Sites NGHP-01-14

By T. Collett, M. Riedel, J. Cochran, R. Boswell, J. Presley, P. Kumar, A. Sathe, A. Sethi, M. Lall, and the National Gas Hydrate Program Expedition 01 Scientists

Scientific Investigations Report 2012–5054

U.S. Department of the Interior
U.S. Geological Survey

Contents

Background and Objectives....675
Operations....675
Hole NGHP-01-14A....675
Lithostratigraphy....679
Lithostratigraphic Units....681
Lithostratigraphic Unit I....681
Gas-Hydrate Occurrence....683
Inorganic Geochemistry....683
Interstitial Water Chloride—Gas-Hydrate Distribution....683
Sulfate and Alkalinity Concentrations: Characterization of the SMI....689
Bromide Concentrations....693
Organic Geochemistry....693
Microbiology....699
Hole NGHP-01-14A....699
Physical Properties....699
Infrared (IR) Imaging....699
Environmental Conditions....699
Infrared Images....705
Core-End Temperature Readings....705
Physical Property Trends....708
Index Properties....708
Strength....708
Electrical Resistivity....711
P-wave Velocity....711
Magnetic Susceptibility (MS)....713
Thermal Conductivity....713
Downhole Temperature Measurements....713
Pressure Coring....713
Pressure Core Operations and Measurements....714
Gas-Hydrate Concentration, Nature, and Distribution from Pressure Coring....714
Downhole Logging....732
Operations....732
Logging Data Quality....739
Logging Units....739
Gas-Hydrate and Free Gas Occurrence....743
References Cited....745

Figures

1. Location of Site NGHP-01-14 in the Krishna-Godavari Basin....676
2. Seismic inline AD-94-39 intersecting with Site NGHP-01-14....677
3. Close-up of seismic line AD-94-39 intersecting with Site NGHP-01-14....678
4. Map showing all holes occupied at Site NGHP-01-14....679
5. Lithostratigraphic summary of Hole NGHP-01-14A....680
6. Regional correlation of Sites NGHP-01-05, NGHP-01-14, and NGHP-01-15 across the Krishna-Godavari Basin....682
7. Silt and sand beds and laminae recovered throughout Lithostratigraphic Unit I....686
8. Terrestrial organic matter recovered at Site NGHP-01-14A....690
9. Authigenic carbonate nodules and bands....691
10. Iron monosulfides infilling burrows....692
11. Interstitial water composition depth profiles of A, chloride determined via ion chromatography; B, salinity; C, Br^-/Cl^- ratio; and D, sulfate and alkalinity at Hole NGHP-01-14A....698
12. Plot of headspace methane gas concentration with depth for Hole NGHP-01-14A....702
13. Plot of headspace carbon dioxide gas concentration with depth for Hole NGHP-01-14A....703
14. Plot of methane to carbon dioxide gas ratio with depth for headspace, free/void gas, and PCS gas for Hole NGHP-01-14A....704
15. Plot of free/void gas and PCS methane to ethane gas ratio with depth for Hole NGHP-01-14A....706
16. Catwalk temperature and humidity during drilling operations at Site NGHP-01-14....709
17. Infrared imaging and the derived downhole temperature profile for Hole NGHP-01-14A....712
18. Core-end probe temperature measurement data for Hole NGHP-01-14A....713
19. Core-end infrared image from Hole NGHP-01-14A, with the corresponding reference temperature scale....714
20. Profiles of core recovery, index, and strength properties for Hole NGHP-01-14A....715
21. Profiles of infrared images, core recovery, electrical resistivity, acoustic *P*-wave velocity, magnetic susceptibility, and thermal conductivity for Hole NGHP-01-14A....716
22. Shear strengths normalized by the effective vertical stress versus sub-bottom depth for Hole NGHP-01-14A....722
23. Peak and remolded vane shear strengths and sensitivity for Hole NGHP-01-14A....722
24. Apparent formation factor versus sub-bottom depth for Hole NGHP-01-14A....732
25. Geothermal gradient and estimated depth to the BSR from *in situ* temperature measurements for Hole NGHP-01-14A....733
26. Temperature and pressure versus elapsed time for each pressure corer deployment as recorded by the corer's internal data logger and Micro data loggers, if used....734
27. Temperature versus pressure for the deployment of Core NGHP-01-14A-15E, showing trajectories relative to gas hydrate stability at 30 ppt and 35 ppt salinity....735

28. X-ray images and gamma density measurements collected at near *in situ* pressure and 7 °C for Core NGHP-01-14A-15E 736
29. Summary of data taken from Core NGHP-01-14A-15E before and after depressurization, including gamma density profiles collected before and after depressurization, X-ray images collected before and after depressurization, and line-scan images collected after depressurization....737
30. Pressure versus volume for Core NGHP-01-14A-15E, also showing placement of gas samples....738
31. Methane-phase diagram for Site NGHP-01-14, with total methane concentration measured from the one successful pressure core at Site NGHP-1-14 740
32. Summary of the wireline logs recorded in Hole NGHP-01-14A 741
33. Sonic waveform amplitude and coherence data and velocity logs measured by the DSI in Hole NGHP-01-14A....742
34. Time-depth plot of the preliminary first break times in the Hole NGHP-01-14A vertical seismic profile....743
35. Water saturations from Archie's equation and wireline porosity and resistivity logs in Hole NGHP-01-14A....744

Tables

1. Smear-slide data for Hole NGHP-01-14A....684
2. Sand/silt laminae and beds and silty clay occurrences at Hole NGHP-01-14A....687
3. Coarse fraction (>63 µm) sieve data for Hole NGHP-01-14A....694
4. Interstitial-water data for Hole NGHP-01-14A....696
5. Headspace gas (HS) composition for Site NGHP-01-14....700
6. Void gas (FG) composition for Site NGHP-01-14....705
7. Pressure Core Sampler gas composition for Site NGHP-01-14....706
8. List of microbiological samples taken for Site NGHP-01-14....707
9. List of infrared image files collected on cores on the catwalk from Hole NGHP-01-14A....710
10. List of infrared image files collected on core ends from Hole NGHP-01-14A 710
11. List of temperature probe data from Hole NGHP-01-14A....711
12. Moisture and density (MAD) physical properties for Hole NGHP-01-14A....717
13. Vane shear strength results for Hole NGHP-01-14A....719
14. Torvane strength results for Hole NGHP-01-14A....719
15. Pocket Penetrometer strength results for Hole NGHP-01-14A....721
16. Wenner array electrical resistivity and apparent formation factor results for Hole NGHP-01-14A....723
17. Contact *P*-wave velocity results determined on split cores sections from Hole NGHP-01-14A....732
18. Thermal conductivity results for Hole NGHP-01-14A 732
19. *In situ* temperature estimates from Hole NGHP-01-14A 733
20. Summary of pressure coring operations at Site NGHP-01-14....733
21. Methane-hydrate volume and concentration in pore space for the successful pressure core at Site NGHP-01-14....739

Site NGHP-01-14

By T. Collett, M. Riedel, J. Cochran, R. Boswell, J. Presley, P. Kumar, A. Sathe, A. Sethi, M. Lall, and the National Gas Hydrate Program Expedition 01 Scientists

Background and Objectives

The Site NGHP-01-14 (Prospectus Site GDGH14-A) is located at 16° 03.5577' N, 082° 05.6218' E in the northern part of the Krishna-Godavari (KG) Basin (fig. 1). This site was selected as an alternate location in the program and was not part of the precoring LWD/MWD program. The water depth was predicted to ~895 m.

The objectives of the work carried out at this site follow the general objectives of NGHP Expedition 01:

- Study the occurrence of gas hydrate and establish the background geochemical, geological, geophysical and microbiological baselines for gas-hydrate proxy studies;
- Define the relationship between the sedimentology and structure of the sediments and the occurrence and concentration of gas hydrate;
- Calibrate remote sensing data such as seismic data by acquiring wire-line log data as well as VSP data for time-depth modeling.

The seismic data available at this site are limited to a single NW-SE trending line (line AD-94-39) shown in figure 2. This line shows the typical sediment sequence of basin and ridge observed throughout the KG Basin. Each ridge appears to be associated with a deep-rooted fault, with the basin sequence developed on the down thrown side of the fault towards the SE. The basins are characterized by seafloor-parallel to subparallel, sedimentary sequences, whereas the ridge flanks are dominated by layers of large NW-dips and somewhat brighter reflection amplitude, especially below the BSR that is well developed along this line. Depth of the BSR is estimated at 109 mbsf at Site NGHP-01-14 using a 0.276 s TWT and a seismic wave velocity of 1,580 m/s.

The detailed seismo-stratigraphy at this site is shown in figure 3. The drill location was chosen to avoid the largest amplitudes below the BSR, which likely indicate the presence of free gas. The BSR is well developed between shot points 265 and 280. Between shot points 255 and 265, the BSR is inferred from the abrupt truncation of the bright reflections when they enter the gas-hydrate stability field.

Operations at this site are limited to a total depth of 180 mbsf (around 70 m below the BSR), which is sufficient to fulfill the site-specific objectives and image below the BSR with the wire-line logging tools (which are ~40 m in length).

Operations

This operations summary covers the Leg 3B transit from Site NGHP-01-07 (KGGH06-A) to Site NGHP-01-14 (GDGH14-A) and drilling/coring operations for Hole NGHP-01-14A (fig. 4). Schedule details and statistics for this site can be found as Appendixes:

- Appendix 1: NGHP Expedition 01 Operations Schedules
- Appendix 2: NGHP Expedition 01 Operations Statistics

Included in the "Methods" chapter and the glossary is a list of standard or commonly used operations terms and acronyms.

Hole NGHP-01-14A

Hole NGHP-01-14A was occupied on Leg 3B of NGHP Expedition 01. This was the only hole drilled at alternate Site NGHP-01-14 (GDGH14-A). The 44.0 NMI transit from Site NGHP-01-07 (KGGH06-A) was completed in 5.0 hr at an average speed of 11.6 knots. The vessel was switched from cruise mode to DP control and a positioning beacon was deployed at the prospectus coordinates at 1115 hr on July 10, 2006. The ice bath was installed in the moon pool and the same BHA as was used on the previous Site NGHP-01-07 was deployed from its racked position in the derrick.

Hole NGHP-01-14A was planned as a continuous APC/XCB cored hole to 180.0 mbsf with several pressure cores targeting the gas-hydrate stability field. Temperature measurements were also to be taken using the APCT–3, APCT, and DVTP systems to define a thermal gradient from seafloor to TD. This hole was designed to be "all inclusive" eliminating the need for a second "tools hole" by combining continuous coring with pressure cores. The hole was to culminate with a complete suite of wire-line logs.

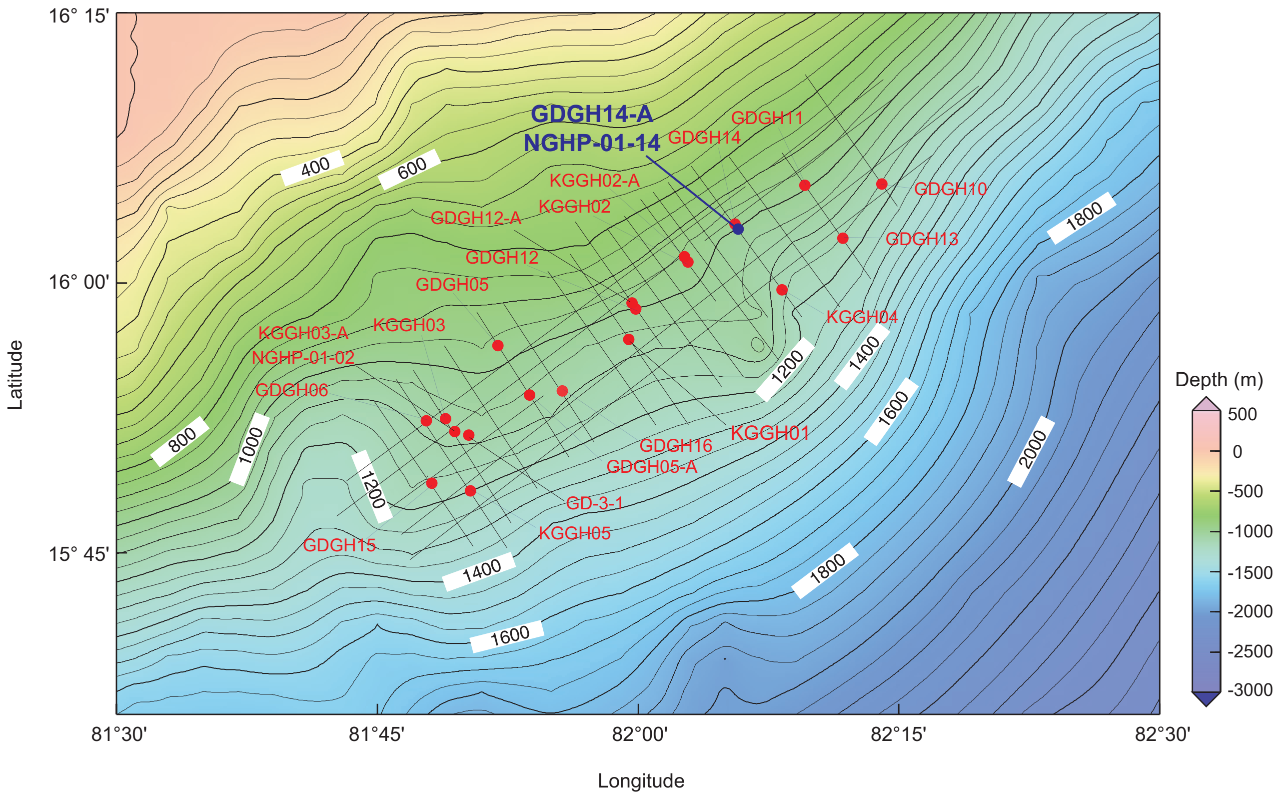

Figure 1. Location of Site NGHP-01-14 (Prospectus Site GDGH14-A) in the Krishna-Godavari (KG) Basin.

The drill string was tripped to bottom. The bit was positioned at a depth of 897.0 mbrf and the first attempt was made to spud Hole NGHP-01-14A. This core barrel recovered only water so the drill string was lowered an additional 5.0 m to 902.0 mbrf. Hole NGHP-01-14A was subsequently spudded at 1435 hr on July 10, establishing a sea floor depth of 906.6 mbrf. The PDR depth for this site, corrected to the rig floor DES, was 908.6 mbrf. APC Core NGHP-01-14A-01H was on-deck at 1445 hr and APC coring continued through Core NGHP-01-14A-08H to a depth of 71.0 mbsf.

Temperature measurements were taken using the APCT–3 shoe on Cores NGHP-01-14A-03H, NGHP-01-14A-05H, and NGHP-01-14A-07H (23.5 mbsf, 42.5 mbsf, and 61.5 mbsf respectively).

After advancing the small diameter APC barrel 9.5 m for Core NGHP-01-14A-08H, the hole was cleaned up with the primary XCB bit and swept with a Sepiolite mud pill. This time a short XCB core was not used to set up the first pressure core because the target depth was very close to the APC stroke depth. The first PCS Core NGHP-01-14A-09P was recovered from 72.0 mbsf. This was followed by the first FPC Core NGHP-01-14A-010Y from 73.0 mbsf. XCB Cores NGHP-01-14A-11X through NGHP-01-14A-13X set up the second PCS Core NGHP-01-14A-14P to 101.0 mbsf and this was followed with the first HRC Core NGHP-01-14A-15E to a depth of 102.0 mbsf. Five XCB Cores NGHP-01-14A-16X through NGHP-01-14A-20X were then cut extending the hole to a depth of 150.0 mbsf. The first DVTP temperature measurement was successfully taken at that depth. Two XCB cores (NGHP-01-14A-21X and -22X) to 169.2 mbsf were recovered and a second DVTP temperature measurement was taken to provide another chance at a deep hole temperature (at TD), which was unsuccessful. One final XCB core (NGHP-01-14A-23X) extended the hole to a total depth of 180.0 mbsf and a final (successful) DVTP temperature measurement was obtained.

Both PCS deployments included successful recovery of data with the PCS Methane tool. Penetration rates with the XCB ranged from 11.5 m/h to 19.2 m/h. Core recovery with the XCB system was again quite variable at 24 percent to 113 percent.

Whirlpaks (microbeads) commonly used for microbiological contamination control were not used for coring; accelerated core barrel handling protocols were used for all core barrels (APC, XCB, and PCS) deployed in this hole. All APC/XCB core barrels were laid down immediately upon arrival at the rig floor before making another drill pipe connection or deploying the next core barrel.

For all HYACINTH pressure coring systems (FPC and HRC) a 15–20 minute wait period was employed at the mudline on the way in the hole and again during retrieval. This was to cool the core barrels down thus aiding in keeping any entrained gas hydrate within the stability field. At the rig floor all pressure core barrels (PCS, FPC, and HRC) showing signs of proper actuation were placed in the moon pool ice bath prior to processing.

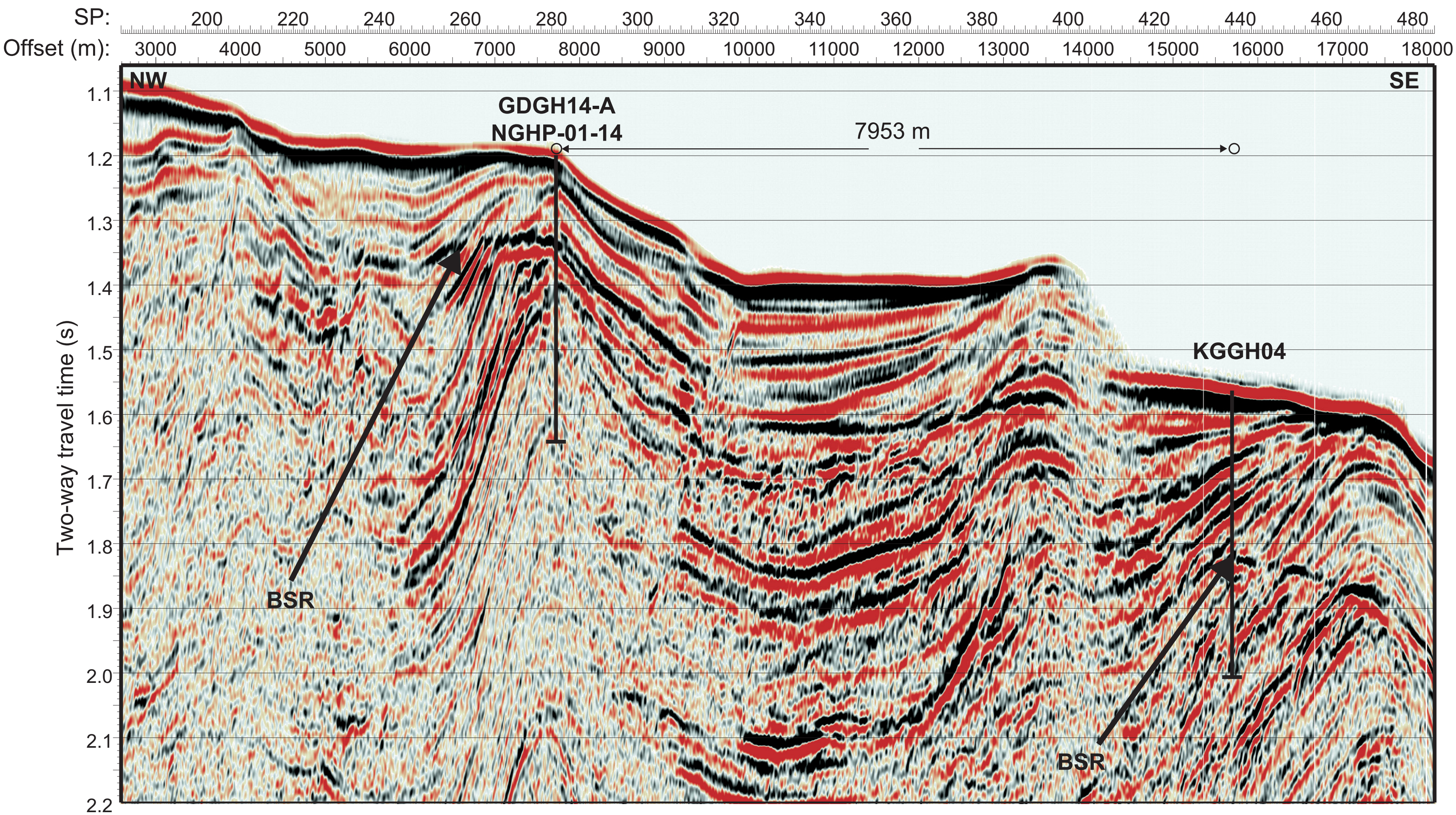

Figure 2. Seismic inline AD-94-39 (oriented NW-SE) intersecting with Site NGHP-01-14 (Prospectus Site GDGH14-A). Also shown is Prospectus Site KGGH04.

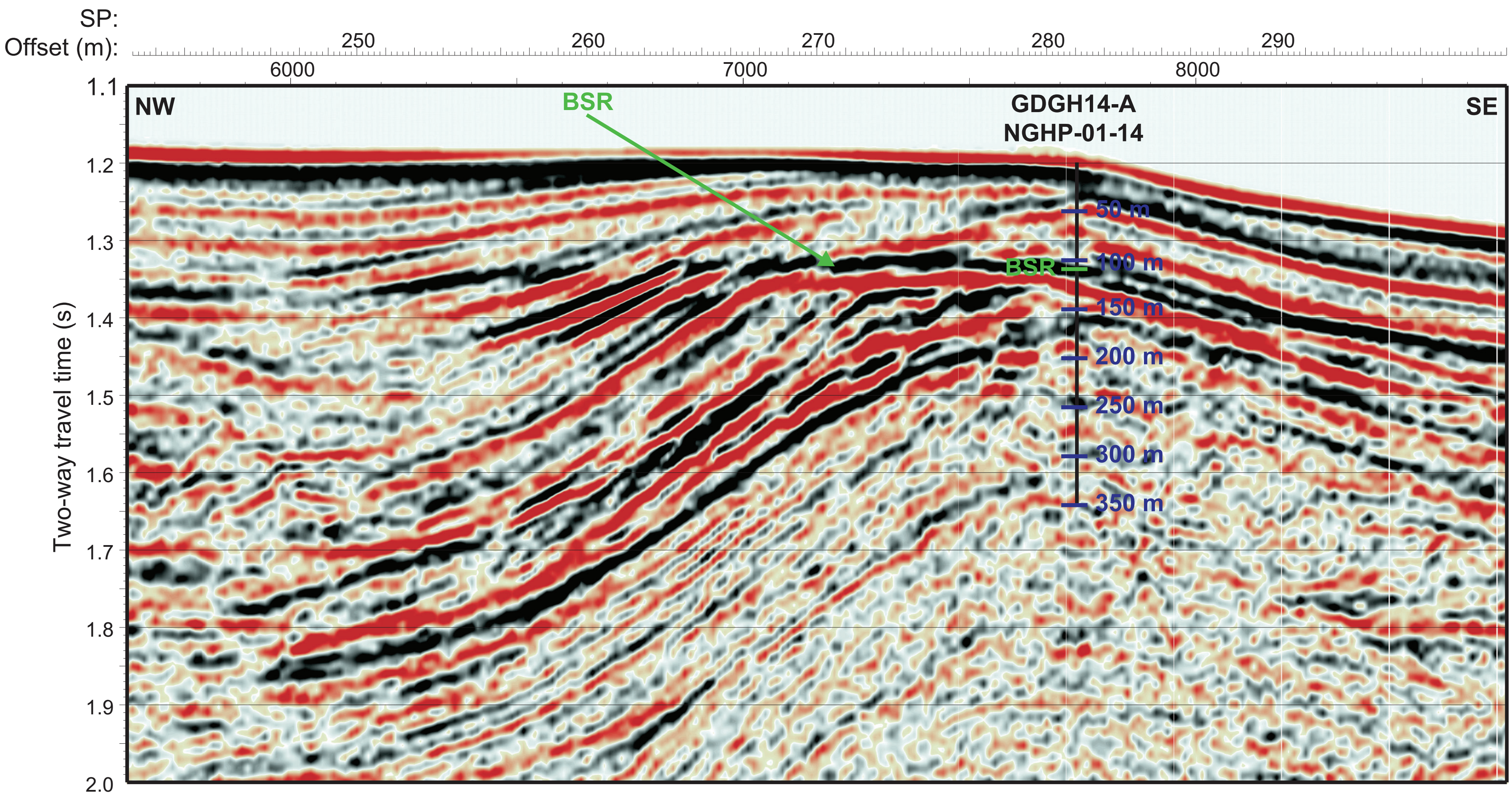

Figure 3. Close-up of seismic line AD-94-39 (oriented NW-SE) intersecting with Site NGHP-01-14 (Prospectus Site GDGH14-A). Formation and BSR depths were estimated using a constant velocity of 1580 m/s for the entire sediment column. [BSR, bottom-simulating reflector; m/s, meters per second]

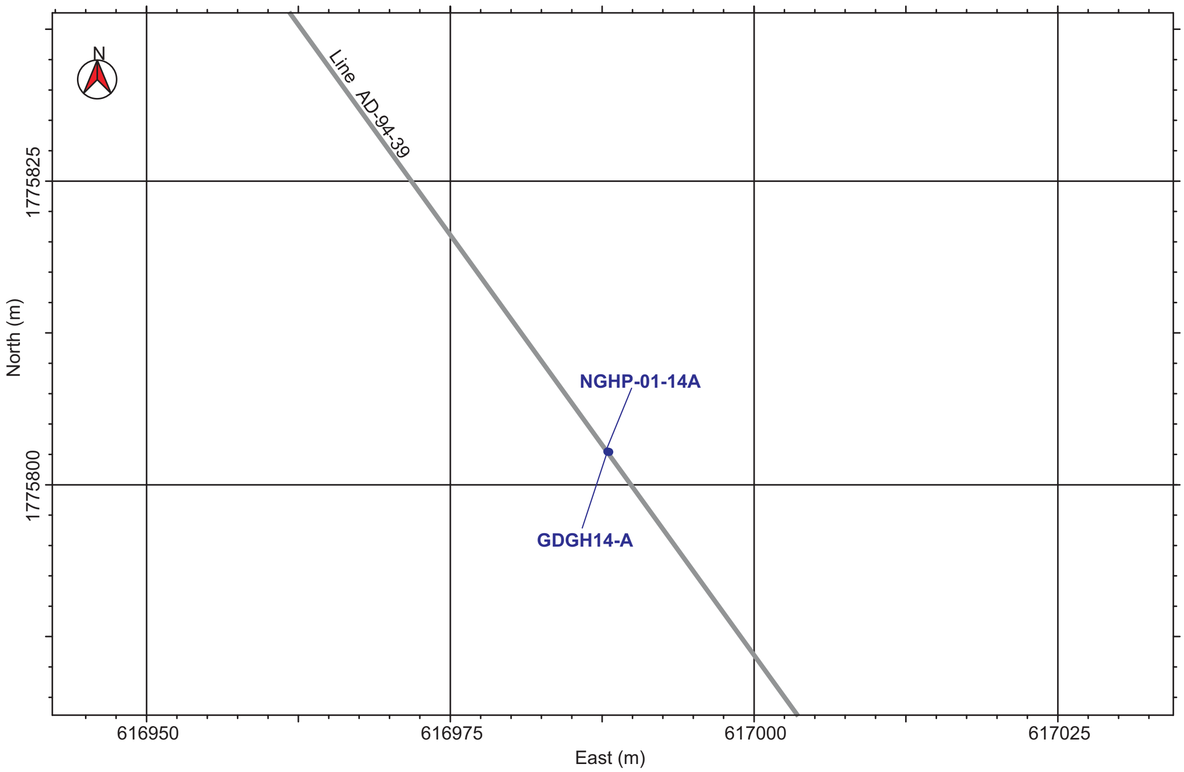

Figure 4. Map showing all holes occupied at Site NGHP-01-14 (GDGH14-A).

The hole was swept with a Sepiolite mud pill and 1.25 hr were spent conducting a wiper trip to logging depth and back. An expendable go-devil was deployed to lock the LFV in the open position and the hole was displaced with 40 barrels of 10.5 ppg weighted mud. The drill string was then tripped setting the EOP at 58.4 mbsf.

At 2230 hr on July 11, 2006, rig-up for logging began. The first logging run was made with the Triple Combo tool suite; however, a bridge in the hole immediately below the bit prevented the tools from going downhole. The logging tools were recovered, laid out, and a single joint of drill pipe was added to the string placing the bit at a depth of 67.4 mbsf. The Triple Combo tool suite was made up once again and this time the tools reached the total hole depth of 180.0 mbsf. The tools were out by 0830 hr on July 12, 2006.

The second tool suite consisted of the FMS-Sonic. This tool string also reached TD and the tools were out by 1230 hr. The VSP logging tools were deployed third in the sequence. VSP operations were completed before dusk and the tools were out of the hole by 1730 hr. As on earlier sites, all VSP operations were conducted while adhering to the IODP policies and mammal protection guidelines. The Schlumberger logging sheaves were rigged down and the drill string was pulled clear of the sea floor at 1845 hr. The positioning beacon was recovered during the pipe trip back to the surface. The vessel was to be moved to the next site (NGHP-01-15) in DP mode and this happened to be down current. Therefore the vessel was allowed to drift towards the next site while retracting the hydrophones. The transit officially began at 2045 hr on July 12, 2006.

Lithostratigraphy

Site NGHP-01-14 is located in the Krishna-Godavari (KG) Basin, along the eastern continental margin of India. At Site NGHP-01-14, one hole (NGHP-01-14A) was drilled, cored, and wire-line logged to a total depth of 180 mbsf (see “Operations”).

We classify the sedimentary sequence recovered at Hole NGHP-01-14A as one Lithostratigraphic Unit (Unit I) based on sedimentological criteria (for example, variations in sedimentary structure and grain size or biogenic and lithologic components) and physical property (for example, magnetic susceptibility) and wire-line logging data (for example, wire-line density; fig. 5 and Site NGHP-01-14 Visual Core Descriptions in the supplemental data files). We also integrate the core data with the available seismic data to help define and interpret the stratigraphic section cored at Site NGHP- 01-14.

The lithostratigraphy recovered at Site NGHP-01-14 is similar to the lithostratigraphy previously drilled at the other sites throughout the Krishna-Godavari Basin. Site NGHP-01-14 is located between Sites NGHP-01-05 and NGHP-01-15, and all three sites are located in a NE-SW line along the 900–950 m water depth contour. Sites NGHP-01-03, NGHP-01-10 and NGHP-01-12, are all located to the SW in slightly deeper water (950–1,050 m). The lithostratigraphy at all three Sites (NGHP-01-05, NGHP-01-14, and NGHP-01-15) is generally similar, (nannofossil-bearing-to-rich clay and clay); however, there are thicker sands at Sites NGHP-01-14 (see below) and Site NGHP-01-15 (see “Lithostratigraphy” in “Site

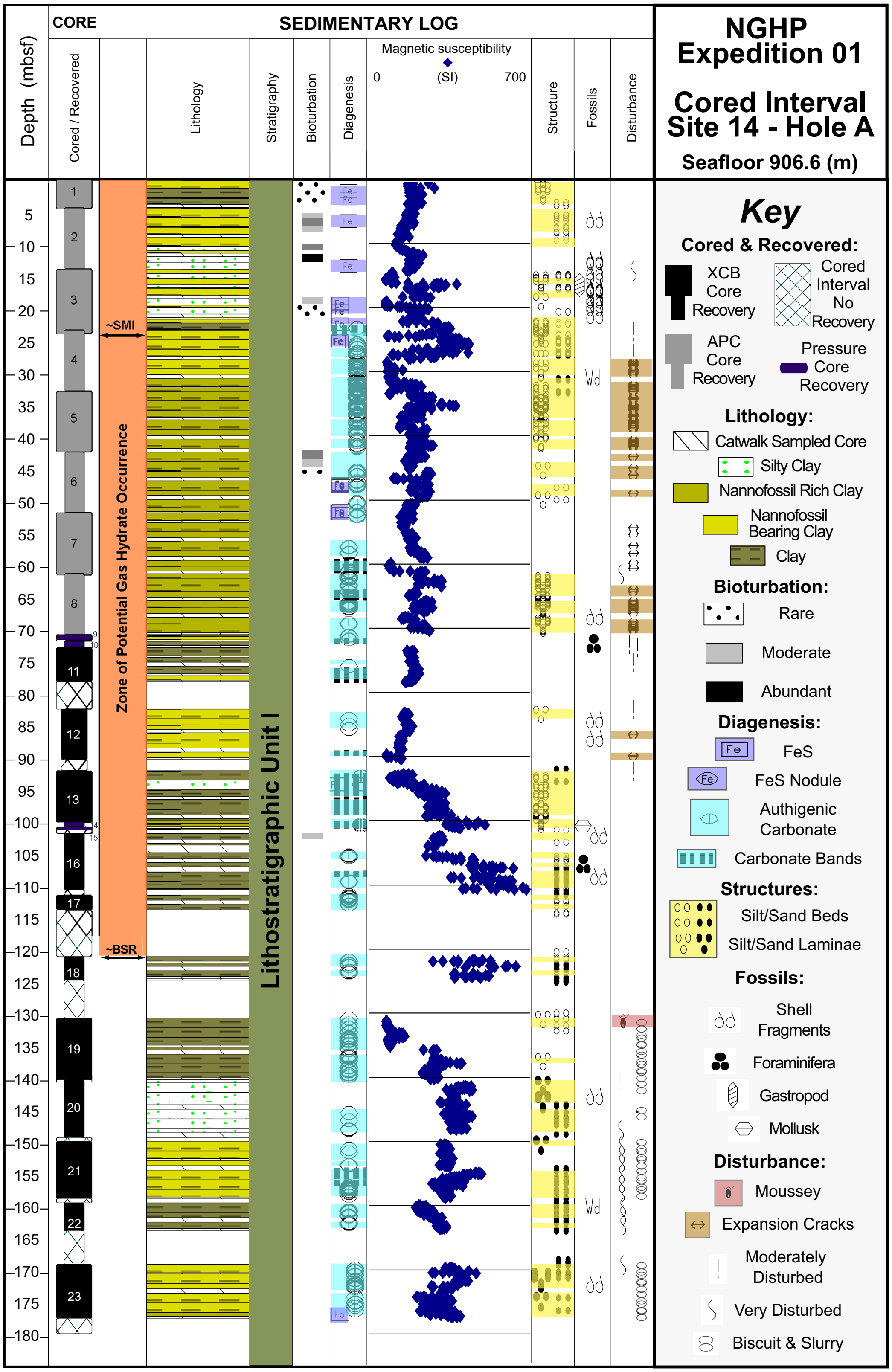

Figure 5. Lithostratigraphic summary of Hole NGHP-01-14A. [BSR, bottom-simulating reflector; RAB, Resistivity-At-Bit; SMI, Sulfate-Methane Interface] Note: Colored intervals exceed symbol size when there is a range in the occurrence. Center point of each symbol represents depth of occurrence; therefore colored bars may slightly exceed core recovery; see Site NGHP-01-14 Visual Core Descriptions for the expanded scale, detailed core descriptions; see Site NGHP-01-14 Oversized Figure for the enlarged version of this summary.

NGHP-01-15) than at Site NGHP-01-05. Although individual sand beds may be thicker at Sites NGHP-01-14 and NGHP-01-15 (relative to Site NGHP-01-05), all three sites are similar in the occurrence of sand and silt lamina and beds (of various thickness) throughout the section, as well as authigenic carbonates, and iron sulfides. LWD density (Site NGHP-01-05 only), wire-line density (Sites NGHP-01-14 and NGHP-01-15), and magnetic susceptibility data show some correlative stratigraphic packages across the three sites (fig. 6). However, variations in the degree and location of diagenesis (authigenic carbonates, iron monosulfide and pyrite precipitation, the degree of lithification, and gas-hydrate and free gas overprinting of the stratigraphy) from site to site make correlations based on physical property and logging data tenuous.

Similar to other KG Basin sites, we observed cyclicity in the RGB color scans of the cores and a lack of *Discoaster* spp. in the record here. Both of these suggest that the age of the stratigraphy is Quaternary. Nevertheless, because of the lithostratigraphic similarity between Site NGHP-01-14 with Sites NGHP-01-05 and NGHP-01-15, we define one Lithostratigraphic Unit (I) at Site NGHP-01-14 (figs. 5, 6, and Site NGHP-01-14 Visual Core Descriptions in the supplemental data files).

Lithostratigraphic Units

Lithostratigraphic Unit I

Intervals: Hole NGHP-01-14A,
Sections NGHP-01-14A -01H-1
to NGHP-01-14A-23X-CC

Depth: Hole NGHP-01-14A, 0–180 mbsf

Age: Quaternary

Core recovery was good at Hole NGHP-01-14A for the upper ~73 mbsf, through APC and pressure coring, and less in the XCB cores in the interval from 73 mbsf to the bottom of the hole (fig. 5). In particular, Cores NGHP-01-14A-11 and NGHP-01-14A-12 within the gas-hydrate stability zone, Cores NGHP-01-14A-17 and NGHP-01-14A-18 near the BSR, and Cores NGHP-01-14A-22 and NGHP-01-14A-23 near the bottom of the hole, had the lowest recovery (fig. 5). Core recovery was less in the cores above and near the BSR likely because of apparent coring difficulties induced by gas hydrate (see "Gas-hydrate occurrence" below).

Lithostratigraphic Unit I is composed of nannofossil-bearing to nannofossil-rich clay and clay that ranges in color from dark olive gray (5Y 3/2) to very dark gray (5Y 3/1) to black (2.5Y 2.5/1). Terrestrial organic matter is common (trace to 5 percent) in smear slides taken throughout Unit I (table 1). Thin (0.2–3 cm) silt/sand laminae and beds are abundant in discrete zones throughout the Unit; however, beds up to 9 to 16 cm thick are also seen (fig. 7 and table 2). These thicker sands are similar to those observed at Site NGHP-01-15 (See "Lithostratigraphy" in "Site NGHP-01-15"). Similar to all the sites drilled in the KG Basin, Lithostratigraphic Unit I at Site NGHP-01-14 is likely Quaternary to recent in age (see "Lithostratigraphy" in "Site NGHP-01-05.

Shell fragments, visible foraminifera tests, gastropod shells, and bivalve shells occur sporadically throughout the Unit (fig. 5 and Site NGHP-01-14 Visual Core Descriptions in the supplemental data files). Rare occurrences of woody debris are also observed (figs. 5 and 8, and Site NGHP-01-14 Visual Core Descriptions). Authigenic carbonate precipitates as nodules, bands, and fine-grained precipitates are common throughout the Unit below the current SMI (Sulfate-Methane Interface; figs. 5 and 9, and Site NGHP-01-14 Visual Core Descriptions). Bioturbated zones are most easily seen when highlighted by iron sulfide precipitates (fig. 10 and Site NGHP-01-14 Visual Core Descriptions) and thus are only evident sporadically in Lithostratigraphic Unit I. The dark grey to black color of the cores likely masks much of the iron sulfides; however, identification of iron sulfides in coarse fraction descriptions (table 3) shows it is distributed throughout most of Lithostratigraphic Unit I. In the upper ~100 mbsf, the iron sulfides often occur as framboidal precipitates in foraminifera. Down-core magnetic susceptibility measurements (figs. 5 and 6, and Site NGHP-01-14 Visual Core Descriptions) throughout the Lithostratigraphic Unit I show variability patterns similar to those at Sites NGHP-01-05 and NGHP-01-15 (fig. 6); however, there is a large increase in susceptibility from 92 mbsf to 125 mbsf. Magnetic iron sulfides (likely gregite and(or) pyrrhotite) have been observed in gas-hydrate-bearing sediments offshore western North America (Musgrave and others, 2006) and may be responsible for some of the magnetic susceptibility highs observed here. At Site NGHP-01-03 and Site NGHP-01-16, we observed magnetic iron sulfide nodules that are either gregite or pyrrhotite, confirming their presence throughout much of the stratigraphy in the Krishna-Godavari Basin. Magnetic susceptibility is also high in stratigraphic packages containing abundant sand and silt beds, which often contain magnetite grains (opaque minerals in smear slide; for example, Trehu and others, 2003). Thus, the variations observed in the magnetic susceptibility are likely recording a mixed signal resulting from primary deposition and secondary magnetic iron sulfide precipitation. The zone of highest susceptibility throughout Hole NGHP-01-14A, however, is from 92 mbsf to 125 mbsf This interval coincides with abundant sand and silt lamina and beds, which are the thickest such beds recovered at this site (fig. 7 and table 3). In addition, there appears to be a lack of iron monosulfides, although pyrite is observed throughout this zone in the coarse fractions (table 3).

The major lithologies of Lithostratigraphic Unit I determined from smear slides are primarily comprised of clay-sized (75–100 percent) grains with minor amounts of silt-sized grains (up to 20 percent) and some sand (table 1). Minor lithologies described in smear slide include silt/sand beds, authigenic carbonates, and iron sulfide rich zones. The major nonbiogenic components of Lithostratigraphic Unit I

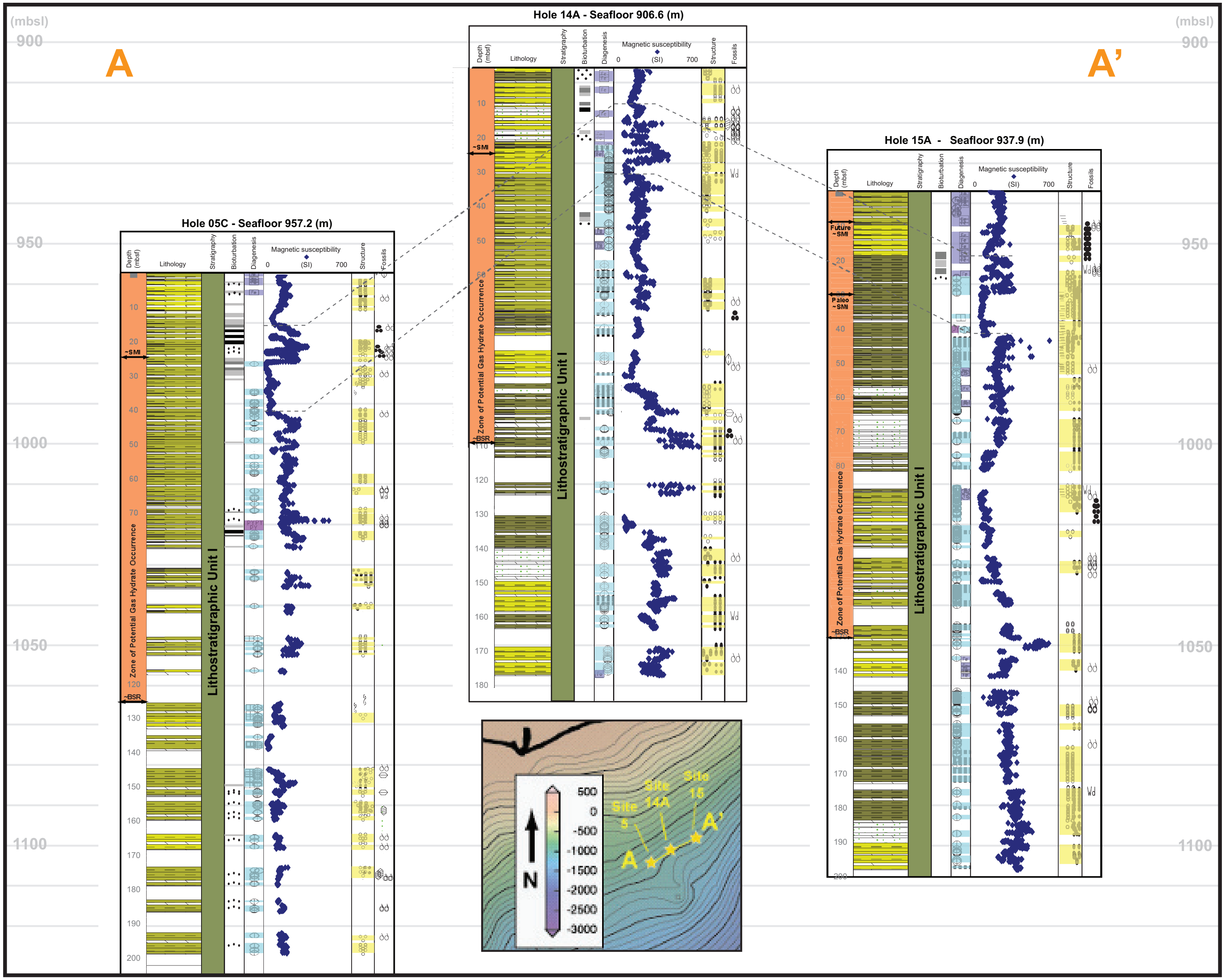

Figure 6. Regional correlation of Sites NGHP-01-05, NGHP-01-14, and NGHP-01-15 across the Krishna-Godavari Basin. Although the lithostratigraphy at all three sites is similar, the physical property correlations suggested here—although intriguing—are tenuous because of varying degrees of diagenetic overprinting of the primary stratigraphy between the cores sites; see Site NGHP-01-14 Oversized Figure for the enlarged version of this correlation. [BSR, bottom-simulating reflector; SMI, sulfate-methane interface]

are quartz, feldspar, mica, clay, and heavy minerals. Opaque grains, mostly sulfides in irregular and framboidal forms or heavy minerals, are common in all grain sizes, and typically comprise trace amounts of the total sediment in the clays, but higher percentages in the silts (table 1). The total biogenic component of the sediment is dominated by calcareous nannofossils, which comprise trace to 25 percent of the total (biogenic and nonbiogenic) sediment grains (table 1). Foraminifera are common in the coarse fractions of the sediments throughout the hole and are especially predominant in coarse fractions taken from the upper 16 mbsf (table 3). These are often visible with the naked eye on the split core surfaces as well and occasionally are observed in smear slide (trace to 5 percent; table 1). Terrestrial organic matter was also observed in smear slide (trace to 5 percent) throughout the sediments of Lithostratigraphic Unit I (table 1). Woody debris was observed in two locations in Hole NGHP-01-14A (fig. 8). Authigenic carbonate precipitates were also observed in smear slides (trace to 70 percent) from ~23 mbsf to TD (table 1).

Gas-Hydrate Occurrence

Gas hydrate was inferred from small increases in resistivity on the wire-line resistivity FMS tool (See "Downhole logging"). Gas hydrate was also observed in some interstitial water (IW) samples prior to squeezing. Evidence of dissociated gas hydrate was also observed as pore water freshening spikes in Cores NGHP-01-14A-05H, -09P, and -11X (see "Inorganic geochemistry"). IR anomalies were also observed throughout these same cores when imaged on the catwalk and also observed in Sections NGHP-01-14A-16X-1-3; whole-round gas-hydrate samples were collected from Sections NGHP-01-14A-16X-1-3 on the catwalk (Site NGHP-01-14 Visual Core Descriptions).

Inorganic Geochemistry

The main objectives of the inorganic geochemistry program at this site were to (1) constrain the fluid and gas source(s), subsurface hydrology (transport mechanisms and migration pathways), and biogeochemical reactions associated with subsurface gas hydrate, and (2) quantify the content and distribution of gas-hydrate based on dissolved chloride concentrations and determine the relationship between the regional hydrogeochemistry and gas-hydrate distribution. The primary objective of the high-resolution sampling in the upper 23 m of the sediment column was to characterize the sulfate-methane interface (SMI) for future geochemical modeling studies and to provide supporting data and samples for studies on the microbial dynamics of the SMI. The IW geochemistry data are tabulated in table 4, and illustrated in figure 11.

A total of 51 whole-round samples were collected for IW analyses at Site NGHP-01-14 in the Krishna-Godavari Basin offshore the eastern margin of the Indian Peninsula. Whole-round lengths ranged from 10 to 30 cm, with longer sections subsampled from cores recovered deeper within the hole. Samples were collected at a frequency of six samples per core in the upper 23 m, two whole-round samples per core to the BSR (~110 mbsf), two whole-round samples per core to 123 mbsf, and one sample per core to TD. The whole-round sampling program was coordinated with both the organic geochemistry and microbiology sampling programs. In addition to the general whole-round sampling scheme, intervals with IR anomalies were sampled on the catwalk. The IR anomaly whole-round samples were immediately transferred to the chemistry laboratory, removed from the core liner, split in half, and imaged with a hand-held IR camera. The anomaly was then separated from the whole-round sample and squeezed. If the anomaly was heterogeneous, then lithologies were separated (that is, silt and clay) and squeezed separately to examine the original percent pore space gas-hydrate occupancy of each sediment type. In addition to routine catwalk whole-round sampling, four pressure cores were sampled (two PCS, one HRC, and one FPC pressure cores). Pressure cores were subsampled for interstitial water squeezing based on X-ray logs.

Interstitial Water Chloride—Gas-Hydrate Distribution

Chloride concentrations were measured by IC at this site due to the paucity of indicator solution used for manual titrations left after the first four sites of Leg 3 of NGHP Expedition 01. The accuracy and precision of the IC technique is not as robust as the $AgNO_3$ titration method with the percent precision of chloride values determined via the IC method averaging 0.7 percent compared to 0.2 percent by titration. The Cl^- concentration data are presented in table 4 and the Cl^- concentration profile is illustrated in figure 11A. The Cl^- data presented here should be viewed as preliminary and are only presented to demonstrate the relative concentrations of gas hydrate in the sediments. The samples were analyzed for Cl^- concentrations shore-based by titration with $AgNO_3$. The interstitial Cl^- concentrations at Site NGHP-01-14 range from 565 to 493 mM. Chloride concentrations are variable from the seafloor to 20 mbsf ± 2 percent of the mean, which is greater than the precision of the analytical technique, indicating that some of the variability reflects *in situ* changes in pore water chlorinity. From 20 mbsf to the base of Hole NGHP-01-14A, chloride concentrations are below the shallow values with local Cl^- depletions as great as 12 percent. Below 20 mbsf, the only slightly depleted chloride concentrations having a rather constant value suggest that the majority of the gas hydrate

Table 1. Smear-slide data for Hole NGHP-01-14A.

Sample reference		Texture			Mineral										
Core, section, depth (cm, in section)	Lithology	Sand	Silt	Clay	Quartz	Feld-spar	Mica	Heavy minerals	Clay minerals	Volcanic glass	Opaques	Iron sulfides	Fram-boidal pyrite	Rock fragments	Authigenic carbonates
NGHP-01-14A															
1H-1,39.5	D			100	3	trace			88			trace			
1H-2,111	D		10	90	2		trace		94			1			
1H-3,23.5	M	5	95		80	5	1					10			
2H-2,70	D		9	95	2			trace	87			3			
2H-6,57	D		2	98	2				93						
3H-2,52	M		100		80	1		1				15			
3H-2,110	D		5	95	trace				95			1			
3H-7,54	D		3	97	1				93			2			
4H-1,113	D		5	95	2	2	1	trace	90			trace			trace
4H-3,83	D		3	97	2	trace	1	trace	80			trace			2
4H-6,97.5	M	35	2	63	20	5	10	trace	33	trace		2			
4H-6,8	M		35	65	5	trace	trace		10			65			trace
5H-6,11	D	1	2	97	2	trace	1	trace	80	trace					2
5H-6,15	D		10	90	3	trace	1	trace	74						7
5H-2,107	M	75	5	20	25	10	20	2	15	trace		13			10
6H-2,140	D		10	90	5	trace	5		66	trace		2			4
6H-2,55	D		7	93	2	trace	trace		73			trace			
6H-7,67	D		20	80	8	1	5	2	60	trace		2			4
7H-7,50	D		1	99	trace	trace			45						30
7H-3,70	D		3	97	2	trace	trace	trace	71			trace			1
8H-2,96	M	98	2	trace	45	20	25	5				5			
8H-4,19	D	2	15	83	9	5	2	trace	53	trace		2			15
8H-3,67	M	15	15	70	10	5	2	3	33	trace		12			30
9P-1,9	D		5	95	2				89						
10Y-1,20	D		1	99	1				94			trace			
11X-1,69	D		2	98	5				86			4			
11X-4,36	D		1	99	1				90			2			
12X-1,124	D			100	1				94			trace			trace
12X-5,54	D		1	99	1				93			1			trace
14P-1,2	D		20	80	10	2		2	71						
15E-1,28	D		1	99	4				84						
13X-1,77	D	1	10	89	5	trace			85			5			1
13X-4,62	D		2	98	2		1		92			trace			1
13X-2,146	M	20	70	10	64			5	9			20			
16X-1,34	D		2	98	2				94						1
16X-5,30	M		75	25	50	1			8			2			39
16X-6,82	D		2	98	5		trace		88			2			
17X-1,42	D		3	97	4				91			1			trace
18X-1,37.5	D		5	95	2		trace		91			3			trace
18X-2,36	M		10	90	30										70
19X-1,99	M		2	98	3				93						
19X-5,44	D		3	97	5	1			90						1
20X-2,57	M	13	25	62	15	5	7	3	55			3			9
20X-3,100	D	2	30	68	14	5	7	1	58	1		4			10
21X-1,104	D		17	83	9	3	5	1	52	trace		1			14
21X-1,71	M	55	5	40	28	8	12	5	37	trace		4			4
21X-5,8	D	2	10	88	6	2	3	1	64	trace		2			10
22X-2,35	D	2	14	84	9	2	3	1	76	trace		1			5
22X-3,40	M	80	9	11	35	10	24	9	11	trace		11			trace
23X-1,19	M	85	5	10	35	17	14	4	10	2		12			6
23X-3,40	D	trace	40	60	20	6	11	2	42	2		2			6
23X-6,50	D	trace	8	92	4	trace	2	trace	46	1		2			25

Table 1. Smear-slide data for Hole NGHP-01-14A.—Continued

Sample reference		Biogenic							
Core, section, depth (cm, in section)	Lithology	Fora-minifera	Nanno-fossils	Carbonate shell fragments	Diatoms	Radio-larians	Sponge spicules	Plant debris	Comments
				NGHP-01-14A—Continued					
1H-1,39.5	D	1	8					trace	
1H-2,111	D	trace	2					1	
1H-3,23.5	M			1				3	From silt bed
2H-2,70	D		7					1	
2H-6,57	D	trace	5					trace	
3H-2,52	M			3					From silt bed
3H-2,110	D	1	1					2	
3H-7,54	D		2					2	
4H-1,113	D		5					trace	
4H-3,83	D		15					trace	
4H-6,97.5	M		30					trace	From sand layer
4H-6,8	M							20	From wood and FeS layer
5H-6,11	D		15						
5H-6,15	D		15					trace	
5H-2,107	M		5						From sand layer
6H-2,140	D	trace	18						
6H-2,55	D		20					5	
6H-7,67	D	trace	17					1	
7H-7,50	D		25						
7H-3,70	D		25					1	
8H-2,96	M								
8H-4,19	D	trace	14					trace	
8H-3,67	M	trace	5					trace	From sand burrow fill
9P-1,9	D	2	5					2	
10Y-1,20	D		3					2	
11X-1,69	D		3					2	Contains pyrite
11X-4,36	D		5					2	
12X-1,124	D	trace	5						
12X-5,54	D	trace	5						
14P-1,2	D		15						
15E-1,28	D	5	5					2	
13X-1,77	D		2					2	
13X-4,62	D		2					2	
13X-2,146	M	2							
16X-1,34	D	trace	trace					3	
16X-5,30	M								Silt with aragonite crystals
16X-6,82	D		trace					5	
17X-1,42	D		2					2	
18X-1,37.5	D	trace	1					3	
18X-2,36	M								From carbonate layer
19X-1,99	M	1	2					1	
19X-5,44	D							3	
20X-2,57	M	3							From sand layer
20X-3,100	D	trace						trace	
21X-1,104	D		15					trace	
21X-1,71	M	trace	2					trace	From silt bed
21X-5,8	D		12						
22X-2,35	D	trace	3					trace	Apatite present
22X-3,40	M	trace	trace						From sand layer
23X-1,19	M							trace	From sand layer
23X-3,40	D	trace	9					trace	
23X-6,50	D		20					trace	

Note: M = minor lithology, D = dominant lithology

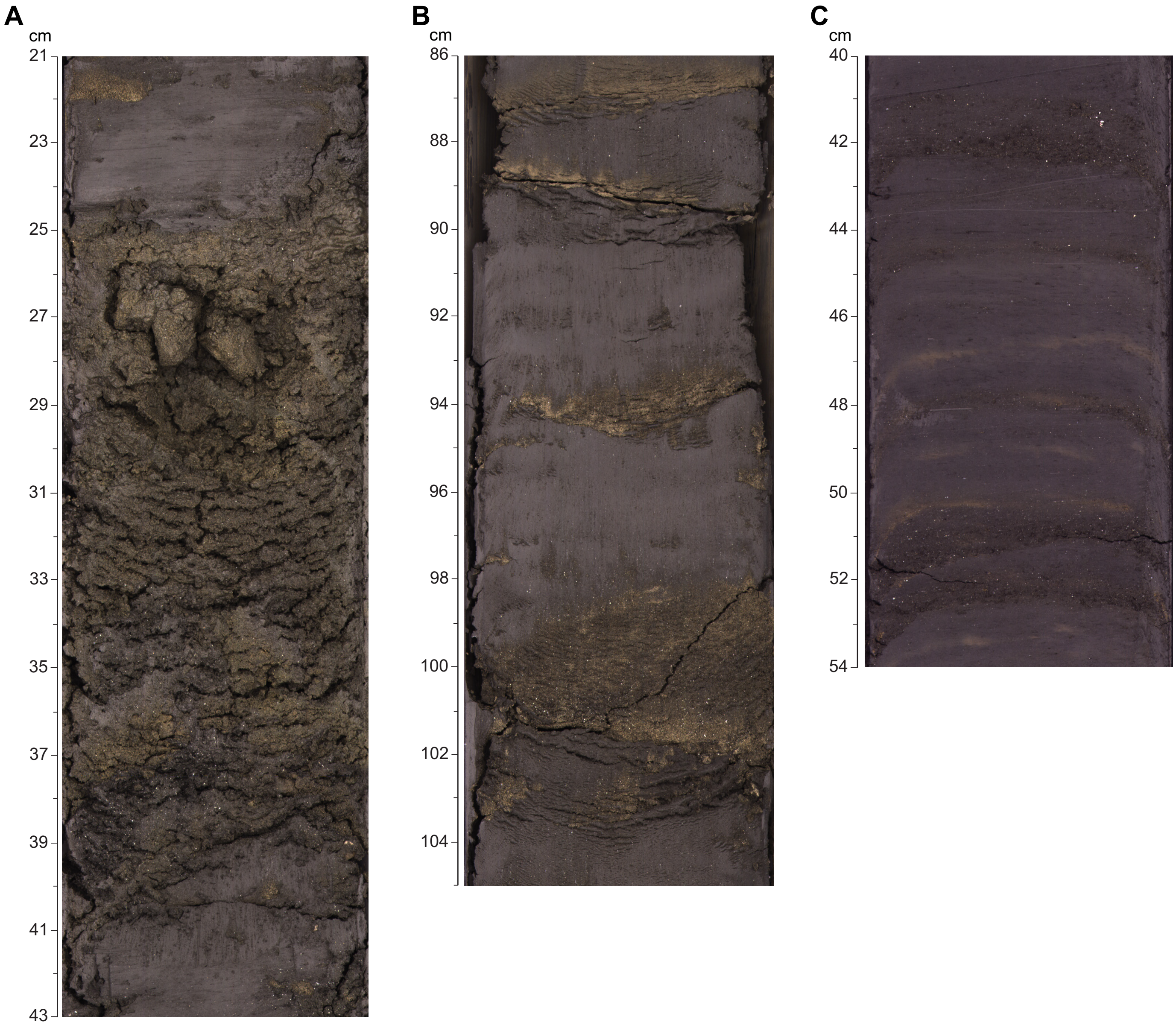

Figure 7. Silt and sand beds and laminae recovered throughout Lithostratigraphic Unit I. The thickest beds within Hole NGHP-01-14A were observed in *A*, Section NGHP-01-14A-16X-5, 21–43 cm and *B*, Section NGHP-01-14A-16X-6, 86–105 cm. *C*, Shows thin silt laminae typical of Lithostratigraphic Unit I from Section NGHP-01-14A-05H-3, 40–54.5 cm; also notice the thin authigenic carbonate bands among the silt laminae.

Table 2. Sand/silt laminae and beds and silty clay occurrences at Hole NGHP-01-14A.

Core, section	Position start	Position end	Depth top (mbsf)	Depth base (mbsf)	Type
NGHP-01-14A					
1H-1	20	20	0.2	0.2	silt bed
1H-1	88	90	0.88	0.9	silt bed
1H-2	42	43	1.92	1.93	silt bed
1H-2	97	98	2.47	2.48	silt bed
1H-2	127	128	2.77	2.78	silt bed
1H-3	22	23	3.22	3.23	silt bed
1H-3	50	50	3.5	3.5	silt bed
1H-3	77	77	3.77	3.77	silt bed
1H-3	82	83	3.82	3.83	silt bed
2H-1	12	12	4.62	4.62	silt bed
2H-1	45	46	4.62	4.62	silt bed
2H-2	56	58	6.56	6.58	silt bed
2H-2	126	127	7.26	7.27	silt bed
2H-3	101	101	7.01	7.01	silt bed
2H-3	53	54	6.53	6.54	silt bed
2H-4	137	139	10.37	10.39	very silty clay
2H-5	0	59	10.5	11.09	silty clay
2H-6	0	90	12	12.9	silty clay
2H-7	0	101	13	14.01	silty clay
3H-1	70	140	14.7	15.4	silty clay
3H-2	29	29	15.79	15.79	silt bed
3H-2	32	33	15.82	15.83	silt bed
3H-2	35	35	15.85	15.85	silt bed
3H-2	37	37	15.87	15.87	silt bed
3H-2	51	53	16.01	16.03	silt bed
3H-2	70	71	16.2	16.21	silt bed
3H-2	42	42	15.92	15.92	silt laminae
3H-2	77	77	16.27	16.27	silt laminae
3H-2	83	83	16.33	16.33	silt laminae
3H-2	86	86	16.36	16.36	silt laminae
3H-2	92	140	16.42	16.9	silty clay
3H-3	101	103	18.01	18.03	silt laminae
3H-3	0	94	17	17.94	silty clay
3H-4	83	83	19.33	19.33	silt laminae
3H-4	0	109	18.5	19.59	silty clay
3H-5	6	38	20.06	20.38	silt laminae
3H-5	48	100	20.48	21	silty clay
3H-6	12	13	21.62	21.63	silt bed
3H-6	14	33	21.64	21.83	silty clay
3H-7	71	72	23.21	23.22	silt laminae
3H-7	85	85	23.35	23.35	silt laminae
3H-7	57	57	23.07	23.07	silt laminae
3H-7	76	77	23.26	23.27	silt bed
4H-1	40	42	24.26	24.27	silt bed
4H-1	67	67	23.9	23.92	silt bed
4H-1	75	75	24.17	24.17	silt bed
4H-1	79	79	24.25	24.25	silt bed
4H-1	96	96	24.29	24.29	silt bed
4H-1	102	102	24.46	24.46	silt bed
4H-1	103	103	24.52	24.52	silt bed
4H-1	108	108	24.53	24.53	silt bed
4H-1	134	134	24.58	24.58	Silt bed
4H-1	148	148	24.84	24.84	Silt bed
4H-2	21	21	25.21	25.21	Silt bed
4H-2	81	81	25.81	25.81	Silt bed
4H-2	104	104	26.04	26.04	Silt bed
4H-2	107	107	26.07	26.07	Silt bed
4H-2	111	111	26.11	26.11	Silt bed
4H-2	115	115	26.15	26.15	Silt bed
4H-2	119	119	26.19	26.19	Silt bed
4H-2	132	133	26.32	26.33	Silt bed
4H-2	135	135	26.35	26.35	Silt bed
4H-2	141	142	26.41	26.42	Silt bed
4H-2	145	145	26.45	26.45	Silt bed
4H-2	149	149	26.49	26.49	Silt bed
4H-3	12	14	26.62	26.64	Silty clay
4H-4	4	21	28.04	28.21	Silty clay
4H-5	10	15	29.6	29.65	Silt laminae
4H-5	82	82	30.32	30.32	Silt laminae
4H-5	86	86	30.36	30.36	Silt laminae
4H-5	92	92	30.42	30.42	Silt laminae
4H-6	97	101	31.97	32.01	Silt bed
4H-6	105	109	32.05	32.09	Silt bed
4H-6	111	113	32.11	32.13	Silt bed
4H-6	118	118	32.18	32.18	Silt bed
4H-6	121	121	32.21	32.21	Silt bed
4H-6	122	122	32.22	32.22	Silt bed
4H-6	125	125	32.25	32.25	Silt bed
4H-7	55	55	33.05	33.05	Silty clay
4H-7	62	62	33.12	33.12	Silty clay
5H-1	47	47	33.47	33.47	Silt laminae
5H-1	49	49	33.49	33.49	Silt laminae
5H-1	51	52	33.51	33.52	Silt laminae
5H-1	53	53	33.53	33.53	Silt laminae
5H-1	56	56	33.56	33.56	Silt laminae
5H-1	60	60	33.6	33.6	Silt laminae
5H-1	120	121	34.2	34.21	Silt laminae
5H-2	4	30	34.54	34.8	Multiple silt laminae
5H-2	143	143	35.93	35.93	Silt laminae
5H-2	33	46	34.83	34.96	Silty clay layers
5H-2	86	90	35.36	35.4	Silty clay layers
5H-2	94	96	35.44	35.46	Silty clay layers
5H-2	103	104	35.53	35.54	Silty clay layers
5H-2	105	108	35.55	35.58	Silty clay layers
5H-2	111	111	35.61	35.61	Silty clay layers
5H-2	119	129	35.69	35.79	Silty clay layers
5H-2	131	131	35.81	35.81	Silty clay layers
5H-3	10	10	36.1	36.1	Silty clay layers
5H-3	15	15	36.15	36.15	Silty clay layers
5H-3	18	19	36.18	36.19	Silty clay layers
5H-3	22.5	22.5	36.225	36.225	Silty clay layers
5H-3	26	28	36.26	36.28	Silty clay layers
5H-3	31	31	36.31	36.31	silty clay layers
5H-3	32	32	36.32	36.32	silty clay layers
5H-3	34	34	36.34	36.34	silty clay layers
5H-3	36	36	36.36	36.36	silty clay layers
5H-3	41	42	36.41	36.42	silty clay layers
5H-3	51	51	36.51	36.51	silty clay layers
5H-4	40	41	37.9	37.91	silt bed
5H-4	96	116	38.46	38.66	silty clay layers
5H-4	147	148	38.97	38.98	silty clay layers
5H-5	0	13	39	39.13	multiple silt laminae
5H-5	18	20	39.18	39.2	multiple silt laminae
5H-5	57	93	39.57	39.93	multiple silt laminae
5H-5	0	100	39	40	silty clay
5H-6	62	62	41.12	41.12	silt laminae

Table 2. Sand/silt laminae and beds and silty clay occurrences at Hole NGHP-01-14A.—Continued

Core, section	Position start	Position end	Depth top (mbsf)	Depth base (mbsf)	Type	Core, section	Position start	Position end	Depth top (mbsf)	Depth base (mbsf)	Type
NGHP-01-14A—Continued											
5H-6	65	65	41.15	41.15	silt laminae	13X-5	62	63	98.82	98.83	Silt laminae
5H-6	91	96	41.41	41.46	silt laminae	13X-5	71	74	98.91	98.94	Silt laminae
6H-1	0	82	42.5	43.32	silty clay	13X-5	77	77	98.97	98.97	Silt laminae
6H-3	10	15	45.5	45.5	silty clay	13X-5	79	81	98.99	99.01	Silt laminae
6H-5	53	53	49.03	49.03	silt/sand bed	13X-5	87	89	99.07	99.09	Silt laminae
6H-6	32	32	50.2	50.2	silt laminae	13X-6	7	7	99.77	99.77	Silt laminae
6H-6	33	33	50.21	50.21	silt laminae	13X-6	18	18	99.88	99.88	Silt laminae
7H-7	13	13	51.33	51.33	sand filled burrow(?)	13X-6	25	25	99.95	99.95	Silt laminae
7H-7	20	20	51.4	51.4	sand filled burrow(?)	13X-6	38	38	100.08	100.08	Silt laminae
8H-2	10	10	62.3	62.3	silt/sand laminae	13X-6	51	51	100.21	100.21	silt laminae
8H-2	39	39	62.59	62.59	silt/sand laminae	13X-6	59	63	100.29	100.33	Multiple silt laminae
8H-2	43	43	62.63	62.63	silt/sand laminae	13X-6	89	89	100.59	100.59	Silt laminae
8H-2	96	96	63.16	63.16	silt/sand laminae	13X-6	110	110	100.8	100.8	Silt laminae
8H-2	100	100	63.2	63.2	silt/sand laminae	16X-1	39	39	102.39	102.39	Silt bed
8H-2	105	105	63.25	63.25	silt/sand laminae	16X-3	19	20	105.19	105.2	Silt bed
8H-2	123	123	63.43	63.43	silt/sand laminae	16X-3	30	32	105.3	105.32	silt bed
8H-2	125	125	63.45	63.45	silt/sand laminae	16X-3	38	38	105.38	105.38	silt bed
8H-2	146	146	63.66	63.66	silt/sand laminae	16X-3	50	59	105.5	105.59	multiple silt beds
8H-3	12	12	63.82	63.82	silt/sand laminae	16X-3	72	75	105.72	105.75	multiple silt beds
8H-3	14	14	63.84	63.84	silt/sand laminae	16X-3	89	90	105.89	105.9	silt bed
8H-3	46	46	64.16	64.16	silt/sand laminae	16X-4	2	2	106.52	106.52	silt bed
8H-3	50	50	64.2	64.2	silt/sand laminae	16X-4	10	19	106.6	106.69	multiple silt beds
8H-4	22	22	65.39	65.39	silt/sand laminae	16X-4	33	49	106.83	106.99	multiple silt beds
8H-4	24	24	65.41	65.41	silt/sand laminae	16X-4	56	62	107.06	107.12	multiple silt beds
8H-4	33	44	65.5	65.61	multiple silt laminae	16X-4	72	72	107.22	107.22	silt bed
8H-4	54	68	65.71	65.85	multiple silt laminae	16X-5	15	22	108.15	108.22	silt bed
8H-4	80	81	65.97	65.98	silt/sand laminae	16X-5	56	57	108.56	108.57	silt bed
8H-5	0	3	66.27	66.3	silt/sand laminae	16X-5	25	39	108.25	108.39	sand bed
8H-5	13	15	66.4	66.42	silt/sand laminae	16X-5	68	71	108.68	108.71	sand filled burrow
8H-5	24	26	66.51	66.53	silt/sand laminae	16X-5	74	75	108.74	108.75	sand filled burrow
8H-5	30	32	66.57	66.59	Silt/sand laminae	16X-5	88	122	108.88	109.22	sand filled burrow
8H-5	45	46	66.72	66.73	Silt/sand laminae	16X-5	98	106	108.98	109.06	sand filled burrow
8H-5	49	51	66.76	66.78	Silt/sand laminae	16X-5	112	113	109.12	109.13	sand filled burrow
8H-5	76	76	67.03	67.03	Silt/sand laminae	16X-6	0	16	109.42	109.58	silt bed
8H-5	80	80	67.07	67.07	Silt/sand laminae	16X-6	24	30	109.66	109.72	silt bed
8H-5	87	90	67.14	67.17	Silt/sand laminae	16X-6	36	50	109.78	109.92	silt bed
8H-6	43	102	68.2	68.79	Silty clay	16X-6	64	68	110.06	110.1	sand bed
8H-7	8	11	68.87	68.9	Silt laminae	16X-6	87	87	110.29	110.29	sand bed
8H-7	13	20	68.92	68.99	Multiple silt laminae	16X-6	90	90	110.32	110.32	sand bed
8H-7	42	42	69.21	69.21	Silt laminae	16X-6	94	94	110.36	110.36	sand bed
8H-7	49	56	69.28	69.35	Multiple silt laminae	16X-6	98	102	110.4	110.44	sand bed
8H-7	65	66	69.44	69.45	Silt laminae	16X-6	110	113	110.52	110.55	sand bed
8H-7	69	69	69.48	69.48	Silt laminae	17X-1	10	18	111.7	111.78	multiple silt beds
8H-7	74	74	69.53	69.53	Silt laminae	17X-1	46	67	112.06	112.27	multiple silt beds
8H-7	89	94	69.68	69.73	Multiple silt laminae	17X-1	75	79	112.35	112.39	multiple silt beds
13X-2	19	19	93.89	93.89	Silt laminae	17X-2	12	40	113.11	113.39	silty clay
13X-2	140	140	95.1	95.1	Silt laminae	17X-2	60	60	113.59	113.59	silt bed
13X-2	146	147	95.16	95.17	Silt laminae	17X-2	73	79	113.72	113.78	silt bed
13X-3	6	6	95.26	95.26	Silt laminae	18X-1	16	20	121.36	121.4	sand bed
13X-3	26	26	95.46	95.46	Silt laminae	18X-1	20	29	121.4	121.49	silty clay
13X-3	34	34	95.54	95.54	Silt laminae	18X-1	29	33	121.49	121.53	sand bed
13X-3	57	57	95.77	95.77	Silt laminae	18X-2	8	10	122.28	122.3	silt bed
13X-4	5	5	96.75	96.75	Silt laminae	18X-3	0	2	123.36	123.38	sand bed
13X-4	10	10	96.8	96.8	Silt laminae	18X-3	42	52	123.78	123.88	sand bed
13X-4	32	34	97.02	97.04	Silt laminae	18X-3	55	59	123.91	123.95	sand bed
13X-4	74	75	97.44	97.45	Silt laminae	18X-3	72	75	124.08	124.11	sand bed
13X-4	79	81	97.49	97.51	Silt laminae	18X-3	82	91	124.18	124.27	sand bed
13X-4	138	138	98.08	98.08	Silt laminae	18X-3	11	13	123.47	123.49	silt bed
13X-4	145	147	98.15	98.17	Silt laminae	18X-3	24	28	123.6	123.64	silt bed

Table 2. Sand/silt laminae and beds and silty clay occurrences at Hole NGHP-01-14A.—Continued

Core, section	Position start	Position end	Depth top (mbsf)	Depth base (mbsf)	Type	Core, section	Position start	Position end	Depth top (mbsf)	Depth base (mbsf)	Type
NGHP-01-14A—Continued											
18X-3	35	38	123.71	123.74	Silt bed	21X-5	91	112	156.91	157.12	Multiple sand beds
19X-1	10	21	130.9	131.01	Multiple silt beds	22X-1	22	30	159.82	159.9	Multiple sand beds
19X-1	69	74	131.49	131.54	Multiple silt beds	22X-1	42	42	160.02	160.02	Sand bed
19X-1	32	60	131.12	131.4	Silty clay	22X-1	88	91	160.48	160.51	Multiple sand beds
19X-2	9	9	132.39	132.39	Silt bed	22X-1	101	102	160.61	160.62	Sand bed
19X-5	134	134	137.81	137.81	Sand pocket	22X-1	106	108	160.66	160.68	Sand bed
20X-2	0	90	140.89	141.79	Multiple silt/sand laminae	22X-1	114	115	160.74	160.75	Sand bed
20X-3	117	150	143.56	143.89	Multiple silt pockets	22X-1	118	121	160.78	160.81	Sand bed
20X-4	0	11	143.89	144	Multiple sand pockets	22X-2	18	18	161.28	161.28	Sand laminae
20X-4	11	30	144	144.19	Multiple sand pockets	22X-2	50	52	161.6	161.62	Sand laminae
20X-5	22	32	145.23	145.33	Multiple sand laminae	22X-2	56	80	161.66	161.9	Multiple sand laminae
20X-5	42	42	145.43	145.43	Sand laminae	23X-1	56	56	169.76	169.76	Sand laminae
20X-5	50	50	145.51	145.51	Sand laminae	23X-1	60	60	169.8	169.8	Sand laminae
20X-5	147	147	146.48	146.48	Sand laminae	23X-1	64	64	169.84	169.84	Sand laminae
20X-6	112	120	147.63	147.71	Sand burrow fills	23X-1	80	94	170	170.14	Multiple sand laminae
21X-1	59	72	150.59	150.72	Multiple sand filled burrows	23X-1	108	117	170.28	170.37	Multiple sand laminae
21X-4	10	30	154.6	154.8	Sand bed	23X-2	74	78	171.44	171.48	Multiple sand laminae
21X-4	73	73	155.23	155.23	Sand bed	23X-2	140	150	172.1	172.2	Sand burrow fills
21X-4	67	71	155.17	155.21	Sand bed	23X-2	0	100	170.7	171.7	Sandy clay
21X-4	94	97	155.44	155.47	Sand bed	23X-3	20	23	172.4	172.43	Sand burrow fills
21X-4	100	103	155.5	155.53	Sand bed	23X-4	130	130	175	175	Sand burrow fills
21X-5	30	72	156.3	156.72	Multiple sand beds	23X-5	15	15	175.35	175.35	Sand bed

at Site NGHP-01-14 is most likely disseminated within the sediments at low concentrations. Overprinted on this "diffuse" distribution of gas hydrate are two zones where Cl^- concentrations are depleted by as much as 12 percent relative to modern seawater value, indicating elevated concentrations of gas hydrate that in most cases is not lithologically-controlled. The first of these zones occurs between 31 and 40 mbsf where Cl^- values sharply drop to 515 mM from a background concentration of ~550 mM. The second zone is from 65 to 100.4 mbsf, which is just above the BSR with a depth of 109 mbsf. The Cl^- minimum within this interval is defined by four samples. At 71.2 mbsf, the pressure core sample NGHP-01-14A-09P-1 exhibits a chloride concentration of 517 mM (8 percent depletion) followed by sample NGHP-01-14A-11X-2 with a Cl^- concentration of 513 mM. A moderate IR anomaly was sampled on the catwalk corresponding to NGHP-01-14A-12X-3 (95–105 cm) producing a Cl^- concentration of 509 mM (9 percent depletion). This sample was extremely disturbed and "soupy," a texture that is typically associated with gas-hydrate dissociation induced during the core recovery process, and was contaminated by drilling fluid. The SO_4^{2-} concentration measured in this sample was 4.36 mM, which was used to compute the amount of seawater that infiltrated the sample during drilling, because SO_4^{2-} is depleted within this interval. Using a simple two-end member mixing model between seawater and SO_4^{2-}-depleted formation fluid, the percent dilution of the sample was computed. The percent contamination/dilution is then multiplied by the Cl^- value in sample NGHP-01-14A-12X-3 (95–105 cm) to estimate the in situ chloride concentration of 419 mM, which is a 25 percent depletion and defines the apex of the chloride minimum. The next sample, NGHP-01-14A-12X-3 (105–115 cm), was collected on the catwalk adjacent to the IR anomaly at 86.15 mbsf with a Cl^- concentration of 493 mM. At 100.4 mbsf, Cl^- concentrations rapidly return to background values averaging 540 mM, except for sample NGHP-01-14A-18X-2 (86–116 cm) with 528 mM at 123 mbsf.

Sulfate and Alkalinity Concentrations: Characterization of the SMI

The primary objectives of the high-resolution sampling in the upper 30 m of sediments at this site were to characterize the SMI for future geochemical modeling of methane fluxes and to provide supporting data and samples for studies on the microbial dynamics of the SMI. At Site NGHP-01-14, the SMI is located at 23.4 mbsf. Above the SMI, the sulfate and alkalinity concentration depth profiles can be split into three sections (fig. 11A). The first section is typified by a sharp decrease in sulfate concentrations from the seafloor to 6 mbsf with a corresponding increase in alkalinity concentrations reflecting sulfate reduction and alkalinity production by organic matter oxidation. The second section extends from 6 to 15.4 mbsf and is characterized by a shallower gradient with a coincident decrease in alkalinity reflecting either authigenic

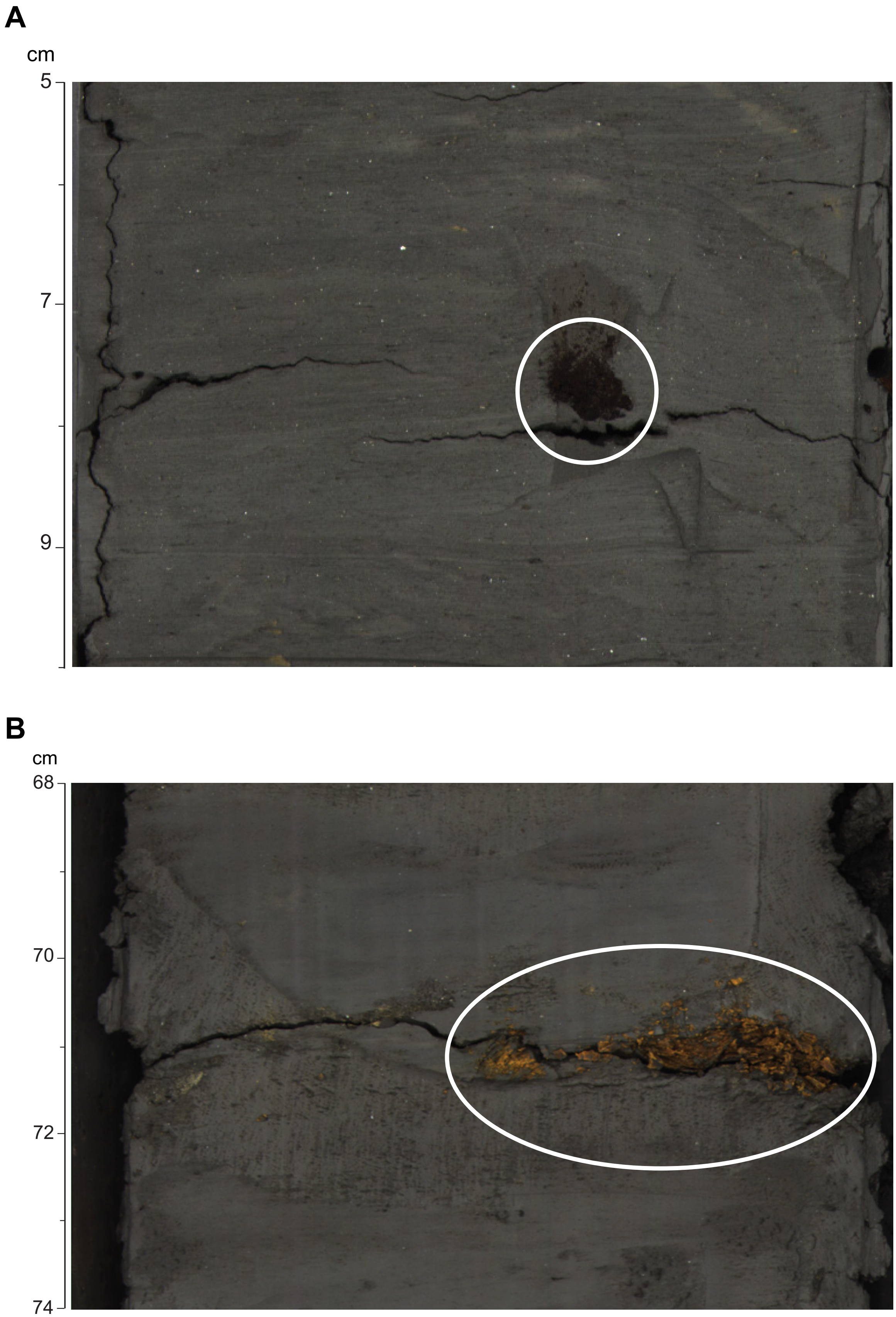

Figure 8. Terrestrial organic matter (circled) recovered at Site NGHP-01-14A. A, Section NGHP-01-14A-04H-6, 5–10 cm. B, Section NGHP-01-14A-22X-1, 68.5–74 cm.

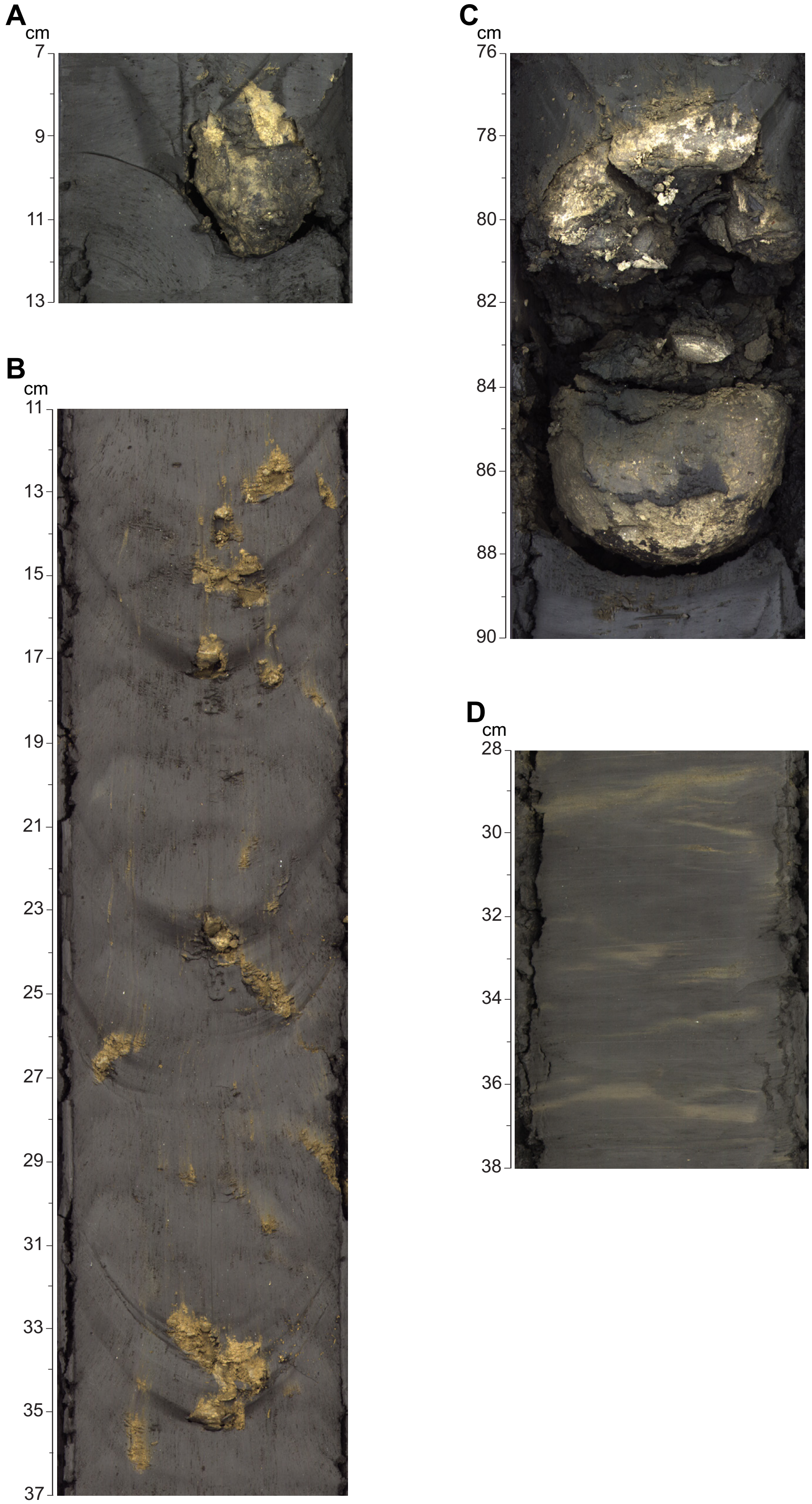

Figure 9. Authigenic carbonate nodules and bands. A, Section NGHP-01-14A-11X-3, 7–13 cm; nodule. B, Section NGHP-01-14A-21X-6, 11.5–37 cm; nodule. C, Section NGHP-01-14A-19X-1, 76–90 cm; large broken nodule. D, Section NGHP-01-14A-13X-5, 28–38 cm; authigenic carbonate bands.

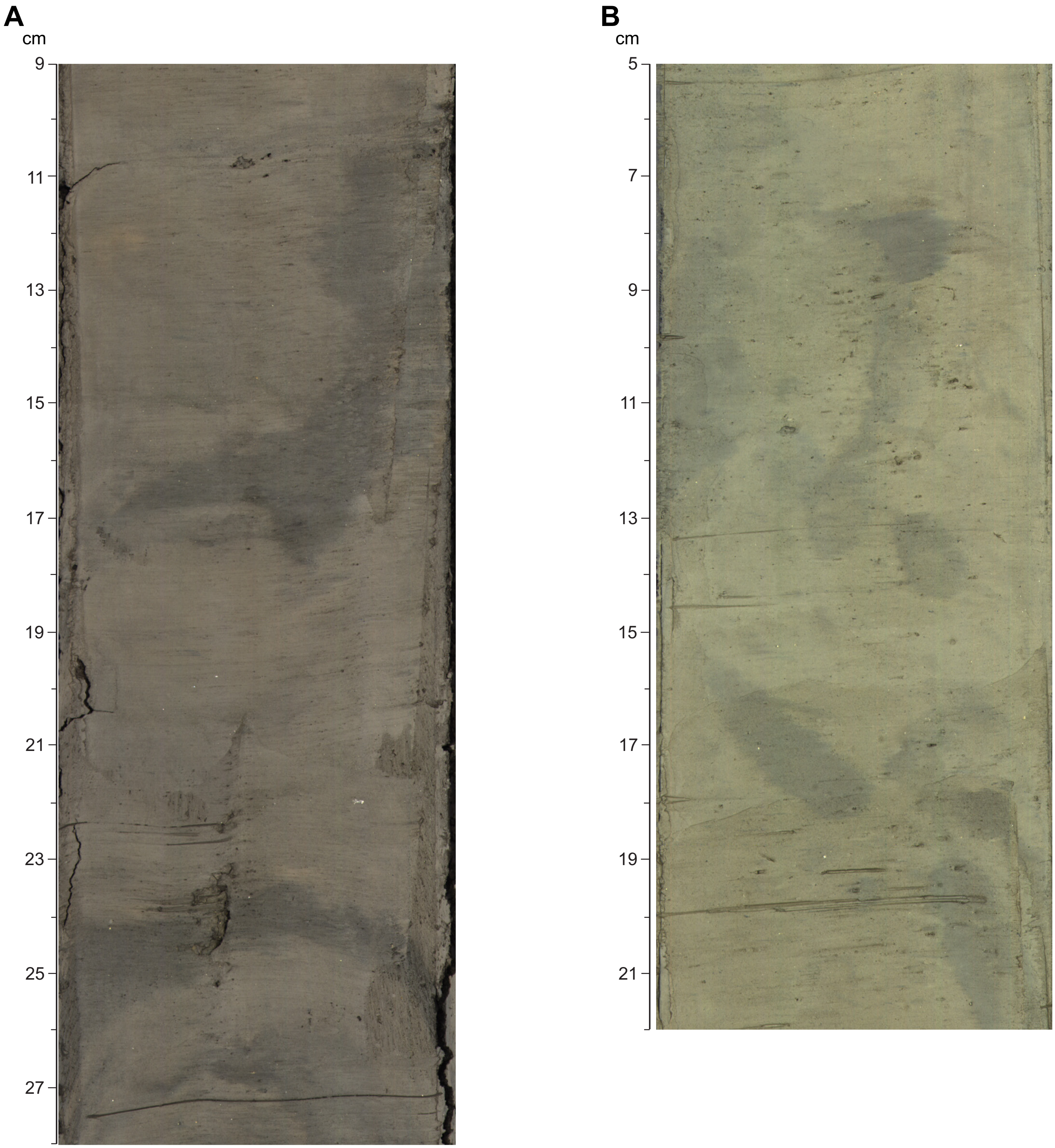

Figure 10. Iron monosulfides (dark black precipitates) infilling burrows; characteristic of Lithostratigraphic Unit I from 0–45 mbsf. A, Section NGHP-01-14A-06H-2, 9–28 cm. B, Section NGHP-01-14A-02H-6, 5–22 cm. [mbsf, meters below sea floor]

carbonate precipitation or a change in the sedimentation rate within this interval. The third zone is characterized by a clear monotonic decrease in sulfate concentrations from 14.73 mM at 15 mbsf to depletion at 23.4 mbsf with a concomitant linear increase in alkalinity to 19.8 mM at the SMI and the first detectable head-space methane concentrations (see “Organic Geochemistry”). The linear decrease in sulfate and increase in alkalinity reflects anaerobic methane oxidation coupled to sulfate depletion and will be employed to compute upward methane fluxes at this site.

If there were no precipitation of authigenic carbonates at the SMI, then alkalinity would increase to approximately 40 mM within this interval, however the value of ~20 mM at the SMI indicates carbonate precipitation. Below the SMI, alkalinity concentrations remain relatively constant to the base of the hole, while SO_4^{2-} values remain depleted with spikes in SO_4^{2-} concentrations reflecting contamination of samples by drilling fluid. At all of the other sites cored in the Krishna-Godavari Basin, alkalinity becomes progressively depleted to the depth of the BSR, indicating that the alkalinity is not controlled by the same removal process at this site, but rather appears to reflect concentrations at the SMI with little to no subsequent removal by precipitation at depth. The alkalinity profile at this site will be key to deciphering the alkalinity removal processes operating at the other sites in this region.

Bromide Concentrations

Bromide concentrations are not typically measured shipboard during IODP/ODP cruises. During Leg 3 of NGHP Expedition 01, an ion chromatograph was utilized to measure both SO_4^{2-} and Br^-. Bromide concentrations in pore waters are sensitive to organic matter diagenesis, with concentrations higher than seawater reflecting marine organic matter decomposition. Since, gas hydrate was inferred to be present in a substantial amount of the samples at this site, Br^- concentrations have been normalized to Cl^- to dampen the influence of gas-hydrate dissociation on the Br^- concentration depth profile (fig. 11). In Hole NGHP-01-14A, Br^-/Cl^-- remains near seawater value (0.00154) from the seafloor to the SMI at 23.4 mbsf. Below the SMI, Br^-/Cl^- increases abruptly from 0.00166 to 0.00251 (~40 percent greater than seawater value) at 56.6 mbsf. Below 56.6 mbsf, the Br^-/Cl^- ratio is relatively constant to the base of the hole with variability in Br^- concentrations in the middle and lower portion of the profile likely reflecting varying amounts of terrestrial organic matter which does not contribute a significant amount of Br^- to the pore fluids during organic matter diagenesis compared with marine organic matter.

Organic Geochemistry

Organic geochemical studies at Site NGHP-01-14 (GDGH-14A) included analysis of the composition of volatile hydrocarbons including methane, ethane, and propane (C_1–C_3) and fixed natural gases (that is, O_2, CO_2, and N_2+Ar) from headspace, void gas, and PCS degassing experiments. In general, these analyses indicate that methane and carbon dioxide are the predominant gases found in the cores at Site NGHP-01-14. Ethane was measurable in void gas samples from a range of depths, typically below 60 mbsf. The headspace samples of sections overlying the SMI were dominated by air and slightly depleted in carbon dioxide. Methane was moderately enriched below the SMI and above the seismically-inferred BSR.

Headspace gas analyses were performed on forty-five samples from Site NGHP-01-14A ranging in depth from 1.35 to 172.95 meters below seafloor (mbsf). The concentrations given here represent minimum proxy measurements of the actual concentrations due to limitations of the gas headspace method (Kvenvolden and Lorenson, 2000). The sediment pore water contained methane at concentrations ranging from non-detectable near the surface to 5.24 mM at ~28 mbsf (table 5). Theoretical methane saturation in pore water under site-specific physical conditions, calculated using the Duan and others (1992) and Xu (2002, 2004) methodologies, ranges from 70.7 mM at the seafloor to 114.2 mM at 120 mbsf, then declines to 113.7 mM near the borehole completion depth of 180 mbsf. $C_2 – C_3$ hydrocarbon gases were not detected in headspace samples suggesting a biogenic source of methane. Methane concentrations increase step-wise from non-detectable to 0.4 mM at 23.4 mbsf, then to 5.2 mM at 27.6 mbsf, corresponding to the SMI (see “Inorganic geochemistry”; fig. 12). Below the SMI, methane concentrations gradually decreased to nearly 1 mM just below the BSR. Methane concentrations increased 1–2 mM at ~40 m below the BSR, which is likely to be associated with the presence of free gas in this interval. The presence of free gas is also inferred from well logs (see “Downhole logging”). The headspace methane concentrations were generally more than an order of magnitude below pore-water saturation throughout the length of the borehole (fig. 12).

Carbon dioxide (CO_2) concentrations ranged from 0.2 to 11.5 mM in pore water contained within the sediment. An equivalent concentration expression of gas volume to sediment volume ranges from ~3,120 to nearly 112,200 microliters CO_2/liter wet sediment (table 5). CO_2 concentrations show an increase from seafloor through the SMI to ~75 mbsf, and then gradually decrease with depth. Two measurements at ~160 mbsf exhibit enriched CO_2 concentrations, which also coincide with the increase in methane noted above (figs. 12 and 13). No apparent change in lithology could be inferred at or near this interval. In general, the results can be roughly divided into three zones based on gas concentration. The lowest concentrations are found above the SMI at a depth ranging from 0 to 15 mbsf (fig. 13). Intermediate CO_2 concentrations were found in the entire interval below the SMI; however, they are probably not associated with gas hydrate given the methane concentrations. Below the BSR, CO_2 concentrations generally decline to less than 3 mM; however, these concentrations are above surficial levels. The methane to carbon dioxide ratio did not reflect these zones. Instead, this ratio exhibits a slight decreasing trend with depth, perhaps indicating that methane may not be preferentially concentrated in relation to carbon dioxide between the SMI and

Table 3. Coarse fraction (>63 µm) sieve data for Hole NGHP-01-14A.

Core, section, depth (cm, in section)	MBSF	Quartz	Feldspar	Mica	Heavy minerals	Volcanic glass	Pyrite	Iron sulfides	Framboidal pyrite	Rock fragments	Authigenic carbonates
NGHP-01-14A											
1H-1,39.5	0.395			trace			2		5		
1H-2,111	2.61			trace			1		5		
2H-2,70	6.77			trace					5		
2H-7,14	13.14								5		
2H-6,57	12.57			trace			5		5		
3H-2,110	16.6						trace		5		
3H-7,54	23.04								100		
4H-1,113	24.63			trace					85		
4H-3,83	27.33			trace					75		
4H-3,97.5	27.475	40		5			5		5		
5H-2,107	35.57	80		10	trace		5				
5H-6,11	40.61	8		2			20		5		
5H-6,16	40.65	1		7			5				
6H-2,55	44.55	45	20	15	9		4	2		1	1
6H-2,140	45.4	10		5	1		2				
6H-7,67	52.14	70	5	7	5				3	1	1
8H-4,19	65.36	10					5		5		
9P-1,9	71.09	70		trace			10				
10Y-1,20	72.2			trace			3		6		
11X-1,69	73.69	10		trace			25		trace		
12X-1,124	83.84						80				
13X-4,62	97.32	80					7				
14P-1,2	100.02	85					10				
16X-1,34	102.34	80		5			10		3		
16X-6,82	109.84	45		5			10				
17X-1,42	112.02	83		7			5				
18X-1,37	121.57	80		5			10				
19X-1,99	131.79	85		2	5						
19X-5,44	136.91	80		5			5				
20X-2,57	141.46	80		5	5		5				
20X-3,100	143.37	80		5	5		2				
21X-1,104	151.04	85		5	7						
21X-5,80	156.8	23		5	3		2				
22X-2,35	161.45	80		10	5		2				
23X-3,40	172.6	85			7		5				
23X-6,50	177.2	5			45		45				

Table 3. Coarse fraction (>63 µm) sieve data for Hole NGHP-01-14A.—Continued

Core, section, depth (cm, in section)	Fora-minifera	Carbonate shell fragments	Dia-toms	Radio-larians	Silico-flagellates	Siliceous shell fragments	Sponge spicules	Other biogenic	Plant debris	Comments
NGHP-01-14A—Continued										
1H-1,39.5	91	2								
1H-2,111	92	2								
2H-2,70	92	3								
2H-7,14	80							10	5	Other biogenic is sea urchin remains
2H-6,57	90									
3H-2,110	90							5	trace	Other biogenic is gastropods
3H-7,54										
4H-1,113		5							10	
4H-3,83	20	5								
4H-3,97.5	40	5						trace		Brachipod
5H-2,107	2								3	Amphibole present
5H-6,11	50	10							5	
5H-6,16	7	80								
6H-2,55	3	trace						trace		Other biogenic is fish remains
6H-2,140	40					40			2	
6H-7,67	5					2			1	
8H-4,19	70	7							3	
9P-1,9		20								
10Y-1,20	90							1	trace	Other biogenic is gastropods
11X-1,69	60								5	
12X-1,124	15	5								
13X-4,62	10								3	
14P-1,2	5									
16X-1,34									2	
16X-6,82	5	5							30	
17X-1,42	2								3	
18X-1,37	5									
19X-1,99	5	3								
19X-5,44	5	5								
20X-2,57	5									
20X-3,100	2								2	
21X-1,104	3	trace								
21X-5,80	60	6						1		Other biogenic is fish remains
22X-2,35	2	1								
23X-3,40		3								
23X-6,50		5								

Table 4. Interstitial-water data for Hole NGHP-01-14A.

[“–”, the value was not determined; bdl, below detection limit]

Sample name	Depth (mbsf)	V samp (mL)	pH	Alk (mM)	Salinity	Cl^- by IC (mM)
1H-1,140-150	1.4	30	7.7	10.46	35.5	560
1H-2,140-150	2.9	30	7.6	13.55	35.0	555
1H-3,128-138	4.3	30	7.7	14.92		558
2H-1,140-150	5.9	30	7.9	16.00	35.8	547
2H-2,140-150	7.4	30	7.9	15.97	35.5	549
2H-3,140-150	8.9	30	7.7	15.17	35.5	561
2H-4,140-150	10.4	30	7.6	13.95	35.5	554
2H-5,140-150	11.9		7.6	12.81		556
2H-6,90-100	12.9	30	7.4		34.5	561
2H-7,91-101	13.9	30	7.8	12.36		552
3H-1,140-150	15.4	30	7.9	11.21	35.0	561
3H-2,140-150	16.9	32	8.0	11.86	34.5	548
3H-3,140-150	18.4	30	7.9	12.53	34.5	565
3H-4,140-150	19.9	28	7.6	14.42	34.5	560
3H-5,140-150	21.4	29	7.7	16.12	34.0	554
3H-6,90-100	22.4	21	8.0	18.45	33.0	546
3H-7,90-100	23.4	24	7.9	19.83	32.5	551
4H-3,140-150	27.9	25	8.2	22.09	32.5	540
4H-5,140-150	30.9	24	8.0	23.86	33.0	543
5H-3,140-150	37.4	26	7.7	22.17	32.5	515
5H-5,140-150	40.4	24	7.9	23.15	32.8	551
6H-3,130-150	46.8	20	8.0	24.17	32.5	545
6H-5,118-138	49.7	20	8.0		32.5	540
6H-6,106-132	50.9	33	8.0	23.12	32.5	546
7H-3,125-145	56.2	20	7.9	26.00	32.8	546
7H-5,130-150	59.2	21	7.9	23.96	32.5	552
8H-3,127-147	65.0	14			32.0	537
8H-5,130-150	67.6	19	7.8	25.35	31.8	533
9P-1,20-30	71.2	9			30.8	517
10Y-1,66-88	72.7	14				542
11X-2,113-136	75.6	17	8.1	25.43	31.0	513
11X-2,113-136	75.6	17	8.1	25.80	32.0	545
11X-3,130-150	77.2	19	7.8	28.70	32.0	551
12X-3,95-105	86.1	16	7.9	21.62	30.0	419
12X-3,105-115	86.2	20	7.8	30.23	33.0	493
12X-5,130-150	89.1	18	8.0	29.45	32.0	542
13X-3,130-150	96.5	18	8.2	28.80	33.0	534
13X-5,130-150	99.5	22	8.1	26.41	33.0	539
14P-1,40-52	100.4	11			32.0	541
15E-1,0-19	101.0	16	8.3	17.59	33.5	538
16X-2,60-90	104.1	15	8.3	25.12	33.0	543
16X-2,60-90	104.1	22	8.1	26.29	33.0	542
16X-4,120-150	107.7	20	8.1	25.24	33.5	543
17X-1,109-139	112.7	16	8.3	23.36	33.0	541
18X-1,70-100	121.9	25	8.2	26.09	33.5	540
18X-2,86-116	123.1	15	8.3	24.14	32.5	528
19X-4,87-117	136.2	20	8.3	25.86	32.5	542
20X-4,82-112	144.7	26	8.2	27.81		543
21X-3,120-150	154.2	21	8.2	24.47	33.5	536
22X-2,120-150	162.3	18	8.0	23.42	32.5	531
23X-3,120-150	173.4	31	8.0	18.41	32.0	535

Table 4. Interstitial-water data for Hole NGHP-01-14A.—Continued

[“-“, the value was not determined; bdl, below detection limit]

Sample name	Br^- (mM)	SO_4^{2-} (mM)	Comments	Alk/Cl^-	Br^-/Cl^-	SO42$^-$/Cl^-
1H-1,140-150	0.88	22.27		0.01869	0.00158	0.03978
1H-2,140-150	0.88	18.51		0.02441	0.00159	0.03335
1H-3,128-138	0.89	17.14		0.02673	0.00160	0.03071
2H-1,140-150	0.88	15.23		0.02923	0.00160	0.02782
2H-2,140-150	0.87	14.57		0.02907	0.00158	0.02652
2H-3,140-150	0.88	14.32		0.02703	0.00157	0.02552
2H-4,140-150	0.91	14.23		0.02517	0.00164	0.02566
2H-5,140-150	0.89	13.86		0.02302	0.00161	0.02492
2H-6,90-100	0.87	13.79			0.00155	0.02458
2H-7,91-101	0.90	13.17		0.02239	0.00164	0.02387
3H-1,140-150	0.89	14.73		0.02000	0.00158	0.02627
3H-2,140-150	0.87	12.63		0.02164	0.00159	0.02306
3H-3,140-150	0.91	11.32		0.02218	0.00162	0.02004
3H-4,140-150	0.92	8.26		0.02575	0.00163	0.01475
3H-5,140-150	0.90	4.59		0.02912	0.00163	0.00829
3H-6,90-100	0.92	1.55		0.03379	0.00169	0.00285
3H-7,90-100	0.92	0.07		0.03596	0.00166	0.00013
4H-3,140-150	0.95	0.10		0.04089	0.00177	0.00018
4H-5,140-150	1.03	0.04		0.04392	0.00190	0.00008
5H-3,140-150	1.09	0.11		0.04300	0.00210	0.00022
5H-5,140-150	1.23	0.04		0.04198	0.00224	0.00007
6H-3,130-150	1.31	0.00		0.04434	0.00240	0.00000
6H-5,118-138	1.31	0.00			0.00243	0.00000
6H-6,106-132	1.33	0.04	IR anomaly	0.04232	0.00244	0.00008
7H-3,125-145	1.37	0.08	Strong IR anomaly	0.04764	0.00251	0.00015
7H-5,130-150	1.39	0.00		0.04341	0.00252	0.00000
8H-3,127-147	1.41	0.06	Abundant authigenic carbonates		0.00263	0.00011
8H-5,130-150	1.37	0.00		0.04753	0.00256	0.00000
9P-1,20-30	1.28	1.35			0.00247	0.00261
10Y-1,66-88	1.44	0.67			0.00266	0.00124
11X-2,113-136	1.28	0.35	IR anomaly, small pieces of hydrate	0.04962	0.00250	0.00069
11X-2,113-136	1.41	0.11	Background	0.04733	0.00258	0.00021
11X-3,130-150	1.45	0.06		0.05210	0.00263	0.00010
12X-3,95-105	1.18	4.36	IR anomaly, corrected for seawater contamination	0.05159	0.00281	0.01040
12X-3,105-115	1.35	0.05		0.06134	0.00273	0.00011
12X-5,130-150	1.43	0.10		0.05430	0.00263	0.00019
13X-3,130-150	1.39	0.10	Abundant authigenic carbonates	0.05396	0.00260	0.00019
13X-5,130-150	1.39	0.49		0.04902	0.00257	0.00091
14P-1,40-52	1.44	0.04			0.00266	0.00007
15E-1,0-19	1.18	7.63		0.03269	0.00220	0.01418
16X-2,60-90	1.43	0.17	Strong IR anomaly	0.04629	0.00263	0.00031
16X-2,60-90	1.43	0.05	Moderate IR anomaly; background	0.04846	0.00264	0.00010
16X-4,120-150	1.43	0.07	Large carbonate nodules	0.04650	0.00264	0.00012
17X-1,109-139	1.50	0.06		0.04314	0.00277	0.00010
18X-1,70-100	1.43	0.28	~3 cm diameter carbonate nodules	0.04830	0.00265	0.00053
18X-2,86-116	1.41	0.26	Interbedded silts to fine sands; carbonate nodules	0.04576	0.00267	0.00048
19X-4,87-117	1.51	0.06		0.04773	0.00279	0.00011
20X-4,82-112	1.48	0.07		0.05122	0.00273	0.00013
21X-3,120-150	1.46	0.08		0.04561	0.00271	0.00014
22X-2,120-150	1.47	0.10		0.04414	0.00276	0.00019
23X-3,120-150	1.48	0.07		0.03439	0.00277	0.00014

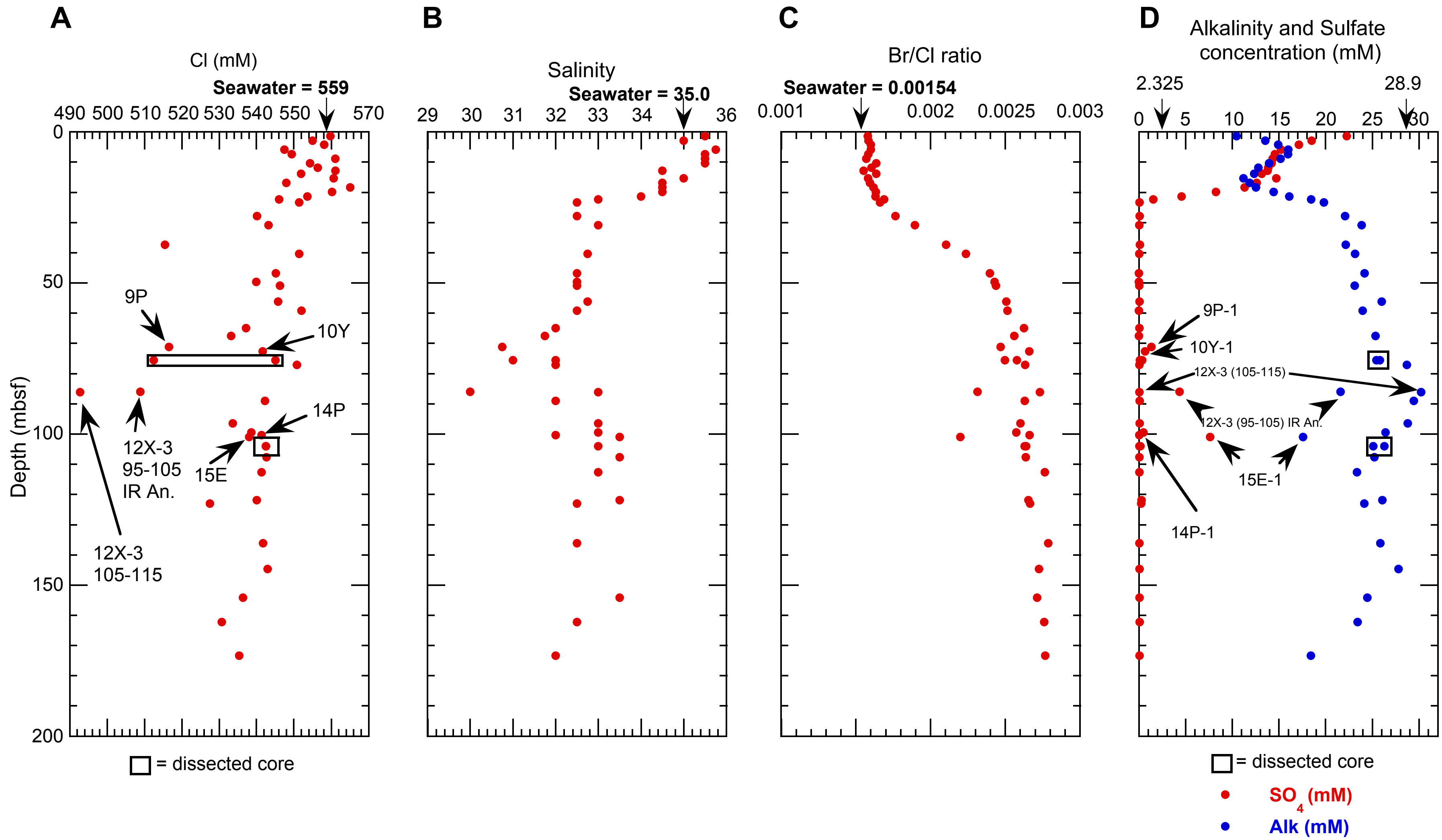

Figure 11. Interstitial water composition depth profiles of A, chloride determined via ion chromatography (error is ±0.7 percent); B, salinity; C, Br^-/Cl^- ratio; and D, sulfate and alkalinity (red circles represent Hole NGHP-01-14A sulfate concentrations and blue circles represent alkalinity) at Hole NGHP-01-14A.

BSR (fig. 14). The air gases (N_2+Ar), and O_2 were the balance gases; however, the (N_2+Ar)/O_2 ratios were typically greater than air which may reflect the ratio in the sediment, as well as air that was trapped in the headspace samples. Air gases are present in all samples as the core plugs were degassed in an air headspace.

Void gas samples were collected from thirteen different intervals ranging in depth from 32.8 to 145.2 mbsf. The void gas samples contained methane above 52 percent at all intervals, as noted in table 6. Methane concentrations within voids averaged nearly 886,000 ppm (±176,000). Carbon dioxide concentrations ranged from ~1,800 to 11,500 ppmv and are tabulated with other gas data in table 6. The methane to carbon dioxide ratios were fairly uniform with increasing depth, indicating that any existing gas hydrate may have concentrated the methane relative to carbon dioxide with depth (fig. 14). This is particularly the case for two samples between the interval 45–60 mbsf, and one sample just above the BSR, where methane levels were enriched 2 to 5 fold above background. Void gases exhibited the presence of low level C_2 concentrations, ranging from non-detectable to 48 ppmv. Note that headspace C_1/CO_2 is typically 2 orders of magnitude less due to the preferential loss of volatile methane by the headspace sample method (fig. 14). Ratio values for C_1 to C_2 gases ranged from ~19,900 to ~49,200 ppmv (average 30,712 ppmv), and showed no apparent trend with depth (fig. 15). The concentrations are focused near the high organic matter portion of the 'normal' occurrence interval as depicted in the graph. The air gases (N_2+Ar), and O_2 composed the balance gases and along with the (N_2+Ar)/O_2 ratios reflect air contamination plus *in situ* sediment concentrations.

Gas was collected from one PCS in Hole NGHP-01-14A (table 7). The gas concentration results are very similar to the void gas results (table 6), as exhibited by C_1/CO_2 ratio (fig. 14). The PCS gas results confirmed the slight enrichment of methane just above the BSR, which is likely due to the presence of a free gas and(or) gas hydrate in this interval, as other proxy measurements indicated (see "Downhole Logging"). PCS core gases did not indicate the presence of C_2 concentrations. These high methane concentrations versus low concentrations of ethane are strong evidence of a microbially-dominated hydrocarbon gas source.

Microbiology

Hole NGHP-01-14A

Analysis of all microbiological samples will be shore-based. Nineteen samples were collected for CEL, and 19 for SPH, one 30 cm section identified as anomalous on the IR scan of the core (MAF, MAG, MAR) for detailed microbiological studies and one 30 cm section identified as background (MBF, MBG, MBR) (table 8). The 30 cm sections were split into 3 subsections as described in the "Methods" section. Additional microbiological samples were taken (Lab code JUD, 28 samples; Lab code JAN, 18 samples). Samples were collected as described in the "Methods" section.

Physical Properties

Whole-round cores at NGHP Expedition 01, Site 14 were imaged using an infrared (IR) camera on the catwalk to determine the location of temperature anomalies on the surface of core liners and enable sections containing gas hydrate to be quickly removed, preserved, and studied. After IR imaging was finished, non-destructive measurements were conducted on temperature-equilibrated whole-round core sections with the MSCL. Thermal conductivity measurements were also conducted on whole-round cores. Various tests were performed on split cores including: electrical resistivity by use of a Wenner array, P-wave velocity by inserted spades, and shear strength by mini-vane, Torvane, and Pocket Penetrometer. Core subsamples were placed in 10-mL beakers and dried at 105 °C to determine water content. Subsequently, the dried samples were analyzed for grain density using gas pycnometers and other sediment parameters were then calculated. See the "Physical Properties" section of the "Methods" chapter for more details.

The physical properties program at Site NGHP-01-14 was conducted on samples recovered from Hole NGHP-01-14A in the Krishna-Godavari Basin located about 35 km off the eastern coast of India in 895 m of water. A preliminary well using LWD technology was not drilled at this site; however, a wireline logging program was conducted after drilling and coring. Hole NGHP-01-14A was continuously cored to about 180 mbsf and overall core recovery was 85 percent.

Infrared Imaging

Environmental Conditions

The catwalk environment was monitored during the entire drilling operation at Site NGHP-01-14 for temperature and humidity. Temperature on the catwalk ranged from 30.0 to 32.5 °C during the drilling operation that lasted approximately 30 hr, as shown in figure 16. Percent relative humidity ranged between 62 and 86 percent (fig. 16), consistent with a marine setting in the Indian Ocean. No adverse environmental conditions such as thunderstorms, rough seas, lightning, or high winds, persisted during drilling operations at this site. Also presented in figure 16 are the relative times at which each core was transferred onto the catwalk from the drill floor.

Table 5. Headspace gas (HS) composition for Site NGHP-01-14.

Sample	Site	Hole	Core	Section	Interval (cm)	Sed wt. (g)	Sample depth (mbsf)	CO_2 (ppm-v)	C_1	C_2	C_3
14A-1H1-135-140	14	A	1	1	135–140	9.4	1.35	3,400	nd	nd	nd
14A-1H2-135-140	14	A	1	2	135–140	7.7	2.85	1,400	nd	nd	nd
14A-1H3-83-88	14	A	1	3	83–88	7.4	3.83	1,100	nd	nd	nd
14A-2H1-135-140	14	A	2	1	135–140	11.7	5.85	14,200	nd	nd	nd
14A-2H2-135-140	14	A	0	2	135–140	9.3	7.35	13,000	nd	nd	nd
14A-2H3-105-110	14	A	2	3	105–110	8.6	8.55	2,200	nd	nd	nd
14A-2H4-135-140	14	A	2	4	135–140	12.0	10.35	5,000	nd	nd	nd
14A-2H5-95-100	14	A	2	5	95–100	10.1	11.45	10,300	nd	nd	nd
14A-2H6-85-90	14	A	2	6	85–90	8.3	12.85	17,300	nd	nd	nd
14A-2H7-86-91	14	A	2	7	86–91	7.7	13.86	3,900	nd	nd	nd
14A-3H1-135-140	14	A	3	1	135–140	6.7	15.35	1,300	nd	nd	nd
14A-3H2-135-140	14	A	3	2	135–140	6.0	16.85	1,500	nd	nd	nd
14A-3H3-105-110	14	A	3	3	105–110	6.0	18.05	1,300	nd	nd	nd
14A-3H4-135-140	14	A	3	4	135–140	5.9	19.85	1,500	nd	nd	nd
14A-3H5-95-100	14	A	3	5	95–100	12.2	20.95	13,900	nd	nd	nd
14A-3H6-85-90	14	A	3	6	85–90	9.9	22.35	1,400	nd	nd	nd
14A-3H7-85-90	14	A	3	7	85–90	10.4	23.35	4,700	2,800	nd	nd
14A-4H3-105-110	14	A	4	3	105–110	7.8	27.55	14,700	23,500	nd	nd
14A-4H5-95-100	14	A	4	5	95–100	8.8	30.45	28,900	22,000	nd	nd
14A-5H3-105-110	14	A	5	3	105–110	9.1	37.05	6,800	2,500	nd	nd
14A-5H5-95-100	14	A	5	5	95–100	8.3	39.95	3,600	6,900	nd	nd
14A-6H3-95-100	14	A	6	3	95–100	12.0	46.45	38,200	14,700	nd	nd
14A-6H5-73-78	14	A	6	5	73–78	7.1	49.23	26,300	10,700	nd	nd
14A-7H3-90-95	14	A	7	3	90–95	9.2	55.83	5,700	3,200	nd	nd
14A-7H5-85-90	14	A	7	5	85–90	8.0	58.73	34,300	8,200	nd	nd
14A-8H3-92-97	14	A	8	3	92–97	10.6	64.62	2,100	1,600	nd	nd
14A-8H5-85-90	14	A	8	5	85–90	11.3	67.12	30,500	10,300	nd	nd
14A-9P-15-20	14	A	9	P	15–20	13.9	71.15	6,100	6,000	nd	nd
14A-11X2-78-83	14	A	11	2	78–83	9.7	75.28	22,600	10,300	nd	nd
14A-11X3-120-125	14	A	11	3	120–125	6.6	77.06	17,100	4,500	nd	nd
14A-12X3-60-65	14	A	12	3	60–65	11.0	85.70	32,500	9,900	nd	nd
14A-12X5-85-90	14	A	12	5	85–90	8.8	88.60	36,900	10,100	nd	nd
14A-13X3-95-100	14	A	13	3	95–100	10.5	96.15	21,600	8,600	nd	nd
14A-13X5-85-90	14	A	13	5	85–90	7.8	99.05	17,400	6,300	nd	nd
14A-14P-52-57	14	A	14	P	52–57	9.9	100.52	26,100	11,100	nd	nd
14A-16X2-25-30	14	A	16	2	25–30	8.4	103.75	17,500	7,800	nd	nd
14A-16X4-75-80	14	A	16	4	75–80	9.6	107.25	16,300	5,300	nd	nd
14A-17X1-84-94	14	A	17	1	84–94	8.8	112.44	19,400	5,700	nd	nd
14A-18X1-65-70	14	A	18	1	65–70	10.0	121.85	11,000	6,200	nd	nd
14A-18X2-41-46	14	A	18	2	41–46	9.3	122.61	17,900	4,400	nd	nd
14A-19X4-42-47	14	A	19	4	42–47	9.5	135.72	10,100	5,100	nd	nd
14A-20X4-75-80	14	A	20	4	75–80	10.4	144.26	8,200	5,000	nd	nd
14A-21X3-75-80	14	A	21	3	75–80	11.0	153.75	39,100	8,200	nd	nd
14A-22X2-75-80	14	A	22	2	75–80	11.9	161.85	68,100	11,000	nd	nd
14A-23X3-75-80	14	A	23	3	75–80	11.4	172.95	10,500	4,800	nd	nd

Table 5. Headspace gas (HS) composition for Site NGHP-01-14.—Continued

Sample	O_2	N_2+Ar	H_2S	C_1 (mL/L WS)	C_1 (mM PW)	CO_2 (mL/L WS)	CO_2 (mM PW)	C_1/CO_2
14A-1H1-135-140	192,100	753,900	nd	nd	nd	7,900	0.4	-
14A-1H2-135-140	183,100	755,200	nd	nd	nd	4,300	0.2	-
14A-1H3-83-88	187,700	745,000	nd	nd	nd	3,700	0.2	-
14A-2H1-135-140	183,400	756,800	nd	nd	nd	24,100	1.4	-
14A-2H2-135-140	187,700	750,200	nd	nd	nd	30,900	1.8	-
14A-2H3-105-110	191,700	746,400	nd	nd	nd	5,900	0.4	-
14A-2H4-135-140	186,700	749,500	nd	nd	nd	8,100	0.5	-
14A-2H5-95-100	181,200	750,800	nd	nd	nd	21,800	1.4	-
14A-2H6-85-90	183,600	749,400	nd	nd	nd	48,500	3.1	-
14A-2H7-86-91	188,400	746,500	nd	nd	nd	12,000	0.8	-
14A-3H1-135-140	192,900	749,600	nd	nd	nd	4,900	0.3	-
14A-3H2-135-140	191,500	748,800	nd	nd	nd	6,200	0.4	-
14A-3H3-105-110	192,200	743,800	nd	nd	nd	5,400	0.4	-
14A-3H4-135-140	193,400	752,100	nd	nd	nd	6,600	0.5	-
14A-3H5-95-100	179,800	754,100	nd	nd	nd	22,000	1.6	-
14A-3H6-85-90	192,100	747,500	nd	nd	nd	3,100	0.2	-
14A-3H7-85-90	188,400	754,000	nd	5,600	0.4	9,600	0.7	0.6
14A-4H3-105-110	166,500	754,800	nd	71,500	5.2	44,800	3.3	1.6
14A-4H5-95-100	146,100	760,600	nd	56,700	4.2	74,600	5.6	0.8
14A-5H3-105-110	184,300	745,200	nd	6,100	0.5	16,700	1.3	0.4
14A-5H5-95-100	153,800	732,500	nd	19,200	1.5	10,200	0.8	1.9
14A-6H3-95-100	136,100	776,200	nd	23,900	2.0	62,100	5.1	0.4
14A-6H5-73-78	146,600	766,500	nd	36,700	2.9	90,500	7.2	0.4
14A-7H3-90-95	184,100	744,000	nd	7,700	0.6	13,800	1.1	0.6
14A-7H5-85-90	162,700	730,000	nd	23,900	2.0	100,800	8.4	0.2
14A-8H3-92-97	189,000	752,500	nd	3,200	0.3	4,200	0.4	0.8
14A-8H5-85-90	166,200	756,500	nd	18,400	1.6	54,600	4.8	0.3
14A-9P-15-20	170,900	723,400	nd	7,600	0.7	7,700	0.7	1.0
14A-11X2-78-83	157,700	744,200	nd	23,100	2.0	50,700	4.4	0.5
14A-11X3-120-125	171,100	732,300	nd	17,000	1.5	64,500	5.5	0.3
14A-12X3-60-65	157,000	737,300	nd	18,500	1.7	60,600	5.5	0.3
14A-12X5-85-90	156,200	708,400	nd	25,900	2.3	95,300	8.5	0.3
14A-13X3-95-100	163,800	746,500	nd	17,300	1.6	43,200	4.0	0.4
14A-13X5-85-90	168,300	752,400	nd	19,000	1.7	52,800	4.8	0.4
14A-14P-52-57	155,600	738,100	nd	24,200	2.2	56,900	5.2	0.4
14A-16X2-25-30	175,100	726,100	nd	21,400	2.0	48,000	4.4	0.4
14A-16X4-75-80	177,200	733,900	nd	12,000	1.1	37,200	3.4	0.3
14A-17X1-84-94	163,900	755,300	nd	14,800	1.4	50,000	4.6	0.3
14A-18X1-65-70	179,400	760,500	nd	13,400	1.3	23,600	2.2	0.6
14A-18X2-41-46	164,400	759,600	nd	10,600	1.0	42,600	4.0	0.2
14A-19X4-42-47	184,100	757,200	nd	11,800	1.1	23,500	2.3	0.5
14A-20X4-75-80	177,400	743,400	nd	10,200	1.0	16,700	1.6	0.6
14A-21X3-75-80	94,100	799,900	nd	15,300	1.5	72,800	7.3	0.2
14A-22X2-75-80	77,200	808,000	nd	18,100	1.9	112,200	11.5	0.2
14A-23X3-75-80	158,600	766,100	nd	8,500	0.9	18,600	1.9	0.5

Notes: nd = not detected. WS = Wet sediment. PW = porewater. Approximate detection limits are about 15 ppmv for methane, 30 ppmv for ethane, 50 ppmv for propane, and 20 ppmv for hydrogen sulfide.

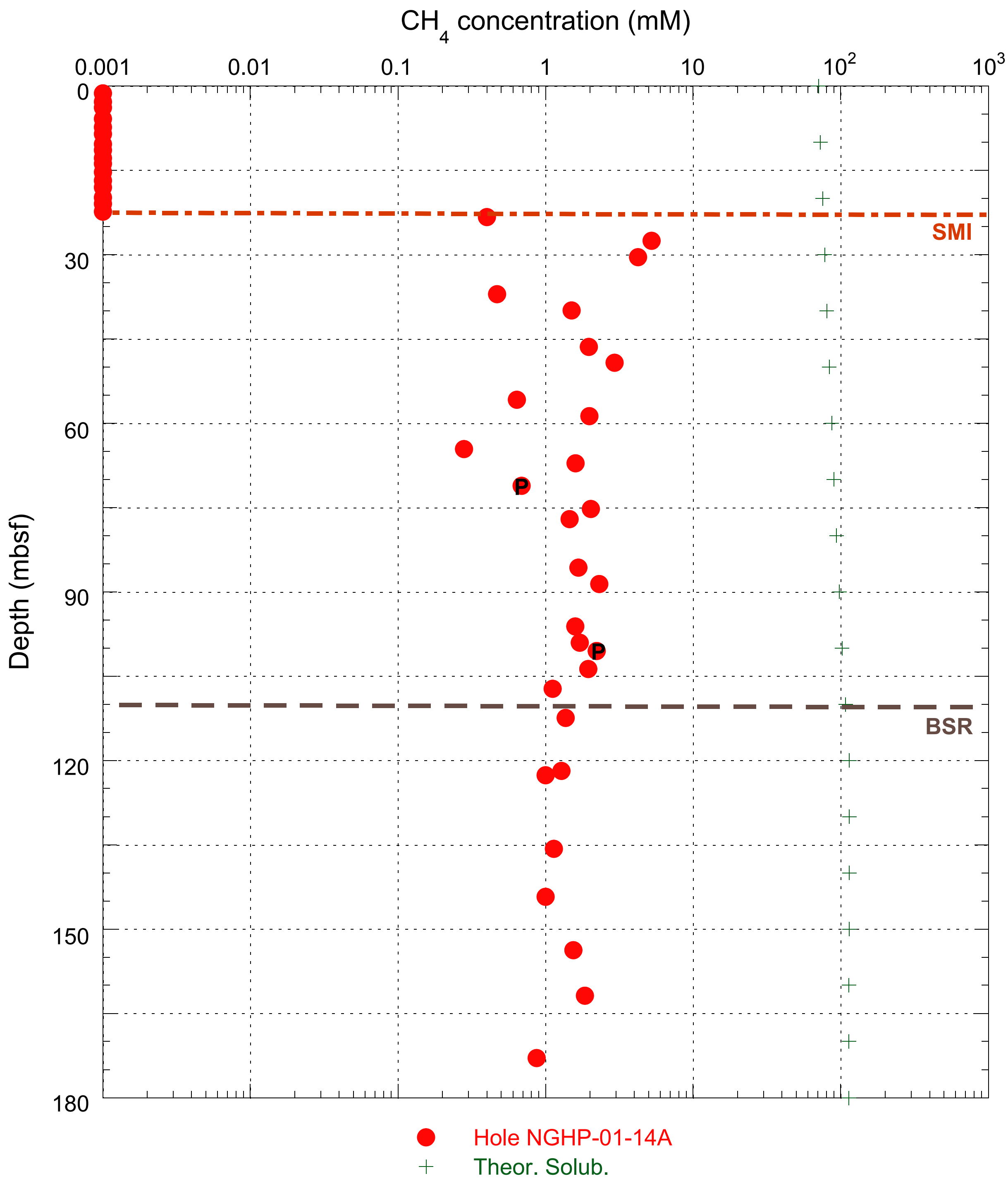

Figure 12. Plot of headspace methane gas concentration (mM) with depth for Hole NGHP-01-14A. Note the methane gradient at ~23 mbsf denoting the SMI. Values less than 0.003 mM are below instrument detection limits but are plotted for reference. Text inside a symbol denotes special coring tool (E, HRC; P, PCS; Y, FPC). Theoretical solubility of methane calculated using the Duan and others (1992) and Xu (2002, 2004) methodologies. [SMI, sulfate-methane interface]

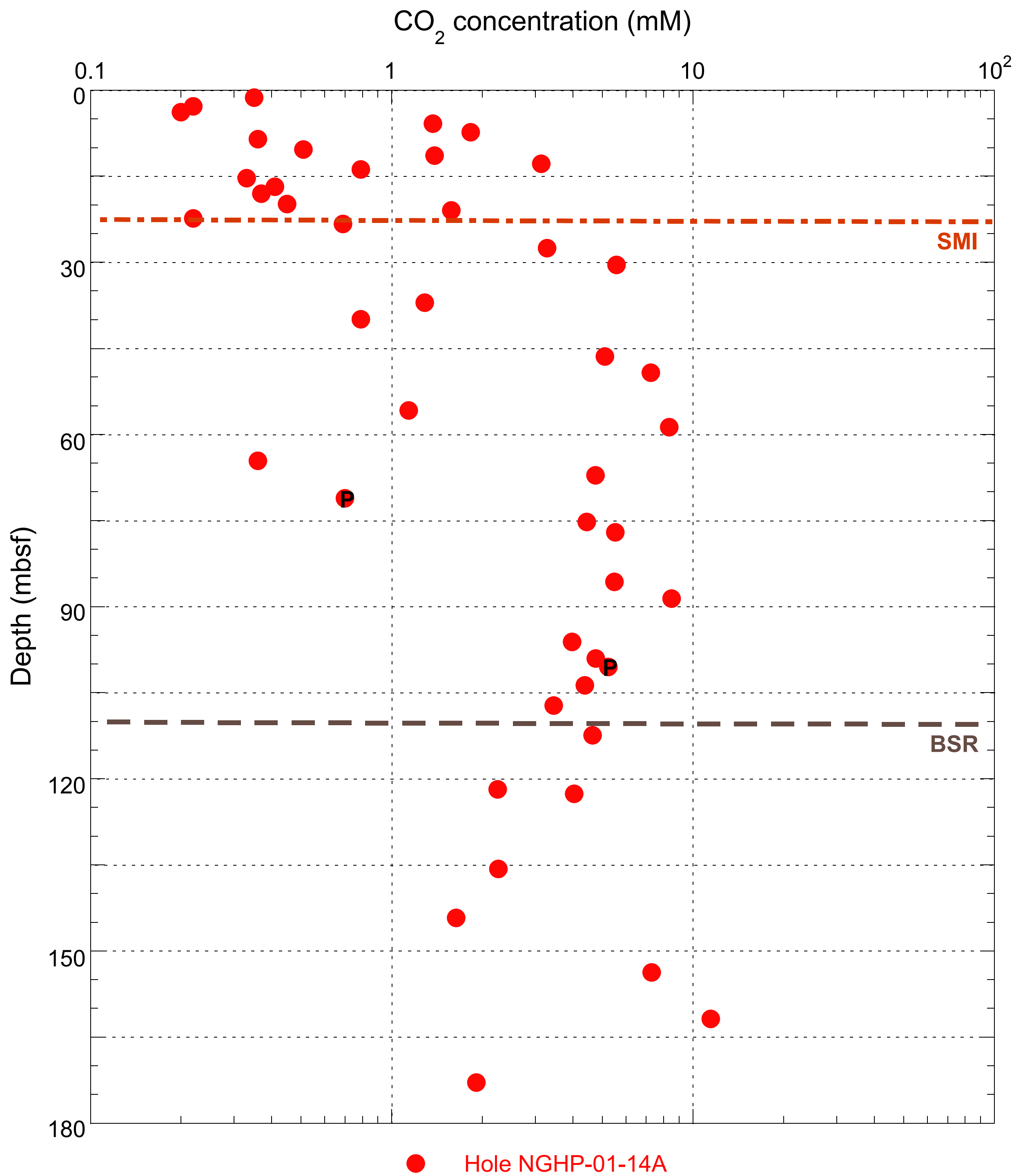

Figure 13. Plot of headspace carbon dioxide gas concentration (mM) with depth for Hole NGHP-01-14A. Text inside a symbol denotes special coring tool (E, HRC; P, PCS; Y, FPC).

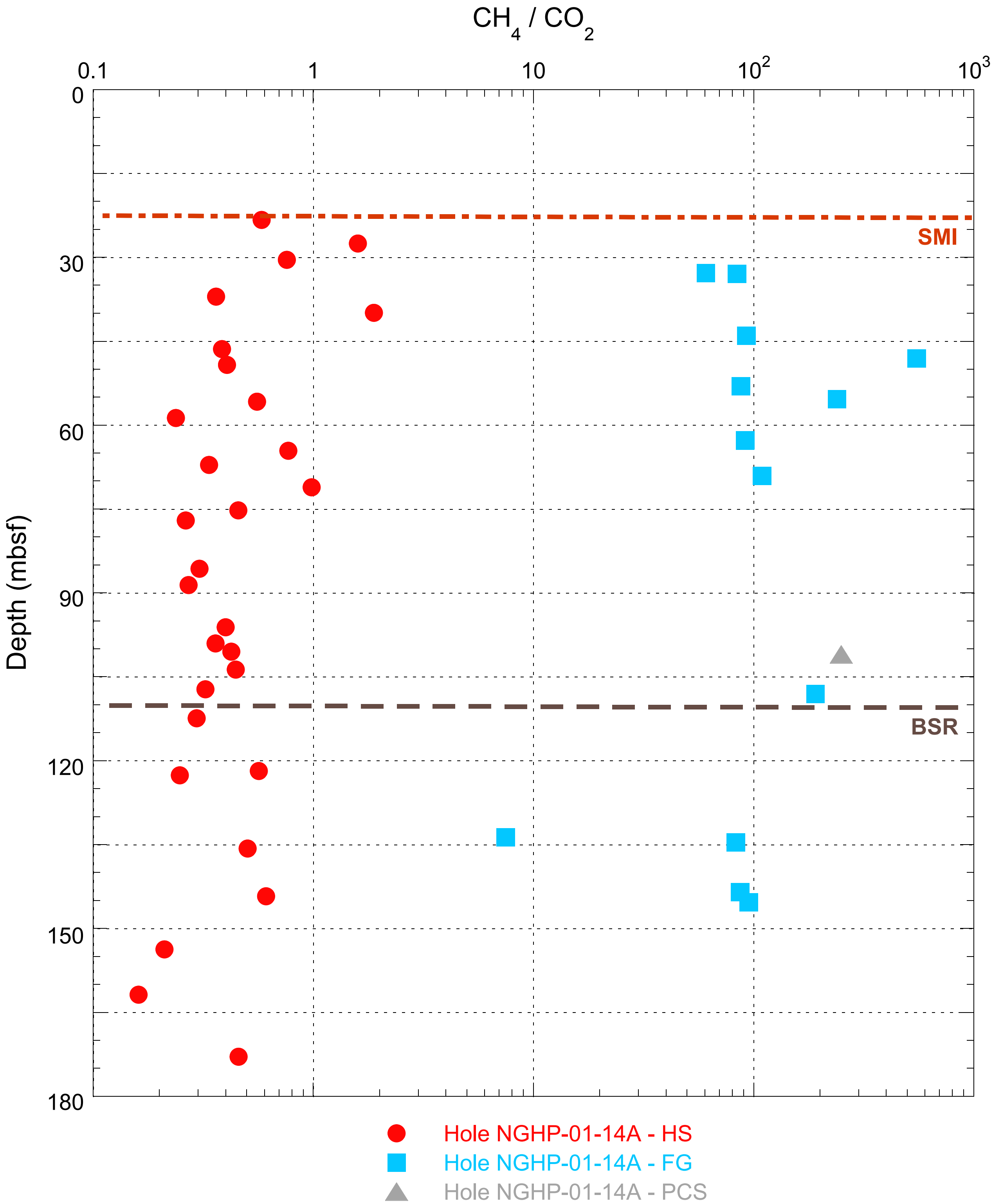

Figure 14. Plot of methane to carbon dioxide gas ratio with depth for headspace, free/void gas, and PCS gas for Hole NGHP-01-14A. Note the localized peaks in methane concentration, perhaps indicating the presence of free gas or gas hydrate. [PCS, Pressure Core Sampler]

Table 6. Void gas (FG) composition for Site NGHP-01-14.

Sample	Site	Hole	Core	Section	Interval (cm)	Sample depth (mbsf)	CO_2	C_1	C_2	C_3	O_2	N_2+Ar	H_2S	C_1/CO_2	C_1/C_2
							(ppmv) normalized to nitrogen+argon								
14A-4H7-31	14	A	4	7	31	32.81	8,800	534,600	nd	nd	96,800	359,800	nd	60	-
14A-4H7-47	14	A	4	7	47	32.97	11,400	960,700	20	nd	2,700	25,100	nd	80	48,000
14A-6H2-4	14	A	6	2	4	44.04	10,500	975,000	nd	nd	4,200	10,200	nd	90	-
14A-6H4-111	14	A	6	4	111	48.11	1,800	994,200	50	nd	1,700	2,300	nd	550	19,900
14A-7H1-106	14	A	0	1	106	53.06	11,200	983,800	nd	nd	1,600	3,400	nd	90	-
14A-7H3-44	14	A	7	3	44	55.37	2,200	527,100	nd	nd	80,900	389,800	nd	240	-
14A-8H2-57	14	A	8	2	57	62.77	10,600	971,300	nd	nd	6,000	12,100	nd	90	-
14A-8H7-27	14	A	8	7	27	69.06	9,000	984,600	20	nd	2,300	4,200	nd	110	49,200
14A-16X5-9	14	A	16	5	9	108.09	5,200	992,300	40	nd	1,000	1,500	nd	190	24,800
14A-19X2-141	14	A	19	2	141	133.71	11,600	965,300	40	nd	7,300	15,700	nd	80	24,100
14A-19X3-84	14	A	19	3	84	134.64	13,100	982,700	40	nd	1,300	2,800	nd	80	24,600
14A-20X3-113	14	A	20	3	113	143.52	11,000	956,800	30	nd	9,900	22,300	nd	90	31,900
14A-20X5-31	14	A	20	5	31	145.32	7,300	695,800	30	nd	66,600	230,200	nd	100	23,200

Notes: nd = not detected. nr = not recorded. Approximate detection limits are about 15 ppmv for methane, 30 ppmv for ethane, 50 ppmv for propane, and 20 ppmv for hydrogen sulfide.

Infrared (IR) Images

All APC and XCB cores from Site NGHP-01-14 were systematically scanned upon arrival on the catwalk using the track-mounted IR camera described in the “Physical Properties” section of the “Methods” chapter. IR anomalies, commonly referred to as “cold spots,” indicate gas-hydrate dissociation during core recovery, which guides catwalk sampling. Summary digital maps of the scans of all cores are available on the data DVD that accompanies this report (tables 9, 10, and 11). Temperature arrays in text-formatted files were exported from the IR camera software and then concatenated for each core. The arrays were then further concatenated for all cores available in a given borehole and down-core temperatures were averaged for each pixel row in the array, excluding pixels ~1 cm from the edge of the image and 2 cm along the midline of the image. Exclusion of these pixels minimized the effects caused by major thermal artifacts in the images. This processing enables us to measure the average amplitude of the cold anomalies and separate warm anomalies due to voids from the background temperature field.

IR track imaging for Hole NGHP-01-14A consisted of 23 scans for a total scanned core length of 177 m. The complete set of IR images collected for Hole NGHP-01-14A is presented in figure 17 along with the corresponding down-core temperatures. The high median core temperature extracted from the IR images for Hole NGHP-01-14A was 30 °C and is related to voids in the core sediment due to gas expansion. The low median temperature of 21.5 °C was produced by small thermal anomalies at ~52, 70, 85, and 105 mbsf. The anomaly at 105 mbsf is ~5 m thick and may reflect a broad zone of pore-filling hydrate or processes other than gas-hydrate dissociation. As shown in figure 17, the measured downcore temperature log generated from the IR imaging shows sediment is initially cooler in the first two cores. Cores below this depth are warmer on average regardless of whether the APC coring technique or XCB coring technique was used. This observation differs from that of Site NGHP-01-07 where core liner temperatures increase with depth. There is no explanation for this difference, but detailed comparison of the IR imaging results from Sites NGHP-01-07 and NGHP-01-14 with other physical property parameters could be useful. Figure 18 provides a comparative down-core plot of core-end temperatures measured on the catwalk with temperature probes (see discussion below)

Thirty-four IR images of the cut ends of core sections were acquired with a hand-held IR camera on the catwalk during sampling activities when possible. Figure 19 is an example of an IR image with a distinct interior cold spot indicating a gas-hydrate occurrence.

Core-End Temperature Readings

To study the temporal and spatial thermal history of recovered cores and assist in the interpretation of IR images, temperature readings were taken on all core ends immediately following the IR track imaging. Typically four temperature probes were inserted approximately 8 cm into the end of each core and allowed to remain there until the core was completely processed and removed from the catwalk. A summary of the core-end temperature results (center position only) for Hole NGHP-01-14A is presented in figure 18. The coldest core-end temperature (12 °C) from Hole NGHP-01-14A was measured in the uppermost core (NGHP-01-14A-01H). Most of the other core-end temperatures vary between 15 °C and 20 °C and typically increase with depth except for the deepest sample at ~120 mbsf.

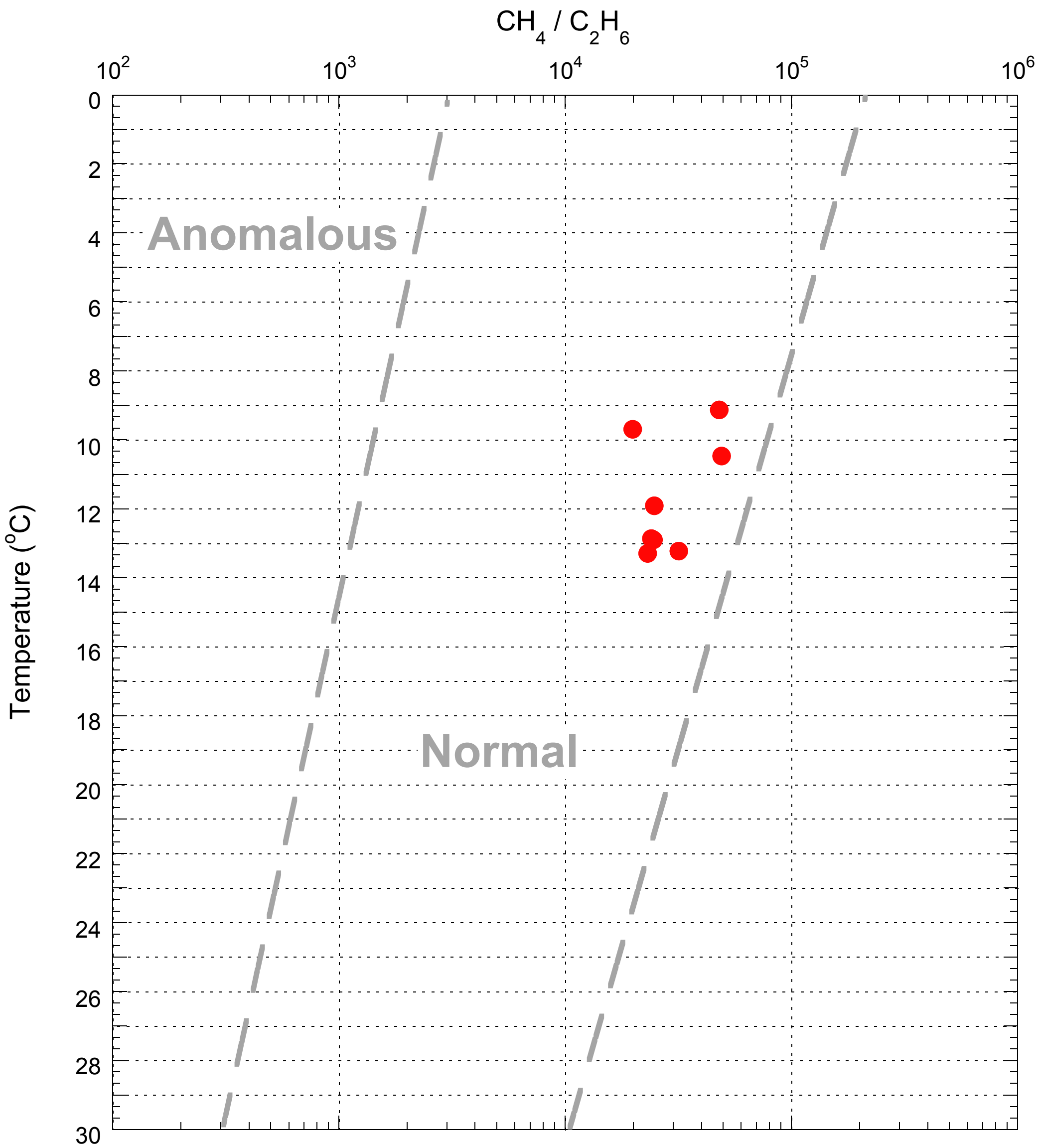

Figure 15. Plot of free/void gas and PCS methane to ethane gas ratio with depth for Hole NGHP-01-14A. Ethane levels were below detection limits for all headspace and PCS samples (tables 5 and 7). Note that the hydrocarbon gas occurrences fall into the typical range. [PCS, Pressure Core Sampler]

Table 7. Pressure Core Sampler gas composition for Site NGHP-01-14.

Sample	Site	Hole	Core	Section	Sample depth (mbsf)	Time	Gas Vol. (ml)	CO_2	C_1	C_2	C_3	O_2	N_2+Ar	H_2S	C_1/CO_2	C_1/C_2
								(ppmv) normalized to nitrogen+argon								
14A-15e-t1	14	A	15	E	101	1	-	500	125,100	nd	nd	159,700	714,600	nd	250	-

Notes: nd = not detected. Approximate detection limits are about 15 ppmv for methane, 30 ppmv for ethane, 50 ppmv for propane, and 20 ppmv for hydrogen sulfide.

Table 8. List of microbiological samples taken for Site NGHP-01-14.—Continued

Core, section	Sample reference					Comments
	Sample code	Top (cm)	Bottom (cm)	Depth (mbsf)	Volume (cc)	
NGHP-01-14A						
1H-3	CEL	83	88	3.83	5	
2H-5	CEL	95	100	11.45	5	
3H-5	CEL	95	100	20.95	5	
4H-5	CEL	95	100	30.45	5	
5H-5	CEL	95	100	39.95	5	
6H-5	CEL	73	78	49.23	5	
7H-5	CEL	85	90	58.73	5	
8H-5	CEL	85	90	67.12	5	
11X-3	CEL	120	125	77.06	5	
12X-5	CEL	85	90	88.6	5	
13X-5	CEL	85	90	99.05	5	
16X-4	CEL	75	80	107.25	5	
17X-1	CEL	84	94	112.44	125	Whole round taken for HS sampling
18X-2	CEL	41	46	122.61	5	
19X-4	CEL	42	47	135.72	5	
20X-4	CEL	37	42	144.26	5	
21X-3	CEL	75	80	153.75	5	
22X-2	CEL	75	80	161.85	5	
23X-3	CEL	75	80	172.95	5	
1H-3	JAN	93	98	3.93	187	
2H-5	JAN	105	110	11.55	187	
3H-5	JAN	105	110	21.05	187	IR anomaly
4H-5	JAN	105	110	30.55	187	IR anomaly
5H-5	JAN	105	110	40.05	187	IR anomaly
6H-5	JAN	83	88	49.33	187	
7H-5	JAN	95	100	58.83	187	
8H-5	JAN	95	100	67.22	187	
12X-5	JAN	95	100	88.7	187	
13X-5	JAN	95	100	99.15	187	
16X-1	JAN	118	119	103.18	37	
16X-4	JAN	85	90	107.35	187	
18X-2	JAN	51	56	122.71	187	
19X-4	JAN	52	57	135.82	187	
20X-4	JAN	47	52	144.36	187	
21X-3	JAN	85	90	153.85	187	
22X-2	JAN	85	90	161.95	187	
23X-3	JAN	85	90	173.05	187	
1H-3	JUD	108	118	4.08	374	
2H-3	JUD	120	130	8.7	374	
2H-5	JUD	120	130	11.7	374	
3H-3	JUD	120	130	18.2	374	
3H-5	JUD	120	130	21.2	374	
4H-3	JUD	120	130	27.7	374	
4H-5	JUD	120	130	30.7	374	
5H-3	JUD	120	130	37.2	374	
5H-5	JUD	120	130	40.2	374	
6H-3	JUD	110	120	46.6	374	
6H-5	JUD	98	108	49.48	374	
7H-3	JUD	105	115	55.98	374	
7H-5	JUD	110	120	58.98	374	
8H-3	JUD	107	117	64.77	374	
8H-5	JUD	110	120	67.37	374	
11X-2	JUD	93	103	75.43	374	
12X-3	JUD	75	85	85.85	374	
12X-5	JUD	110	120	88.85	374	
13X-3	JUD	110	120	96.3	374	
13X-5	JUD	110	120	99.3	374	
16X-2	JUD	40	50	103.9	374	
16X-4	JUD	100	110	107.5	374	
18X-2	JUD	66	76	122.86	374	
19X-4	JUD	67	77	135.97	374	

Table 8. List of microbiological samples taken for Site NGHP-01-14.—Continued

Core, section	Sample reference					Comments
	Sample code	Top (cm)	Bottom (cm)	Depth (mbsf)	Volume (cc)	
NGHP-01-14A—Continued						
20X-4	JUD	62	72	144.51	374	
21X-3	JUD	100	110	154	374	
22X-2	JUD	100	110	162.1	374	
23X-3	JUD	100	110	173.2	374	
16X-1	MAF	100	110	103	374	
16X-1	MAG	110	118	103.1	299	
16X-1	MAR	90	100	102.9	374	
19X-3	MBF	125	135	135.05	374	
19X-3	MBG	135	145	135.15	374	
19X-3	MBR	115	125	134.95	374	
1H-3	SPH	88	93	3.88	187	
2H-5	SPH	100	105	11.5	187	
3H-5	SPH	100	105	21	187	
4H-5	SPH	100	105	30.5	187	
5H-5	SPH	100	105	40	187	
6H-5	SPH	78	83	49.28	187	
7H-5	SPH	90	95	58.78	187	
8H-5	SPH	90	95	67.17	187	
11X-3	SPH	125	130	77.11	187	
12X-5	SPH	90	95	88.65	187	
13X-5	SPH	90	95	99.1	187	
16X-4	SPH	80	85	107.3	187	
17X-1	SPH	94	99	112.54	187	
18X-2	SPH	46	51	122.66	187	
19X-4	SPH	47	52	135.77	187	
20X-4	SPH	42	47	144.31	187	
21X-3	SPH	80	85	153.8	187	
22X-2	SPH	80	85	161.9	187	
23X-3	SPH	80	85	173	187	

Physical Property Trends

Overall physical properties vary in expected patterns downhole except that subtle changes occur at the APC and XCB coring boundary, and at the BSR showing “lobes” or offsets in properties above, between, and below these depths (figs. 20 and 21). Data sets that show behavioral changes at these depths include: water content, porosity, bulk density, shear strength, electrical resistivity (MSCL), and magnetic susceptibility. However, because distinct trends were not discernable across various property types, the hole was classified as one physical-property unit.

Index Properties

Water content and porosity decrease downhole in primarily nannofossil bearing clay, nannofossil rich clay, and clay (see “Lithostratigraphy”). Water content (related to solids) varies from a high of 115 percent to a low of 29 percent (table 12) and rapidly decreases from the seafloor to a subbottom depth of 25 mbsf. Porosity varies from 75 percent to 44 percent downhole. This overall trend is similar to wire-line logging data that begins at about 67 mbsf.

Bulk density data from MAD and MSCL measurements and wire-line logging are in close agreement downhole (fig. 20). Grain density varies from 2.51 to 2.80 g/cm^3 with an average value of 2.73 g/cm^3. Some of this variation is a result of performing mass measurements at sea on small sediment samples after the water has been removed by drying. The pycnometers produce more variable volume measurements when used with smaller samples. This result is most pronounced in the upper sections of the hole where water contents are highest. Grain densities are lower in the upper part of the hole, possibly the result of increased marine organic content. The pycnometers often had difficulty measuring volume of samples from the top of the hole.

Strength

Shear strength increased linearly with depth to just above the boundary between APC and XCB cores (tables 13, 14, and 15; fig. 20). Below that depth, slightly more variation exists, illustrating the effect of disturbance caused by rotary coring on sediment. Although testing was to be restricted to intact biscuits, it was occasionally difficult to differentiate between biscuits and adjacent disturbed sediment. A zone of decreased strength exists between the APC–XCB core boundary and the BSR.

The measured shear strengths were normalized to the effective vertical stress (σ'_v) (fig. 22) to provide qualitative information on the stress history of the sediment. The strength/effective vertical stress ranges from approximately

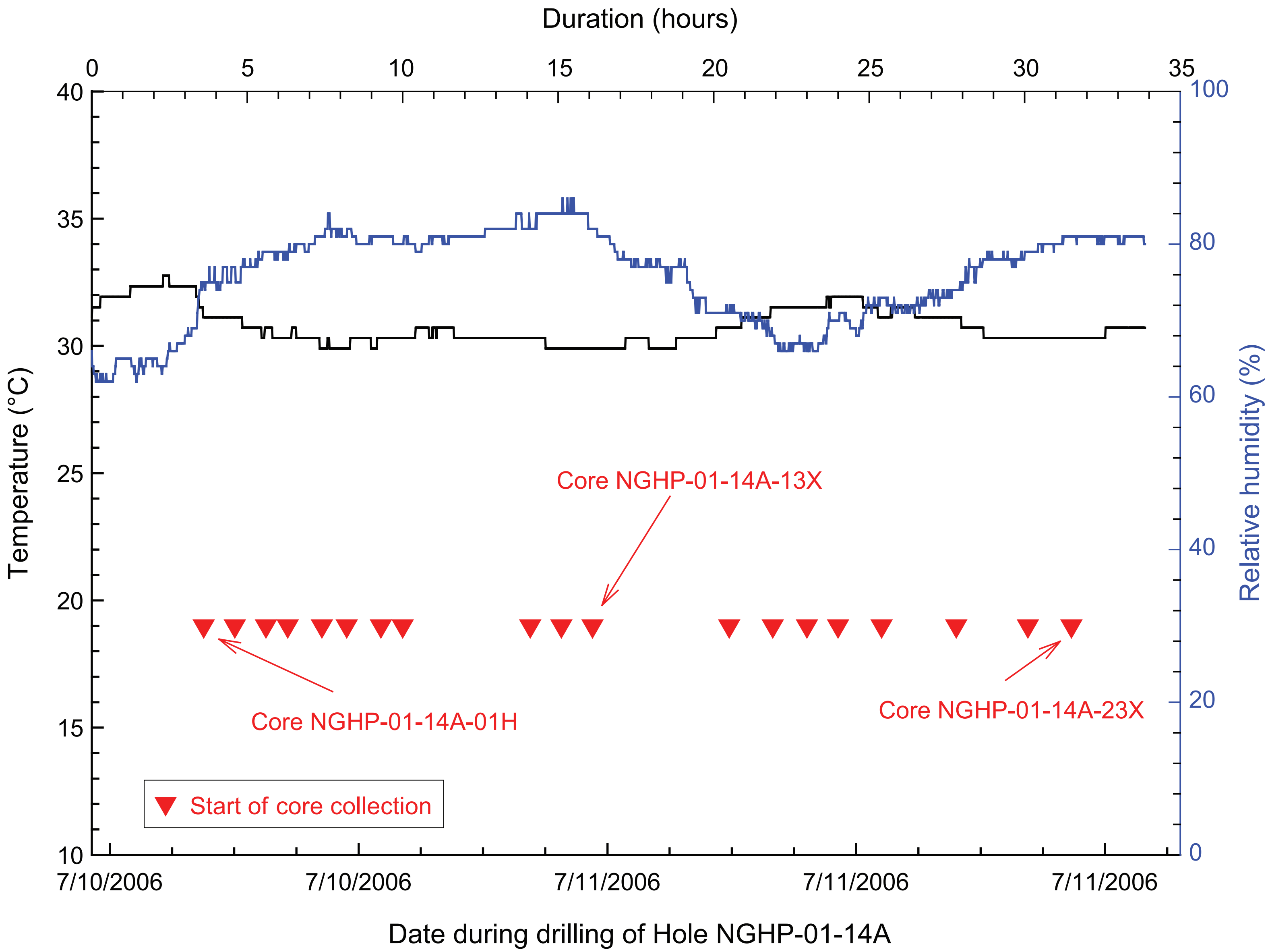

Figure 16. Catwalk temperature and humidity during drilling operations at Site NGHP-01-14.

Table 9. List of infrared image files collected on cores on the catwalk from Hole NGHP-01-14A.

Core	Imaging length (cm)	First run	Date	Start time	Temperature (start/end) (˚C)	File ID	Screen image saved	Comments*
1H								No image, IR track down
2H								No image, IR track down
3H	950	x	7/10	16:37	30.7/30.7	NGHP-14-B-3	Yes	15–30 °C
4H	960	x	7/10	17:19	30.3/30.3	NGHP-14-B-4	Yes	15–30 °C
5H	960	x	7/10	18:24	30.3/30.3	NGHP-14-B-5	Yes	15–30 °C
6H	970	x	7/10	19:09	29.9/29.9	NGHP-14-B-6	Yes	15–30 °C
7H	970	x	7/10	20:16	30.3/30.3	NGHP-14-B-7	Yes	15–30 °C
8H	925	x	7/10	21:02	30.3/30.3	NGHP-14-B-8	Yes	15–30 °C
11H	570	x	7/11	1:07	30.3/30.3	NGHP-14-B-11	Yes	15–30 °C
12X	760	x	7/11	2:05	30.3/30.3	NGHP-14-B-12	Yes	15–30 °C
13X	870	x	7/11	3:07	29.9/29.9	NGHP-14-B-13	Yes	15–30 °C
16X	940	x	7/11	7:53	30.3/30.3	NGHP-14-B-16	Yes	15–30 °C
17X	230	x	7/11	8:54	31.1/31.1	NGHP-14-B-17	Yes	15–30 °C
18X	350	x	7/11	10:10	31.5/31.5	NGHP-14-B-18	Yes	15–30 °C
19X	950	x	7/11	11:23	32.0/32.0	NGHP-14-B-19	Yes	15–30 °C
20X	890	x	7/11	12:21	31.5/31.5	NGHP-14-B-20	Yes	15–30 °C
21X	870	x	7/11	14:45	31.1/31.1	NGHP-14-B-21	Yes	15–30 °C
22X	400	x	7/11	17:04	30.7/30.7	NGHP-14-B-22	Yes	15–30 °C
23X	810	x	7/11	18:29	30.3/30.3	NGHP-14-B-23	Yes	15–30 °C

*Temperature range for images displayed during core collection.

Table 10. List of infrared image files collected on core ends from Hole NGHP-01-14A.

Core	Section	Top	Date	Time	Image #	Comments
2	3	x	7/10	15:39	G0710-03	IMG file
2	3	x	7/10	15:39	G0710-04	Core end, BMP
3	4	x	7/10	16:49	G0710-05	IMG file
3	4	x	7/10	16:49	G0710-06	Core end, BMP
4	3	x	7/10	17:41	G0710-07	IMG file
4	3	x	7/10	17:41	G0710-08	Core end, BMP
5	4	x	7/10	18:39	G0710-09	IMG file
5	4	x	7/10	18:39	G0710-10	Core end, BMP
6	3	x	7/10	19:30	G0710-11	IMG file
6	3	x	7/10	19:30	G0710-12	IMG file
7	3	x	7/10	20:44	G0710-13	Core end, BMP
7	3	x	7/10	20:44	G0710-14	IMG file
8	?	x	7/10	21:25	G0710-15	Core end, BMP
8	?	x	7/10	21:25	G0710-16	IMG file
11	3	x	7/11	1:18	G0711-01	Core end, BMP
11	3	x	7/11	1:18	G0711-02	IMG file
12	2	x	7/11	2:22	G0711-03	Core end, BMP
12	2	x	7/11	2:22	G0711-04	IMG file
13	3	x	7/11	3:20	G0711-05	Core end, BMP
13	3	x	7/11	3:20	G0711-06	IMG file
16	3	x	7/11	7:40	G0711-07	IMG file
16	3	x	7/11	7:40	G0711-08	Core end, BMP
18	2	x	7/11	10:08	G0711-09	IMG file
18	2	x	7/11	10:08	G0711-10	Core end, BMP
19	3	x	7/11	11:38	G0711-11	IMG file
19	3	x	7/11	11:38	G0711-12	Core end, BMP
20	2	x	7/11	12:39	G0711-13	IMG file
20	2	x	7/11	12:39	G0711-14	Core end, BMP
21	3	x	7/11	14:57	G0711-15	IMG file
21	3	x	7/11	14:57	G0711-16	Core end, BMP
22	3	x	7/11	17:13	G0711-17	IMG file
22	3	x	7/11	17:13	G0711-18	Core end, BMP
23	3	x	7/11	18:36	G0711-19	IMG file
23	3	x	7/11	18:36	G0711-20	Core end, BMP

Table 11. List of temperature probe data from Hole NGHP-01-14A.

Core	Section	Top	Bottom	Date	In time	Out time	Temperature probe #	Comments
1H								
2H	last		X	10-Jul	15:36	12:28	1, 2, 3, 4,	
3H	last		X	10-Jul	16:37	16:51	1, 2, 3, 4,	
4H	last		X	10-Jul	17:19	17:41	1, 2, 3, 4,	
5H	last		X	10-Jul	18:34	18:54	1, 2, 3, 4,	
6H	7	X	X	10-Jul	19:22	19:41	1, 2, 3, 4,	Next to IR image
7H	last		X	10-Jul	22:24	20:44	1, 2, 3, 4,	
8H	last		X	10-Jul	21:02	21:28	1, 2, 3, 4,	
11X	last		X	11-Jul	1:07	1:18	1, 2, 3, 4,	
12X	last		X	11-Jul	2:05	2:21	1, 2, 3, 4,	
13X	last		X	11-Jul	3:07	3:20	1, 2, 3, 4,	
16X	last		X	11-Jul	7:35	8:00	1, 2, 3, 4,	
17X	last		X	11-Jul	8:54	9:00	1, 2, 3, 4,	
18X	last		X	11-Jul	10:00	10:07	1, 2, 3, 4,	
19X	last		X	11-Jul	11:25	11:37	1, 2, 3, 4,	
20X	last		X	11-Jul	12:28	12:46	1, 2, 3, 4,	
21X	last		X	11-Jul	14:49	14:59	1, 2, 3, 4,	
22X	last		X	11-Jul	17:09	18:16	1, 2, 3, 4,	
23X	last		X	11-Jul	18:36	18:38	1, 2, 3, 4,	

1.55 at the top of the hole (with most values below 0.4) to an average of about 0.075 near the bottom of the hole. These values are in overall agreement with a number of other normally consolidated clays (Holtz and Kovacs, 1981), although the values below 0.1 are probably an artifact of the more deeply buried sediment from this hole compared to most engineering-type projects from which the published comparison samples were taken. Hunt (1984) states that the strength/effective vertical stress ratio typically is between 0.4 and 0.16. The wide scatter in the results at the top of the hole reflects the dependency of this ratio on the stress path as well as the test method (Bjerrum, 1972; Ladd and others, 1977). Because almost all of the values are below 0.4, the implication is that these sediments have not experienced a vertical effective stress greater than what is now being applied *in situ*. They have not been overconsolidated by erosional or other geologic processes.

Peak (Sv) and remolded (Srem) vane shear strengths clearly increase with subbottom depth. The sensitivity (St), which equals Sv/Srem, has a fairly broad distribution, ranging from about 1.6 to 4.0 (fig. 23) and is independent of depth. Sensitivity values represent the amount of strength loss after remolding and in extreme examples can reach values of 500 (Lambe and Whitman,1969). This sediment has low sensitivity (Holtz and Kovacs, 1981). High values of sensitivity are indicative of good quality core recovery because the sediment has not been highly disturbed.

Electrical Resistivity

Wire-line logging performed in Hole NGHP-01-14A after coring indicates that resistivity values are fairly low and uniform downhole in overall agreement with the MSCL data. Unlike other holes, for example, Hole NGHP-01-10B, these low resistivity values do not reflect significant zones of gas hydrate in Hole NGHP-01-14A. Resistivity determined using both MSCL and the Wenner array on split cores (table 16) increase near 22.5 mbsf, the approximate depth of the SMI. A possible explanation for this agreement is that methane is produced below the SMI and this gas expands upon core recovery disrupting the sediment structure.

The resistivity measurements from the Wenner array are offset below both the MSCL and wire-line logging values (fig. 21). This may in part be due to Wenner measurements being conducted on intact core material, rather than a wider portion of core that may contain voids or small expansion cracks. Lower MSCL values are more representative of undisturbed sediment as they are less impacted by the presence of such micro voids caused by gas expansion.

The apparent formation factor is the ratio of the resistivity of a saturated sediment to the resistivity of the pore fluid and provides an indication of the relationships between sediment structure, void space, tortuosity, and other factors, and the ability of fluid to flow through the formation. Because pore water salinity typically varies a small amount from that of seawater in the recovered sediment (see "Inorganic geochemistry"), we have normalized the measured Wenner resistivity values by that of seawater (approximately 0.2 Ω/m) (table 16). Values range from about 1.6 at the top of the core to 4.5 at the bottom (fig. 24). Other equations and methods exist for calculating formation factor; however, they require the use of empirical constants that have not yet been determined for these particular sediments.

P-wave Velocity

P-wave velocity (V_p) measured with the MSCL increased slightly from 1.48 km/s in the top of the hole to 1.55 km/s at a subbottom depth of 24.6 m (fig. 21), which represents the depth where gas and voids present in the sediment prevented further

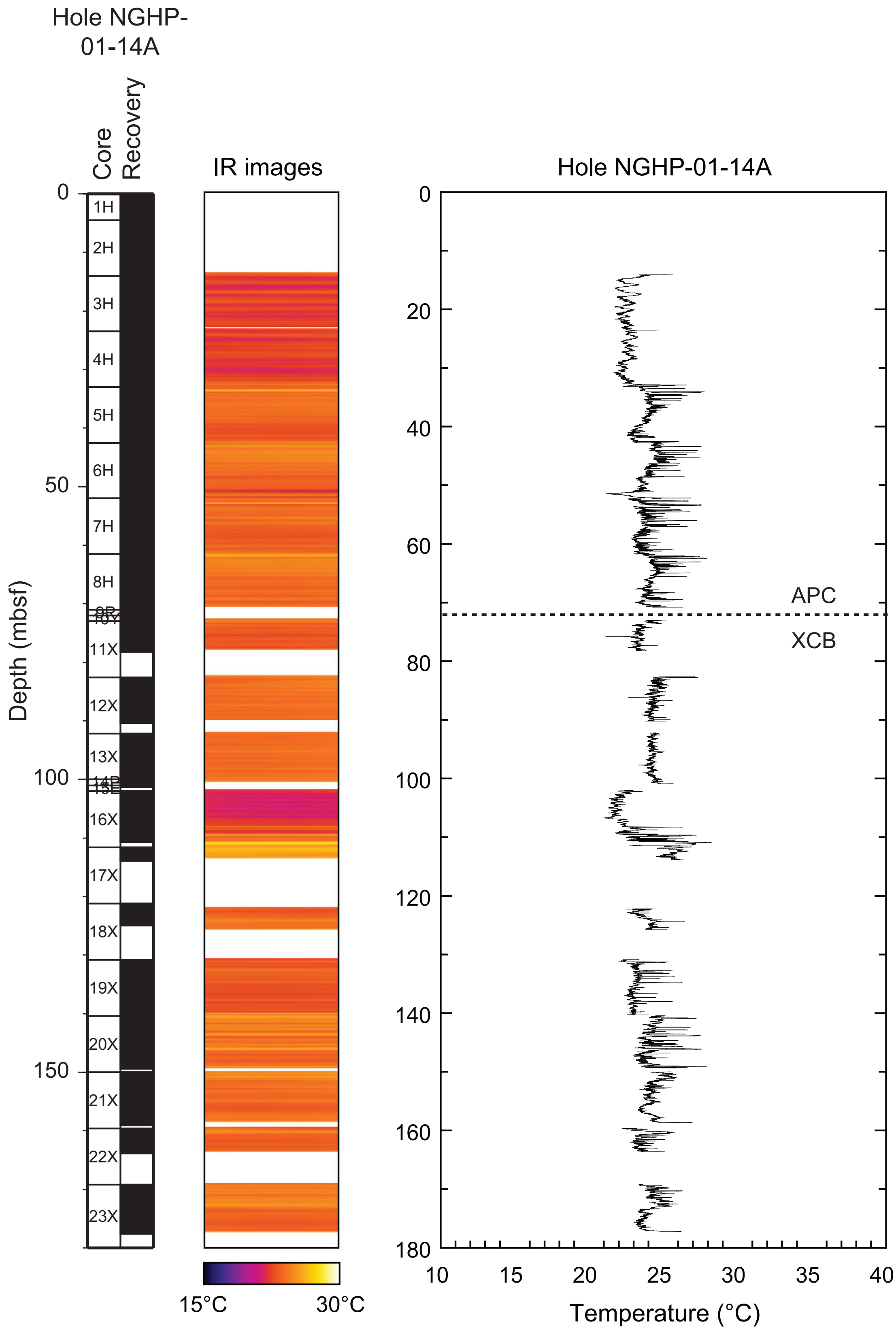

Figure 17. Infrared imaging and the derived downhole temperature profile for Hole NGHP-01-14A.

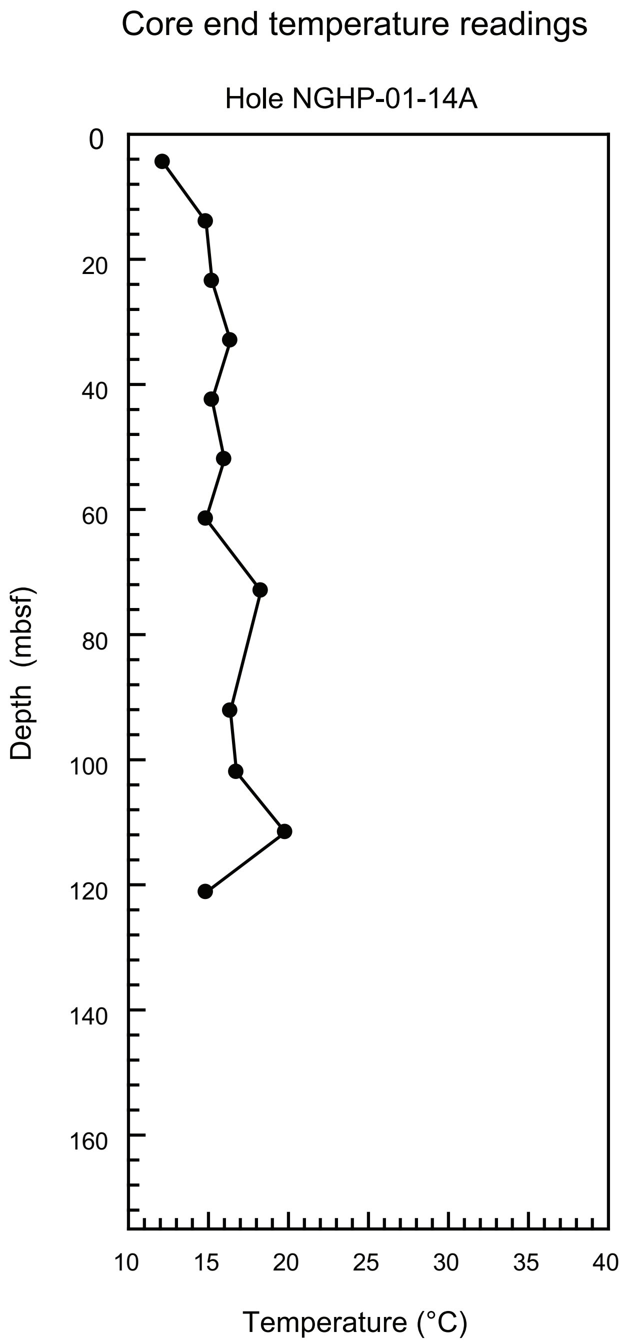

Figure 18. Core-end probe temperature measurement data for Hole NGHP-01-14A.

valid measurements from beings logged. The contact V_P values of 1.47 to 1.54 km/s (table 17) are in agreement with the MSCL values and could not be determined below 22.9 mbsf. Both the MSCL and the contact electrical resistivity values drop out at approximately the depth of the SMI (~22.5 mbsf) determined from interstitial water (IW) and gas geochemistry analyses (see "Inorganic Geochemistry" and "Organic Geochemistry"). Methane, which is typically produced below the SMI, may come out of solution if present in a high enough concentration and attenuate acoustic signals.

Magnetic Susceptibility (MS)

Wide excursions exist in the magnetic susceptibility data indicating that primary and secondary magnetic minerals are present in alternating non-uniform high and low frequency layers (with respect to depth) (fig. 21; see "Lithostratigraphy"). MS decreases uniformly to about 10 mbsf, then has multiple high-amplitude, high-frequency signals to 30 mbsf, and moderate amplitudes to the APC–XCB coring boundary. Beneath the APC–XCB coring boundary the signal becomes less variable then increases to the highest values recorded in the hole, just above the BSR. Amplitude becomes more moderate below the BSR.

Thermal Conductivity

Thermal conductivities vary between 0.694 and 1.033 W/(m×K) and increase slightly with subbottom depth, except between 24 and 43 mbsf (table 18 and fig. 21). Such values are well within the range of marine sediments (for example, Novosel and others, 2007), although they are all lower than values determined by Davis and others (1990) for sediment from Cascadia and the Nankai Trough.

Downhole Temperature Measurements

A number of different tools are available for determining downhole sediment temperature (see "Physical Properties" in "Methods"). Although six attempts were made, only five provided usable *in situ* temperature data at Site NGHP-01-14, and two of those measurements are only of fair quality. Seafloor temperature intercept was determined to be 7.9 ± 0.3 °C and the geothermal gradient was determined to be 38 ± 2 °C per km (fig. 25 and table 19. The base of gas-hydrate stability (BGHS) zone is predicted at 150 mbsf assuming pure methane and porewater salinity of 35 ppt (Sloan, 1998). This is the only site for which the BGHS predicted by the thermal gradient is significantly different from the observed BSR depth (109 mbsf; shipboard calculated seafloor temperature 7.9 °C, geothermal gradient 37 °C per km).

Pressure Coring

The main objectives of pressure coring during NGHP Expedition 01 were to quantify natural gas composition and concentration in sediments and to determine the nature and distribution of gas hydrate and free gas within the sediment matrix. Secondary objectives were to obtain measurements of physical properties on gas-hydrate-bearing sediments under *in-situ* conditions, which can be used to help interpret regional seismic data, and obtain samples under full pressure for shore-based studies. To achieve these objectives, we conducted depressurization experiments and captured resultant gas to calculate gas-hydrate quantity, made nondestructive measurements (X-ray imaging, *P*-wave velocity, gamma density) at *in situ* pressures

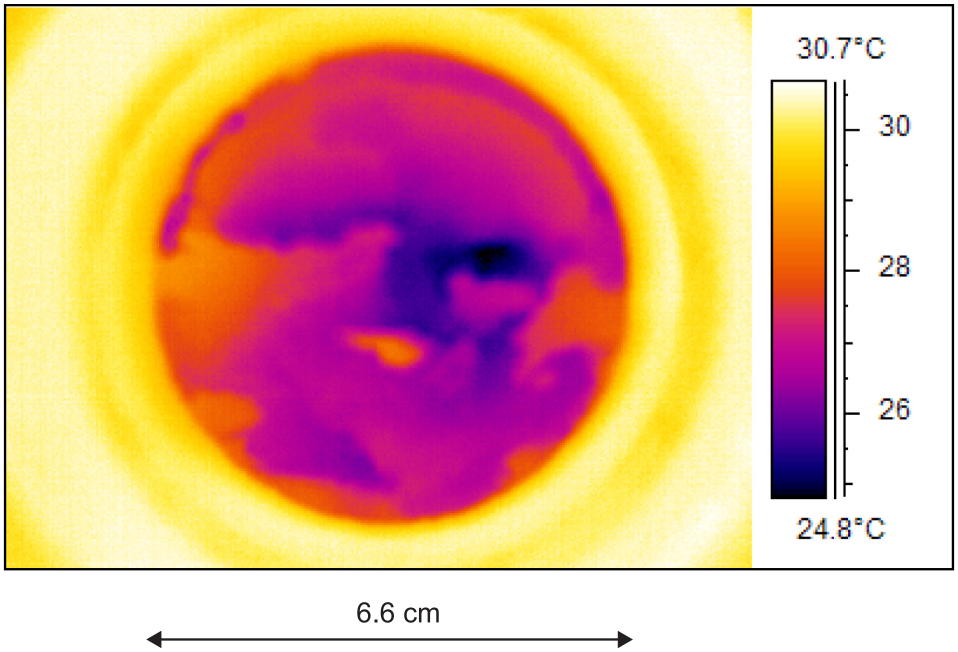

Figure 19. Core-end infrared image from Hole NGHP-01-14A, with the corresponding reference temperature scale. Note small cold spot near the middle of the core.

and during depressurization to examine gas-hydrate habit within sediments, and archived gas-hydrate-bearing sediments at in situ pressures for more comprehensive investigations on shore.

The BSR at Site NGHP-01-14, located in the KG Basin was a strong reflector with an estimated depth of 100 mbsf. This site was expected to contain gas hydrate, as it was located above a potential focusing mechanism for gas (see “Background and Objectives”). There were no LWD data from this site.

Pressure Core Operations and Measurements

Pressure coring tools were deployed four times in Hole NGHP-01-14A (table 20); two PCS cores, one FPC core, and one HRC core. Figures 26 and 27 show the pressure and temperature history of the cores during deployment, coring, recovery, and chilling (in the ice shuck) of the pressure coring tools. Figures 28 and 29 show the measurements made on the single successful core at full pressure and during depressurization. Figure 30 shows the gas and fluid released from the successful core.

Core NGHP-01-14B-15E (102 mbsf), collected near the estimated depth of the BSR (109 mbsf), retrieved a partial core (0.32 m) at pressure (table 20). Core NGHP-01-14A-15E was transferred to the MSCL–P and X-ray images, gamma density and *P*-wave velocity measurements were collected (fig. 28). The measurements showed no evidence of gas-hydrate structures. The core was depressurized in the MSCL-P, releasing 1.04 liters of methane, which is equivalent to methane hydrate at 0.7 percent of pore volume or 2.4 mL of methane hydrate (table 21). The core also released more than usual amounts of nitrogen (see “Organic Geochemistry”). A final MSCL-P scan was collected at atmospheric pressure which showed a highly expanded core (fig. 29). One chlorinity measurement was made on this core (538.1 mM, 0–19 cm); even after sulfate correction (~25 percent seawater in the sample) this sample showed no freshening in comparison with samples from similar depths

Gas-Hydrate Concentration, Nature, and Distribution from Pressure Coring

Only one of the four pressure cores at Site NGHP-01-14 was recovered at sufficient pressures to accurately assess the total concentration of methane and hence the predicted amounts of gas hydrate. The calculated methane concentration for this core is shown in figure 31 in relation to the phase boundaries for Structure I methane hydrate. (The pressure core and the void gases collected at this site contained less than 50 ppm ethane, confirming the suitability of Structure I methane hydrate for stability calculations; see “Organic Geochemistry”). Core NGHP-01-14A-15E provides evidence for small amounts of gas hydrate near the estimated depth of the BSR, predicted to be significantly above the base of gas-hydrate stability (calculated at 121 mbsf; fig. 31).

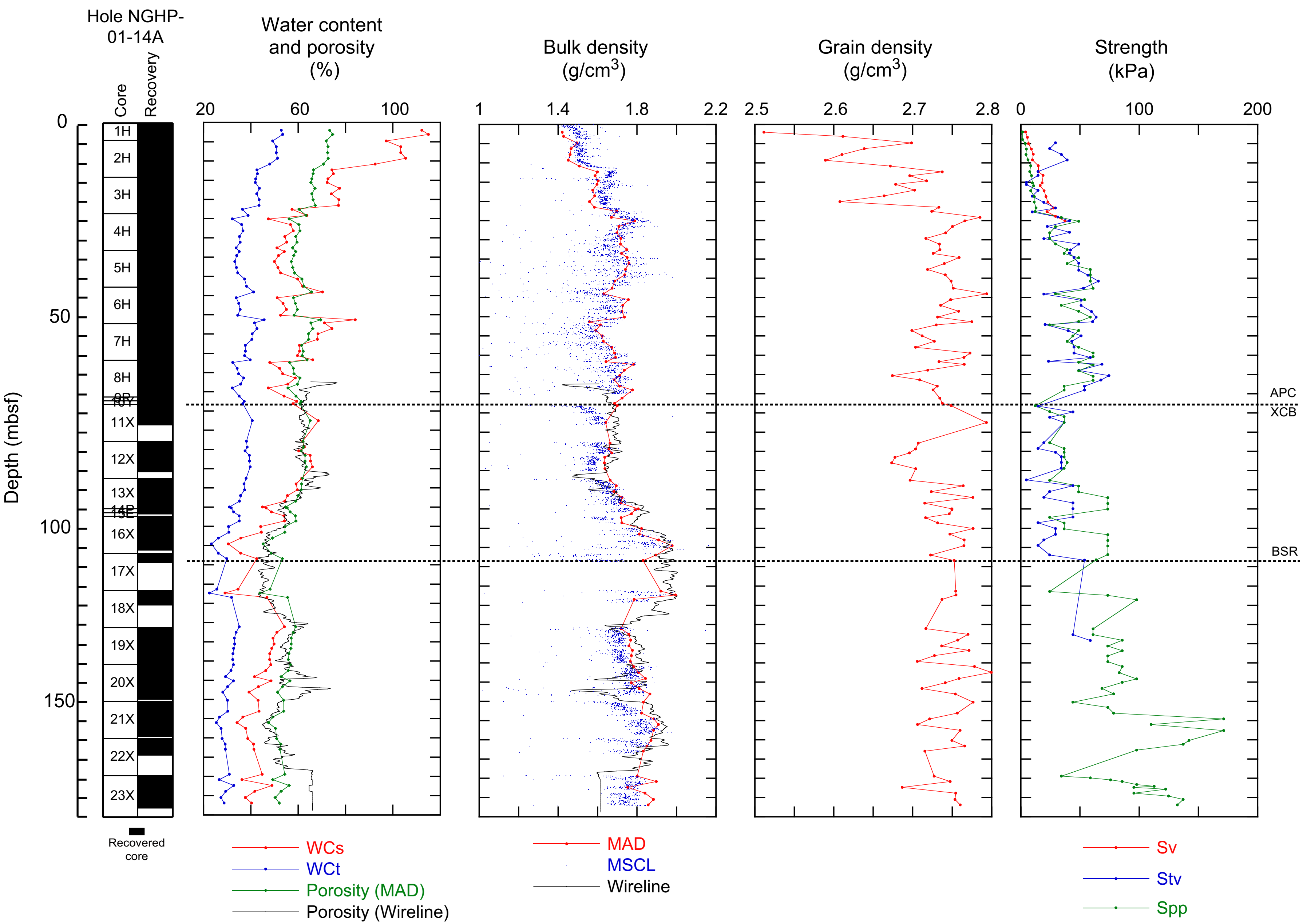

Figure 20. Profiles of core recovery, index, and strength properties for Hole NGHP-01-14A.

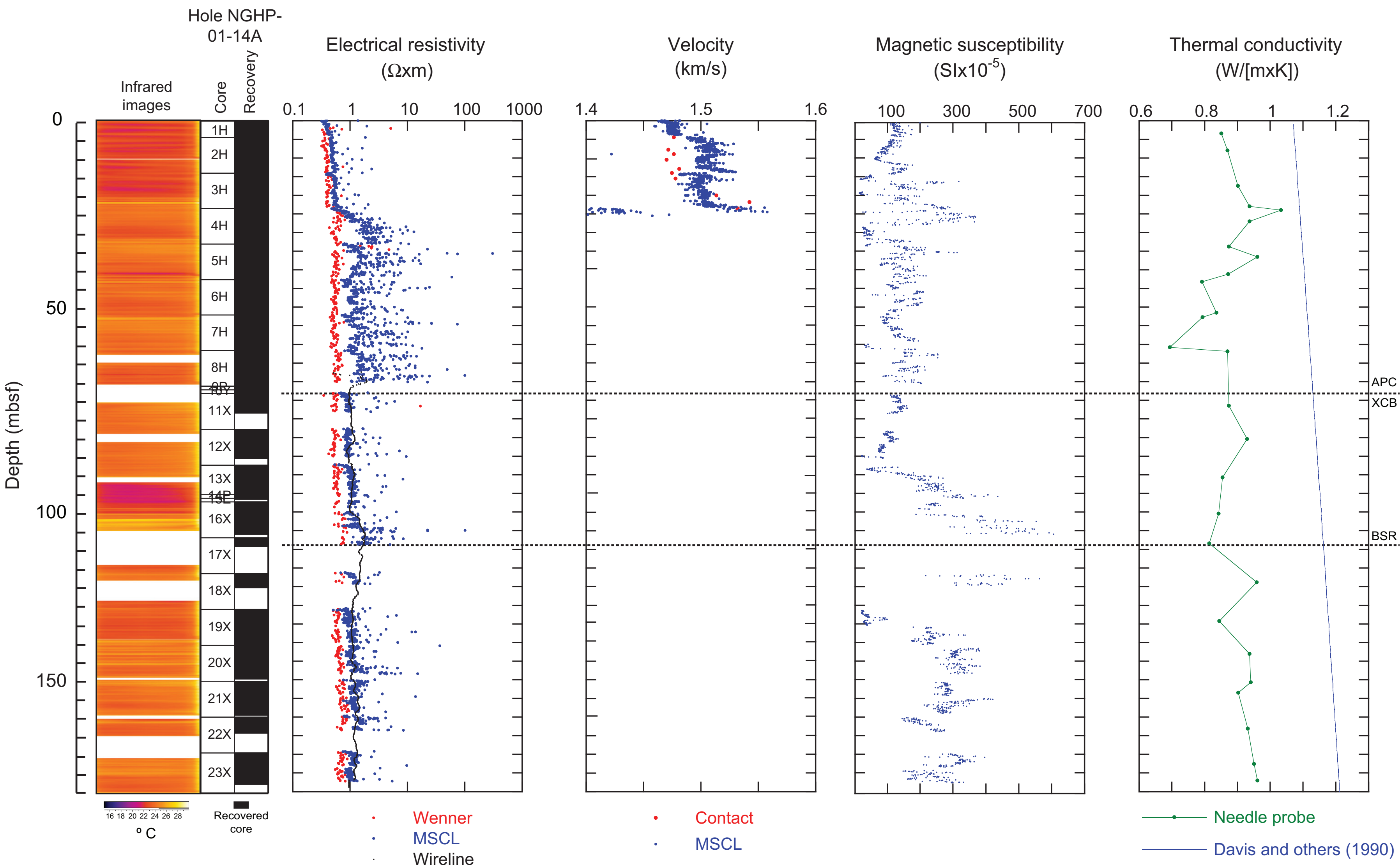

Figure 21. Profiles of infrared images, core recovery, electrical resistivity, acoustic *P*-wave velocity, magnetic susceptibility, and thermal conductivity for Hole NGHP-01-14A.

Table 12. Moisture and density (MAD) physical properties for Hole NGHP-01-14A.

Core, section	Sample code	Depth increment, from (cm)	Depth, increment, to (cm)	Depth (mbsf)	WCt (%)	WCs (%)	Grain density (g/cm^3)	Bulk density (g/cm^3)	Dry bulk density (g/cm^3)	Porosity (%)	Void ratio	Unit weight (kN/m^3)
NGHP-01-14A												
1H-2	MAD	56	58	2.06	52.90	112.31	2.51	1.42	0.67	73.34	2.75	13.94
1H-3	MAD	14	16	3.14	53.49	115.02	2.61	1.43	0.66	74.55	2.93	14.01
2H-1	MAD	34	36	4.84	49.28	97.16	2.70	1.50	0.76	71.89	2.56	14.67
2H-2	MAD	34	36	6.34	50.83	103.37	2.64	1.47	0.72	72.68	2.66	14.38
2H-3	MAD	34	36	7.84	50.83	103.37	2.61	1.46	0.72	72.47	2.63	14.33
2H-4	MAD	34	36	9.34	51.32	105.42	2.59	1.45	0.71	72.70	2.66	14.24
2H-5	MAD	34	36	10.84	48.07	92.55	2.67	1.51	0.78	70.69	2.41	14.79
2H-6	MAD	34	36	12.34	42.61	74.26	2.74	1.60	0.92	66.47	1.98	15.68
2H-7	MAD	34	36	13.34	42.83	74.91	2.70	1.59	0.91	66.33	1.97	15.57
3H-1	MAD	68	70	14.68	42.08	72.64	2.72	1.60	0.93	65.82	1.93	15.73
3H-2	MAD	10	12	15.60	41.96	72.31	2.68	1.60	0.93	65.38	1.89	15.67
3H-3	MAD	10	12	17.10	43.66	77.48	2.70	1.58	0.89	67.13	2.04	15.46
3H-4	MAD	10	12	18.60	42.54	74.02	2.66	1.59	0.91	65.79	1.92	15.55
3H-5	MAD	10	12	20.10	43.59	77.28	2.61	1.56	0.88	66.28	1.97	15.29
3H-6	MAD	8	10	21.58	43.51	77.01	2.73	1.58	0.90	67.24	2.05	15.54
3H-7	MAD	10	12	22.60	36.49	57.46	2.72	1.70	1.08	60.42	1.53	16.65
4H-1	MAD	69	71	24.19	38.92	63.72	2.79	1.67	1.02	63.38	1.73	16.38
4H-2	MAD	9	11	25.09	32.18	47.45	2.77	1.79	1.21	56.15	1.28	17.54
4H-3	MAD	6	8	26.56	36.21	56.77	2.75	1.71	1.09	60.36	1.52	16.76
4H-4	MAD	19	21	28.19	36.70	57.97	2.74	1.70	1.08	60.79	1.55	16.66
4H-5	MAD	18	20	29.68	35.23	54.39	2.72	1.72	1.11	59.04	1.44	16.85
4H-6	MAD	14	16	31.14	35.57	55.21	2.73	1.72	1.11	59.55	1.47	16.83
4H-7	MAD	9	11	32.59	33.81	51.08	2.73	1.75	1.16	57.67	1.36	17.15
5H-1	MAD	56	58	33.56	35.14	54.19	2.73	1.72	1.12	59.03	1.44	16.89
5H-2	MAD	12	14	34.62	34.08	51.69	2.76	1.75	1.15	58.18	1.39	17.17
5H-3	MAD	17	19	36.17	33.31	49.96	2.74	1.76	1.17	57.18	1.34	17.26
5H-4	MAD	23	25	37.73	33.98	51.47	2.72	1.74	1.15	57.71	1.36	17.08
5H-5	MAD	13	15	39.13	34.48	52.62	2.74	1.74	1.14	58.45	1.41	17.05
5H-6	MAD	21	23	40.71	37.43	59.81	2.75	1.69	1.06	61.59	1.60	16.55
6H-1	MAD	12	14	42.62	38.25	61.94	2.75	1.67	1.03	62.44	1.66	16.41
6H-2	MAD	6	8	44.06	41.30	70.35	2.79	1.63	0.96	65.72	1.92	16.00
6H-3	MAD	9	11	45.59	33.87	51.21	2.75	1.76	1.16	58.03	1.38	17.23
6H-4	MAD	5	7	47.05	34.93	53.67	2.74	1.73	1.12	58.88	1.43	16.95
6H-5	MAD	9	11	48.59	35.50	55.05	2.76	1.72	1.11	59.69	1.48	16.91
6H-6	MAD	24	26	50.12	34.46	52.57	2.73	1.74	1.14	58.34	1.40	17.03
6H-7	MAD	12	14	51.32	45.69	84.13	2.78	1.56	0.85	69.50	2.28	15.29
7H-1	MAD	13	15	52.13	41.56	71.12	2.73	1.61	0.94	65.44	1.89	15.83
7H-2	MAD	9	11	53.59	42.62	74.29	2.70	1.59	0.91	66.17	1.96	15.61
7H-3	MAD	5	7	54.98	40.62	68.41	2.71	1.62	0.96	64.38	1.81	15.93
7H-4	MAD	4	6	56.42	40.55	68.21	2.73	1.63	0.97	64.47	1.81	15.99
7H-5	MAD	6	8	57.94	37.72	60.56	2.70	1.67	1.04	61.50	1.60	16.39
7H-6	MAD	7	9	59.45	37.76	60.68	2.77	1.69	1.05	62.14	1.64	16.54
7H-7	MAD	28	30	60.60	37.41	59.77	2.77	1.69	1.06	61.71	1.61	16.59
8H-1	MAD	20	22	61.70	39.81	66.13	2.73	1.64	0.99	63.81	1.76	16.12
8H-2	MAD	22	24	62.42	32.44	48.03	2.77	1.78	1.20	56.43	1.30	17.49
8H-3	MAD	22	24	63.92	34.26	52.12	2.72	1.74	1.14	58.02	1.38	17.03
8H-4	MAD	16	18	65.33	34.85	53.50	2.67	1.71	1.12	58.24	1.39	16.80
8H-5	MAD	17	19	66.44	37.01	58.77	2.71	1.68	1.06	60.82	1.55	16.52
8H-6	MAD	26	28	68.03	35.78	55.71	2.73	1.71	1.10	59.74	1.48	16.79
8H-7	MAD	26	28	69.05	32.16	47.40	2.73	1.78	1.21	55.75	1.26	17.43
9P-1	MAD	16	18	71.16	35.11	54.11	2.73	1.72	1.12	59.07	1.44	16.92
10Y-1	MAD	53	55	72.53	37.26	59.40	2.74	1.69	1.06	61.33	1.59	16.55
11X-1	MAD	15	17	73.15	36.68	57.92	2.75	1.70	1.08	60.83	1.55	16.67

Table 12. Moisture and density (MAD) physical properties for Hole NGHP-01-14A.—Continued

Core, section	Sample code	Depth increment, from (cm)	Depth, increment, to (cm)	Depth (mbsf)	WCt (%)	WCs (%)	Grain density (g/cm³)	Bulk density (g/cm³)	Dry bulk density (g/cm³)	Porosity (%)	Void ratio	Unit weight (kN/m³)
NGHP-01-14A—Continued												
11X-4	MAD	15	17	77.51	40.68	68.57	2.79	1.64	0.97	65.14	1.87	16.10
12X-1	MAD	30	32	82.90	38.23	61.88	2.71	1.66	1.03	62.03	1.63	16.32
12X-2	MAD	30	32	84.40	38.53	62.69	2.70	1.66	1.02	62.31	1.65	16.26
12X-3	MAD	30	32	85.40	37.60	60.27	2.70	1.67	1.04	61.31	1.58	16.39
12X-4	MAD	30	32	86.55	39.44	65.12	2.68	1.64	0.99	62.97	1.70	16.05
12X-5	MAD	30	32	88.05	39.48	65.23	2.67	1.64	0.99	62.98	1.70	16.04
12X-6	MAD	30	32	89.55	39.76	66.01	2.70	1.64	0.99	63.52	1.74	16.06
13X-1	MAD	30	32	92.50	38.10	61.55	2.70	1.66	1.03	61.82	1.62	16.31
13X-2	MAD	30	32	94.00	37.18	59.18	2.76	1.70	1.06	61.47	1.60	16.62
13X-3	MAD	30	32	95.50	37.37	59.66	2.72	1.68	1.05	61.31	1.58	16.50
13X-4	MAD	30	32	97.00	35.70	55.52	2.78	1.72	1.11	60.06	1.50	16.91
13X-5	MAD	30	32	98.50	35.23	54.39	2.72	1.72	1.11	59.02	1.44	16.85
13X-6	MAD	30	32	100.00	31.02	44.97	2.75	1.81	1.25	54.67	1.21	17.72
14P-1	MAD	24	26	100.24	31.73	46.48	2.75	1.79	1.22	55.41	1.24	17.56
15E-1	MAD	28	30	101.28	32.76	48.71	2.75	1.77	1.19	56.61	1.30	17.38
16X-1	MAD	30	32	102.30	35.08	54.04	2.72	1.72	1.12	58.88	1.43	16.87
16X-2	MAD	10	12	103.60	35.15	54.20	2.73	1.72	1.12	59.09	1.44	16.90
16X-3	MAD	10	12	105.10	30.63	44.15	2.78	1.82	1.26	54.45	1.20	17.88
16X-4	MAD	4	6	106.54	30.78	44.47	2.75	1.81	1.25	54.37	1.19	17.76
16X-5	MAD	4	6	108.04	26.40	35.87	2.77	1.91	1.41	49.17	0.97	18.73
16X-6	MAD	13	15	109.55	23.42	30.57	2.77	1.98	1.52	45.19	0.82	19.41
17X-1	MAD	42	44	112.02	26.32	35.73	2.72	1.90	1.40	48.69	0.95	18.60
17X-2	MAD	42	44	113.41	29.86	42.57	2.75	1.83	1.28	53.34	1.14	17.96
18X-1	MAD	16	18	121.36	25.73	34.64	2.75	1.92	1.43	48.21	0.93	18.84
18X-2	MAD	16	18	122.36	22.55	29.11	2.75	2.00	1.55	43.89	0.78	19.57
18X-3	MAD	16	18	123.52	31.89	46.83	2.74	1.79	1.22	55.56	1.25	17.52
19X-1	MAD	30	32	131.10	35.16	54.22	2.72	1.72	1.11	58.96	1.44	16.86
19X-2	MAD	30	32	132.60	33.79	51.03	2.77	1.76	1.16	57.96	1.38	17.25
19X-3	MAD	30	32	134.10	33.08	49.42	2.76	1.77	1.18	57.06	1.33	17.35
19X-4	MAD	30	32	135.60	33.26	49.83	2.74	1.76	1.17	57.09	1.33	17.26
19X-5	MAD	30	32	136.77	32.81	48.84	2.77	1.78	1.19	56.90	1.32	17.44
19X-6	MAD	30	32	138.14	32.45	48.05	2.73	1.77	1.20	56.11	1.28	17.38
19X-7	MAD	30	32	139.64	32.42	47.97	2.71	1.77	1.19	55.87	1.27	17.33
20X-2	MAD	9	11	140.98	32.67	48.52	2.78	1.78	1.20	56.80	1.31	17.48
20X-3	MAD	8	10	142.47	31.67	46.35	2.80	1.81	1.24	55.86	1.27	17.73
20X-4	MAD	18	20	144.07	29.37	41.59	2.76	1.84	1.30	52.81	1.12	18.08
20X-5	MAD	16	18	145.17	32.71	48.61	2.74	1.77	1.19	56.52	1.30	17.37
20X-6	MAD	19	21	146.70	30.22	43.31	2.71	1.81	1.26	53.39	1.15	17.76
20X-7	MAD	9	11	148.10	28.21	39.29	2.75	1.87	1.34	51.35	1.06	18.30
21X-1	MAD	25	27	150.25	30.15	43.17	2.78	1.83	1.28	53.90	1.17	17.97
21X-3	MAD	9	11	153.09	30.32	43.52	2.76	1.82	1.27	53.91	1.17	17.88
21X-4	MAD	7	9	154.57	26.81	36.64	2.72	1.89	1.38	49.30	0.97	18.49
21X-5	MAD	6	8	156.06	25.47	34.18	2.71	1.91	1.42	47.43	0.90	18.72
21X-6	MAD	8	10	157.58	27.49	37.91	2.76	1.88	1.37	50.51	1.02	18.47
22X-1	MAD	56	58	160.16	27.92	38.73	2.75	1.87	1.35	50.95	1.04	18.35
22X-2	MAD	53	55	161.63	29.20	41.24	2.77	1.85	1.31	52.71	1.11	18.15
22X-3	MAD	35	37	162.95	29.25	41.34	2.72	1.83	1.30	52.27	1.10	17.97
23X-1	MAD	29	31	169.49	30.96	44.85	2.73	1.80	1.24	54.40	1.19	17.66
23X-2	MAD	17	19	170.87	26.64	36.31	2.75	1.90	1.39	49.32	0.97	18.61
23X-3	MAD	18	20	172.38	32.87	48.96	2.69	1.75	1.18	56.19	1.28	17.19
23X-4	MAD	17	19	173.87	29.44	41.73	2.75	1.84	1.30	52.86	1.12	18.05
23X-5	MAD	33	35	175.53	27.39	37.71	2.75	1.88	1.37	50.32	1.01	18.47
23X-6	MAD	26	28	176.96	28.75	40.36	2.76	1.86	1.32	52.07	1.09	18.21

Table 13. Vane shear strength results for Hole NGHP-01-14A.

Core, section	Sample	Top (cm)	Depth (mbsf)	Sv (kPa)	Sres (kPa)	Srem (kPa)	St
			NGHP-01-14A				
1H-2	VS	50	2.00	4.1	3.3	1.6	2.5
1H-3	VS	35	3.35	5.8	3.3	1.6	3.5
2H-1	VS	50	5.00	6.6	4.9	4.1	1.6
2H-2	VS	44	6.44	9.1	4.9	3.3	2.8
2H-3	VS	25	7.75	10.7	6.6	4.1	2.6
2H-4	VS	25	9.25	9.9	4.9	2.5	4.0
2H-5	VS	25	10.75	14.8	10.7	5.8	2.6
2H-6	VS	25	12.25	14.8	9.1	4.9	3.0
2H-7	VS	25	13.25	18.9	12.3	4.9	3.8
3H-1	VS	125	15.25	18.1	9.9	4.9	3.7
3H-2	VS	45	15.95	16.5	6.6	6.6	2.5
3H-3	VS	25	17.25	19.7	13.2	10.7	1.8
3H-4	VS	25	18.75	21.4	16.5	7.4	2.9
3H-5	VS	25	20.25	23.0	14.8	8.2	2.8
3H-6	VS	25	21.75	28.0	18.1	9.9	2.8
3H-7	VS	23	22.73	22.2	11.5	9.9	2.3
4H-1	VS	40	23.90	29.5	18.1	10.4	2.8
4H-2	VS	16	25.16	37.4	23.9	12.6	3.0

Table 14. Torvane strength results for Hole NGHP-01-14A.—Continued

Core, section	Sample	Top (cm)	Bot (cm)	Depth (mbsf)	Stv (kPa)
			NGHP-01-14A		
2H-1	TV	30	32	4.80	29.4
2H-2	TV	30	32	6.30	24.5
2H-3	TV	30	32	7.80	34.3
2H-4	TV	30	32	9.30	39.2
2H-6	TV	26	28	12.26	14.7
2H-7	TV	26	28	13.26	14.7
3H-1	TV	112	114	15.12	4.9
3H-2	TV	16	18	15.66	4.9
3H-3	TV	16	18	17.16	14.7
3H-4	TV	16	18	18.66	9.8
3H-5	TV	26	28	20.26	19.6
3H-6	TV	26	28	21.76	29.4
3H-7	TV	26	28	22.76	9.8
4H-1	TV	59	61	24.09	31.4
4H-2	TV	9	11	25.09	41.2
4H-3	TV	6	8	26.56	22.6
4H-4	TV	9	11	28.09	41.2
4H-5	TV	21	23	29.71	19.6
4H-6	TV	14	16	31.14	49.0
4H-7	TV	17	19	32.67	42.2
5H-1	TV	50	52	33.50	41.2
5H-2	TV	12	14	34.62	45.1
5H-3	TV	9	11	36.09	49.0
5H-4	TV	42	44	37.92	49.0
5H-5	TV	22	24	39.22	56.9
5H-6	TV	25	27	40.75	65.7
6H-1	TV	9	11	42.59	53.0
6H-2	TV	14	16	44.14	19.6
6H-3	TV	20	22	45.70	51.0

Table 14. Torvane strength results for Hole NGHP-01-14A.—Continued

Core, section	Sample	Top (cm)	Bot (cm)	Depth (mbsf)	Stv (kPa)
		NGHP-01-14A—Continued			
6H-4	TV	9	11	47.09	51.0
6H-5	TV	14	16	48.64	59.8
6H-6	TV	25	27	50.13	63.7
6H-7	TV	11	13	51.31	60.8
7H-1	TV	7	9	52.07	20.6
7H-2	TV	17	19	53.67	40.2
7H-3	TV	5	7	54.98	51.0
7H-4	TV	4	6	56.42	43.1
7H-5	TV	5	7	57.93	45.1
7H-6	TV	7	9	59.45	45.1
7H-7	TV	28	30	60.60	58.8
8H-1	TV	15	17	61.65	23.5
8H-2	TV	18	20	62.38	68.6
8H-3	TV	25	27	63.95	49.0
8H-4	TV	19	21	65.36	74.5
8H-6	TV	32	34	68.09	53.9
8H-7	TV	32	34	69.11	53.9
11X-1	TV	28	30	73.28	14.7
11X-2	TV	28	30	74.78	44.1
11X-3	TV	28	30	76.14	24.5
11X-4	TV	11	13	77.47	36.8
12X-1	TV	16	18	82.76	19.6
12X-2	TV	16	18	84.26	14.7
12X-3	TV	16	18	85.26	29.4
12X-4	TV	16	18	86.41	34.3
12X-5	TV	16	18	87.91	34.3
12X-6	TV	16	18	89.41	34.3
13X-1	TV	25	27	92.45	4.9
13X-2	TV	25	27	93.95	44.1
13X-3	TV	25	27	95.45	24.5
13X-4	TV	25	27	96.95	19.6
13X-5	TV	25	27	98.45	44.1
13X-6	TV	25	27	99.95	44.1
16X-1	TV	8	10	102.08	44.1
16X-2	TV	8	10	103.58	14.7
16X-3	TV	8	10	105.08	29.4
16X-4	TV	8	10	106.58	29.4
16X-5	TV	8	10	108.08	19.6
16X-6	TV	8	10	109.50	14.7
17X-1	TV	34	36	111.94	24.5
17X-2	TV	34	36	113.33	53.9
19X-2	TV	38	40	132.68	44.1
19X-3	TV	38	40	134.18	58.8
19X-4	TV	38	40	135.68	73.5
19X-5	TV	38	40	136.85	68.6
19X-6	TV	38	40	138.22	29.4
19X-7	TV	38	40	139.72	73.5
20X-2	TV	5	7	140.94	66.7
20X-3	TV	8	10	142.47	65.7
20X-4	TV	18	20	144.07	68.6
20X-5	TV	15	17	145.16	72.6
20X-6	TV	19	21	146.70	65.7
20X-7	TV	10	12	148.11	58.8
21X-1	TV	31	33	150.31	53.9
21X-2	TV	5	7	151.55	72.6
21X-3	TV	6	8	153.06	66.7

Table 15. Pocket Penetrometer strength results for Hole NGHP-01-14A.

Core, section	Sample	Top (cm)	Depth (mbsf)	Spp (kPa)	Core, section	Sample	Top (cm)	Depth (mbsf)	Spp (kPa)
NGHP-01-14A									
1H-2	PP	50	2.00	1.5	12X-3	PP	20	85.30	36.8
1H-3	PP	98	3.98	1.5	12X-4	PP	20	86.45	36.8
2H-1	PP	47	4.97	3.8	12X-5	PP	20	87.95	39.2
2H-2	PP	43	6.43	4.9	12X-6	PP	20	89.45	36.8
2H-3	PP	37	7.87	4.6	13X-1	PP	35	92.55	24.5
2H-4	PP	25	9.25	6.1	13X-2	PP	35	94.05	49.0
2H-5	PP	25	10.75	8.4	13X-3	PP	35	95.55	49.0
2H-6	PP	31	12.31	7.7	13X-4	PP	35	97.05	73.5
2H-7	PP	31	13.31	9.2	13X-5	PP	35	98.55	73.5
3H-1	PP	125	15.25	10.0	13X-6	PP	35	100.05	73.5
3H-2	PP	46	15.96	11.0	16X-1	PP	18	102.18	24.5
3H-3	PP	25	17.25	8.4	16X-2	PP	18	103.68	36.8
3H-4	PP	26	18.76	11.5	16X-3	PP	18	105.18	36.8
3H-5	PP	21	20.21	11.3	16X-4	PP	18	106.68	73.5
3H-6	PP	26	21.76	13.0	16X-5	PP	18	108.18	73.5
3H-7	PP	16	22.66	12.3	16X-6	PP	18	109.60	73.5
4H-1	PP	72	24.22	34.3	17X-1	PP	25	111.85	73.5
4H-2	PP	23	25.23	49.0	17X-2	PP	25	113.24	63.7
4H-3	PP	10	26.60	29.4	18X-1	PP	25	121.45	24.5
4H-4	PP	20	28.20	24.5	18X-2	PP	25	122.45	73.5
4H-5	PP	20	29.70	24.5	18X-3	PP	25	123.61	98.0
4H-6	PP	10	31.10	29.4	19X-1	PP	36	131.16	61.3
4H-7	PP	9	32.59	39.2	19X-2	PP	36	132.66	61.3
5H-1	PP	56	33.56	36.8	19X-3	PP	36	134.16	85.8
5H-2	PP	17	34.67	49.0	19X-4	PP	36	135.66	73.5
5H-3	PP	18	36.18	39.2	19X-5	PP	36	136.83	85.8
5H-4	PP	23	37.73	58.8	19X-6	PP	36	138.20	73.5
5H-5	PP	14	39.14	58.8	19X-7	PP	36	139.70	73.5
5H-6	PP	27	40.77	58.8	20X-2	PP	10	140.99	85.8
6H-1	PP	14	42.64	61.3	20X-3	PP	18	142.57	83.3
6H-2	PP	8	44.08	29.4	20X-4	PP	30	144.19	98.0
6H-3	PP	10	45.60	53.9	20X-5	PP	10	145.11	85.8
6H-4	PP	7	47.07	34.3	20X-6	PP	16	146.67	68.6
6H-5	PP	10	48.60	49.0	20X-7	PP	6	148.07	78.4
6H-6	PP	23	50.11	58.8	21X-1	PP	25	150.25	44.1
6H-7	PP	8	51.28	49.0	21X-2	PP	10	151.60	73.5
7H-1	PP	14	52.14	24.5	21X-3	PP	10	153.10	78.4
7H-2	PP	10	53.60	49.0	21X-4	PP	8	154.58	171.5
7H-3	PP	10	55.03	44.1	21X-5	PP	6	156.06	110.3
7H-4	PP	8	56.46	39.2	21X-6	PP	9	157.59	171.5
7H-5	PP	10	57.98	49.0	22X-1	PP	56	160.16	142.1
7H-6	PP	6	59.44	61.3	22X-2	PP	10	161.20	137.2
7H-7	PP	5	60.37	61.3	22X-3	PP	8	162.68	98.0
8H-1	PP	34	61.84	49.0	23X-1	PP	30	169.50	34.3
8H-2	PP	34	62.54	61.3	23X-1	PP	74	169.94	58.8
8H-3	PP	34	64.04	49.0	23X-1	PP	126	170.46	76.0
8H-4	PP	34	65.51	61.3	23X-2	PP	17	170.87	85.8
8H-5	PP	30	66.57	61.3	23X-2	PP	94	171.64	98.0
8H-6	PP	30	68.07	36.8	23X-2	PP	140	172.10	112.7
8H-7	PP	30	69.09	36.8	23X-3	PP	19	172.39	95.6
11X-1	PP	18	73.18	12.3	23X-3	PP	69	172.89	122.5
11X-2	PP	18	74.68	24.5	23X-4	PP	18	173.88	95.6
11X-3	PP	18	76.04	36.8	23X-4	PP	95	174.65	125.0
11X-4	PP	18	77.54	36.8	23X-5	PP	34	175.54	137.2
12X-1	PP	20	82.80	24.5	23X-6	PP	27	176.97	132.3
12X-2	PP	20	84.30	36.8					

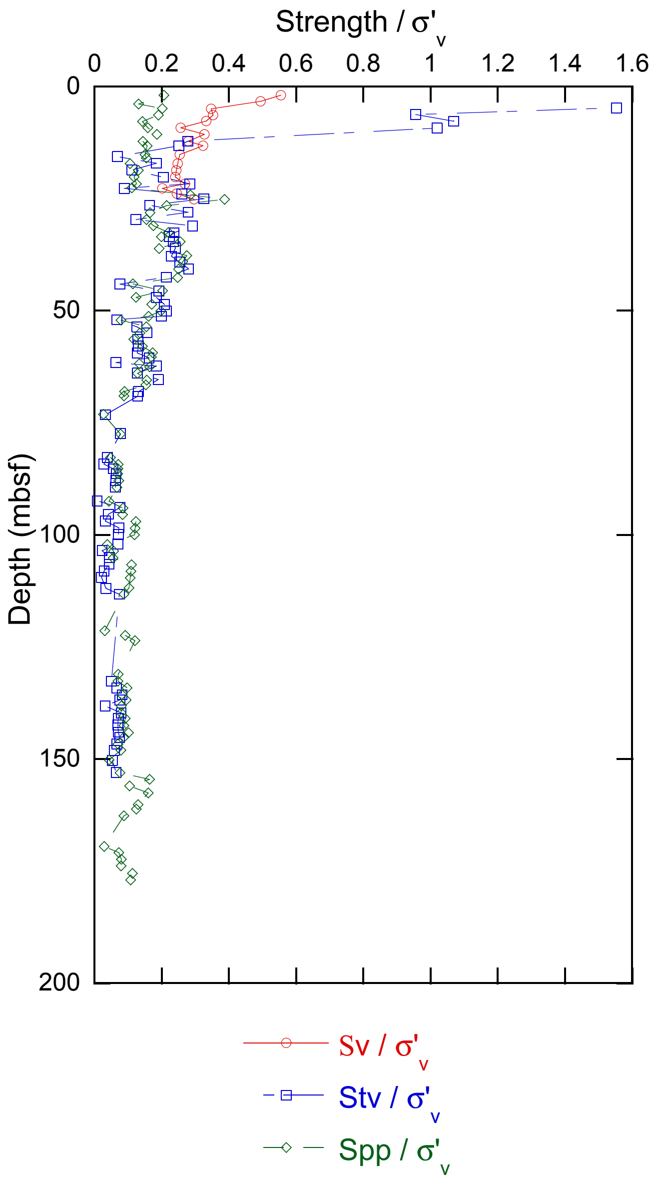

Figure 22. Shear strengths normalized by the effective vertical stress versus sub-bottom depth for Hole NGHP-01-14A.

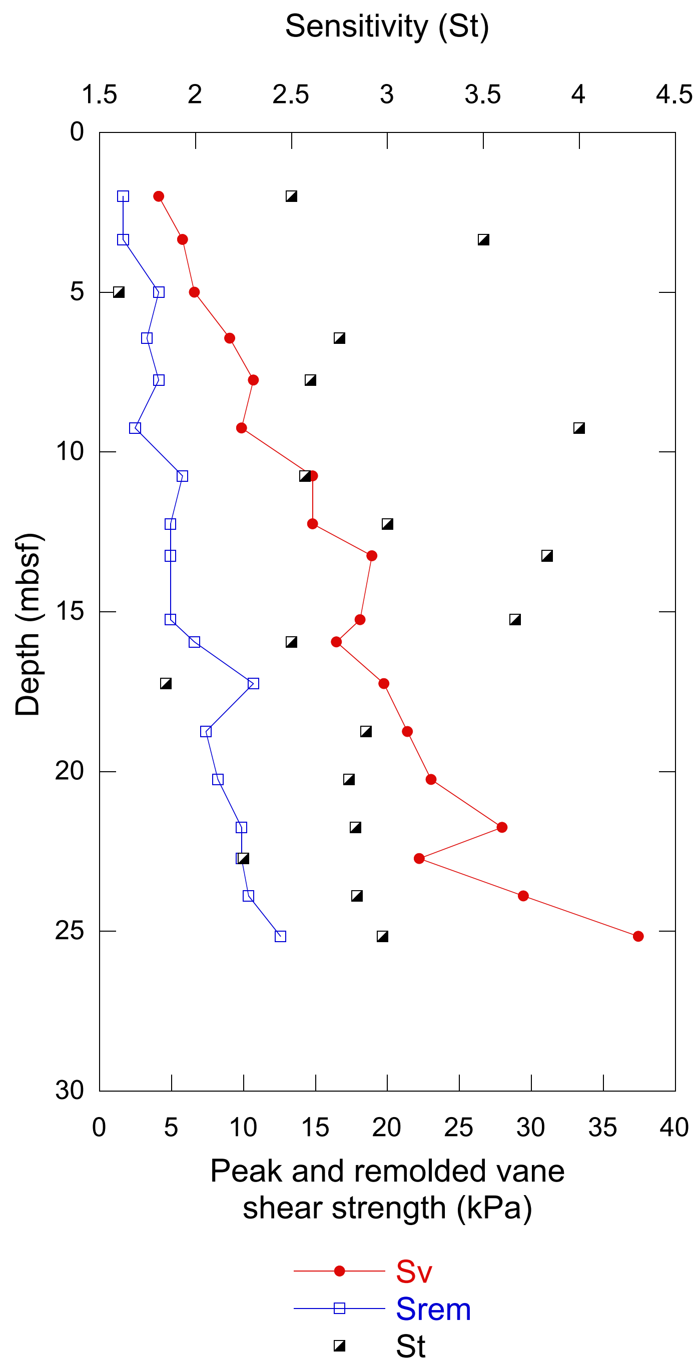

Figure 23. Peak and remolded vane shear strengths and sensitivity for Hole NGHP-01-14A. [Sv, peak vane shear strength; Srem, remolded vane shear strength; St, shear strength sensitivity; mbsf, meters below sea floor; kPa, kilopascals]

Table 16. Wenner array electrical resistivity and apparent formation factor results for Hole NGHP-01-14A. (To view complete table, please refer to the ASCII files.)

Core, section	Sample	Top (cm)	Depth (mbsf)	Electrical resistivity (Ω×m)	Apparent formation factor
			NGHP-01-14A		
1H-2	ER	40	1.90	0.511	2.56
1H-2	ER	60	2.10	0.455	2.28
1H-2	ER	80	2.30	0.721	3.61
1H-2	ER	100	2.50	0.331	1.66
1H-2	ER	120	2.70	0.419	2.10
1H-3	ER	15	3.15	0.35	1.75
1H-3	ER	35	3.35	0.356	1.78
1H-3	ER	55	3.55	0.394	1.97
1H-3	ER	75	3.75	0.358	1.79
2H-1	ER	15	4.65	0.365	1.83
2H-1	ER	40	4.90	0.431	2.16
2H-1	ER	60	5.10	0.366	1.83
2H-1	ER	80	5.30	0.365	1.83
2H-1	ER	100	5.50	0.334	1.67
2H-1	ER	120	5.70	0.456	2.28
2H-2	ER	15	6.15	0.387	1.94
2H-2	ER	40	6.40	0.406	2.03
2H-2	ER	60	6.60	0.347	1.74
2H-2	ER	80	6.80	0.319	1.60
2H-2	ER	100	7.00	0.344	1.72
2H-2	ER	120	7.20	0.357	1.79
2H-3	ER	15	7.65	0.381	1.91
2H-3	ER	40	7.90	0.367	1.84
2H-3	ER	60	8.10	0.391	1.96
2H-3	ER	80	8.30	0.398	1.99
2H-4	ER	15	9.15	0.395	1.98
2H-4	ER	40	9.40	0.394	1.97
2H-4	ER	60	9.60	0.409	2.05
2H-4	ER	80	9.80	0.409	2.05
2H-4	ER	100	10.00	0.394	1.97
2H-4	ER	120	10.20	0.367	1.84
2H-5	ER	20	10.70	0.426	2.13
2H-5	ER	40	10.90	0.398	1.99
2H-5	ER	60	11.10	0.427	2.14
2H-5	ER	80	11.30	0.395	1.98
2H-6	ER	20	12.20	0.414	2.07
2H-6	ER	40	12.40	0.757	3.79
2H-6	ER	60	12.60	0.386	1.93
2H-6	ER	80	12.80	0.396	1.98
2H-7	ER	20	13.20	0.388	1.94
2H-7	ER	40	13.40	0.405	2.03
2H-7	ER	60	13.60	0.382	1.91
2H-7	ER	80	13.80	0.374	1.87
3H-1	ER	80	14.80	0.442	2.21
3H-1	ER	100	15.00	0.463	2.32
3H-1	ER	130	15.30	0.416	2.08
3H-2	ER	15	15.65	0.528	2.64
3H-2	ER	35	15.85	0.486	2.43
3H-2	ER	55	16.05	0.383	1.92
3H-2	ER	75	16.25	0.423	2.12
3H-3	ER	15	17.15	0.4	2.00
3H-3	ER	35	17.35	0.436	2.18
3H-3	ER	55	17.55	0.511	2.56
3H-3	ER	75	17.75	0.438	2.19
3H-3	ER	95	17.95	0.456	2.28
3H-4	ER	15	18.65	0.426	2.13

Table 16. Wenner array electrical resistivity and apparent formation factor results for Hole NGHP-01-14A. (To view complete table, please refer to the ASCII files.)—Continued

Core, section	Sample	Top (cm)	Depth (mbsf)	Electrical resistivity (Ω×m)	Apparent formation factor
NGHP-01-14A—Continued					
3H-4	ER	35	18.85	0.527	2.64
3H-4	ER	55	19.05	0.401	2.01
3H-4	ER	75	19.25	0.384	1.92
3H-4	ER	95	19.45	0.421	2.11
3H-4	ER	115	19.65	0.395	1.98
3H-5	ER	15	20.15	0.711	3.56
3H-5	ER	35	20.35	0.406	2.03
3H-5	ER	55	20.55	0.394	1.97
3H-5	ER	75	20.75	0.551	2.76
3H-6	ER	15	21.65	0.411	2.06
3H-6	ER	25	21.75	0.39	1.95
3H-6	ER	55	22.05	0.398	1.99
3H-6	ER	75	22.25	0.389	1.95
3H-7	ER	15	22.65	0.437	2.19
3H-7	ER	35	22.85	0.423	2.12
3H-7	ER	55	23.05	0.397	1.99
3H-7	ER	75	23.25	0.516	2.58
4H-1	ER	40	23.90	0.535	2.68
4H-1	ER	60	24.10	0.661	3.31
4H-1	ER	80	24.30	0.695	3.48
4H-1	ER	100	24.50	0.594	2.97
4H-1	ER	120	24.70	0.608	3.04
4H-1	ER	140	24.90	0.658	3.29
4H-2	ER	15	25.15	0.684	3.42
4H-2	ER	35	25.35	0.699	3.50
4H-2	ER	55	25.55	0.738	3.69
4H-2	ER	75	25.75	0.611	3.06
4H-2	ER	95	25.95	0.603	3.02
4H-2	ER	115	26.15	0.525	2.63
4H-2	ER	138	26.38	0.663	3.32
4H-3	ER	17	26.67	0.816	4.08
4H-3	ER	35	26.85	0.613	3.07
4H-3	ER	55	27.05	0.69	3.45
4H-3	ER	75	27.25	0.513	2.57
4H-3	ER	95	27.45	0.586	2.93
4H-4	ER	20	28.20	0.696	3.48
4H-4	ER	46	28.46	0.613	3.07
4H-4	ER	70	28.70	0.439	2.20
4H-4	ER	96	28.96	0.565	2.83
4H-4	ER	118	29.18	0.644	3.22
4H-4	ER	140	29.40	0.656	3.28
4H-5	ER	28	29.78	0.518	2.59
4H-5	ER	48	29.98	0.486	2.43
4H-5	ER	72	30.22	0.468	2.34
4H-5	ER	93	30.43	0.516	2.58
4H-6	ER	20	31.20	0.568	2.84
4H-6	ER	39	31.39	0.547	2.74
4H-6	ER	56	31.56	0.531	2.66
4H-6	ER	72	31.72	0.589	2.95
4H-6	ER	92	31.92	0.564	2.82
4H-6	ER	112	32.12	0.591	2.96
4H-7	ER	18	32.68	0.689	3.45
4H-7	ER	31	32.81	0.571	2.86
4H-7	ER	58	33.08	0.633	3.17
5H-1	ER	40	33.40	0.6	3.00
5H-2	ER	35	34.85	0.776	3.88

Table 16. Wenner array electrical resistivity and apparent formation factor results for Hole NGHP-01-14A. (To view complete table, please refer to the ASCII files.)—Continued

Core, section	Sample	Top (cm)	Depth (mbsf)	Electrical resistivity (Ω×m)	Apparent formation factor
			NGHP-01-14A—Continued		
5H-2	ER	60	35.10	0.556	2.78
5H-2	ER	80	35.30	0.538	2.69
5H-2	ER	95	35.45	0.565	2.83
5H-2	ER	122	35.72	0.604	3.02
5H-2	ER	142	35.92	0.494	2.47
5H-3	ER	15	36.15	0.526	2.63
5H-3	ER	36	36.36	0.64	3.20
5H-3	ER	40	36.40	0.536	2.68
5H-3	ER	67	36.67	0.58	2.90
5H-3	ER	89	36.89	0.722	3.61
5H-3	ER	105	37.05	0.587	2.94
5H-4	ER	22	37.72	0.61	3.05
5H-4	ER	43	37.93	0.554	2.77
5H-4	ER	60	38.10	0.567	2.84
5H-4	ER	83	38.33	0.549	2.75
5H-4	ER	96	38.46	0.763	3.82
5H-4	ER	123	38.73	0.623	3.12
5H-4	ER	132	38.82	0.566	2.83
5H-5	ER	15	39.15	0.527	2.64
5H-5	ER	38	39.38	0.583	2.92
5H-5	ER	56	39.56	0.582	2.91
5H-5	ER	76	39.76	0.583	2.92
5H-5	ER	95	39.95	0.652	3.26
5H-6	ER	11	40.61	0.507	2.54
5H-6	ER	22	40.72	0.565	2.83
5H-6	ER	56	41.06	0.624	3.12
5H-6	ER	80	41.30	0.514	2.57
5H-6	ER	124	41.74	0.481	2.41
5H-6	ER	125	41.75	0.583	2.92
6H-1	ER	13	42.63	0.491	2.46
6H-1	ER	33	42.83	0.562	2.81
6H-1	ER	53	43.03	0.505	2.53
6H-1	ER	73	43.23	0.523	2.62
6H-1	ER	93	43.43	0.472	2.36
6H-1	ER	113	43.63	0.634	3.17
6H-1	ER	133	43.83	0.526	2.63
6H-2	ER	15	44.15	0.545	2.73
6H-2	ER	35	44.35	0.532	2.66
6H-2	ER	55	44.55	0.53	2.65
6H-2	ER	82	44.82	0.54	2.70
6H-2	ER	103	45.03	0.563	2.82
6H-2	ER	123	45.23	0.638	3.19
6H-2	ER	144	45.44	0.643	3.22
6H-3	ER	8	45.58	0.602	3.01
6H-3	ER	28	45.78	0.555	2.78
6H-3	ER	46	45.96	0.564	2.82
6H-3	ER	69	46.19	0.548	2.74
6H-3	ER	85	46.35	0.615	3.08
6H-4	ER	10	47.10	0.558	2.79
6H-4	ER	30	47.30	0.517	2.59
6H-4	ER	50	47.50	0.566	2.83
6H-4	ER	70	47.70	0.546	2.73
6H-4	ER	90	47.90	0.471	2.36
6H-4	ER	110	48.10	0.525	2.63
6H-4	ER	132	48.32	0.515	2.58
6H-5	ER	15	48.65	0.516	2.58

Table 16. Wenner array electrical resistivity and apparent formation factor results for Hole NGHP-01-14A. (To view complete table, please refer to the ASCII files.)—Continued

Core, section	Sample	Top (cm)	Depth (mbsf)	Electrical resistivity (Ω×m)	Apparent formation factor
NGHP-01-14A—Continued					
6H-5	ER	35	48.85	0.571	2.86
6H-5	ER	55	49.05	0.573	2.87
6H-5	ER	70	49.20	0.538	2.69
6H-6	ER	21	50.09	0.559	2.80
6H-6	ER	42	50.30	0.577	2.89
6H-6	ER	63	50.51	0.513	2.57
6H-6	ER	83	50.71	0.52	2.60
6H-6	ER	103	50.91	0.593	2.97
6H-7	ER	10	51.30	0.593	2.97
6H-7	ER	30	51.50	0.493	2.47
6H-7	ER	62	51.82	0.594	2.97
7H-1	ER	15	52.15	0.496	2.48
7H-1	ER	35	52.35	0.485	2.43
7H-1	ER	55	52.55	0.524	2.62
7H-1	ER	75	52.75	0.451	2.26
7H-1	ER	95	52.95	0.516	2.58
7H-1	ER	119	53.19	0.498	2.49
7H-2	ER	15	53.65	0.472	2.36
7H-2	ER	35	53.85	0.529	2.65
7H-2	ER	60	54.10	0.783	3.92
7H-2	ER	86	54.36	0.653	3.27
7H-2	ER	117	54.67	0.567	2.84
7H-2	ER	133	54.83	0.521	2.61
7H-3	ER	10	55.03	0.558	2.79
7H-3	ER	30	55.23	0.536	2.68
7H-3	ER	50	55.43	0.523	2.62
7H-3	ER	70	55.63	0.545	2.73
7H-3	ER	88	55.81	0.501	2.51
7H-4	ER	9	56.47	0.469	2.35
7H-4	ER	25	56.63	0.474	2.37
7H-4	ER	50	56.88	0.515	2.58
7H-4	ER	70	57.08	0.504	2.52
7H-4	ER	100	57.38	0.583	2.92
7H-4	ER	124	57.62	0.62	3.10
7H-4	ER	140	57.78	0.518	2.59
7H-5	ER	11	57.99	0.567	2.84
7H-5	ER	40	58.28	0.556	2.78
7H-5	ER	60	58.48	0.523	2.62
7H-5	ER	83	58.71	0.611	3.06
7H-6	ER	15	59.53	0.59	2.95
7H-6	ER	41	59.79	0.474	2.37
7H-6	ER	67	60.05	0.511	2.56
7H-6	ER	81	60.19	0.565	2.83
7H-7	ER	8	60.40	0.523	2.62
7H-7	ER	29	60.61	0.461	2.31
7H-7	ER	51	60.83	0.479	2.40
8H-1	ER	16	61.66	0.575	2.88
8H-1	ER	35	61.85	0.58	2.90
8H-1	ER	55	62.05	0.563	2.82
8H-2	ER	15	62.35	0.7	3.50
8H-2	ER	35	62.55	0.628	3.14
8H-2	ER	54	62.74	0.62	3.10
8H-2	ER	77	62.97	0.691	3.46
8H-2	ER	94	63.14	0.565	2.83
8H-2	ER	121	63.41	0.622	3.11
8H-2	ER	138	63.58	0.643	3.22

Table 16. Wenner array electrical resistivity and apparent formation factor results for Hole NGHP-01-14A. (To view complete table, please refer to the ASCII files.)—Continued

Core, section	Sample	Top (cm)	Depth (mbsf)	Electrical resistivity (Ω×m)	Apparent formation factor
NGHP-01-14A—Continued					
8H-3	ER	18	63.88	0.632	3.16
8H-3	ER	36	64.06	0.681	3.41
8H-3	ER	56	64.26	0.599	3.00
8H-3	ER	78	64.48	0.64	3.20
8H-4	ER	15	65.32	0.523	2.62
8H-4	ER	35	65.52	0.722	3.61
8H-4	ER	55	65.72	0.733	3.67
8H-4	ER	75	65.92	0.615	3.08
8H-4	ER	95	66.12	0.652	3.26
8H-4	ER	108	66.25	0.632	3.16
8H-5	ER	24	66.51	0.558	2.79
8H-5	ER	42	66.69	0.622	3.11
8H-5	ER	62	66.89	0.62	3.10
8H-5	ER	85	67.12	0.535	2.68
8H-6	ER	12	67.89	0.514	2.57
8H-6	ER	34	68.11	0.567	2.84
8H-6	ER	80	68.57	0.55	2.75
8H-7	ER	11	68.90	0.613	3.07
8H-7	ER	28	69.07	0.594	2.97
8H-7	ER	48	69.27	0.643	3.22
8H-7	ER	68	69.47	0.661	3.31
8H-7	ER	89	69.68	0.6	3.00
8H-7	ER	109	69.88	0.547	2.74
8H-7	ER	129	70.08	0.587	2.94
11X-1	ER	15	73.15	0.515	2.58
11X-1	ER	35	73.35	0.507	2.54
11X-1	ER	55	73.55	0.718	3.59
11X-1	ER	55	73.55	0.61	3.05
11X-1	ER	75	73.75	0.351	1.76
11X-1	ER	75	73.75	0.568	2.84
11X-1	ER	95	73.95	0.558	2.79
11X-1	ER	115	74.15	0.525	2.63
11X-2	ER	15	74.65	0.525	2.63
11X-2	ER	35	74.85	0.603	3.02
11X-2	ER	60	75.10	0.587	2.94
11X-3	ER	15	76.01	0.566	2.83
11X-3	ER	35	76.21	0.545	2.73
11X-3	ER	55	76.41	0.516	2.58
11X-3	ER	75	76.61	0.477	2.39
11X-3	ER	95	76.81	0.584	2.92
11X-4	ER	15	77.51	0.579	2.90
11X-4	ER	35	77.71	0.506	2.53
11X-4	ER	55	77.91	0.548	2.74
12X-1	ER	20	82.80	0.495	2.48
12X-1	ER	40	83.00	0.493	2.47
12X-1	ER	60	83.20	0.569	2.85
12X-1	ER	80	83.40	0.536	2.68
12X-1	ER	100	83.60	0.538	2.69
12X-1	ER	120	83.80	0.524	2.62
12X-2	ER	15	84.25	0.605	3.03
12X-2	ER	35	84.45	0.551	2.76
12X-2	ER	55	84.65	0.632	3.16
12X-2	ER	75	84.85	0.84	4.20
12X-2	ER	95	85.05	0.547	2.74
12X-3	ER	15	85.25	0.562	2.81
12X-3	ER	35	85.45	0.54	2.70

Table 16. Wenner array electrical resistivity and apparent formation factor results for Hole NGHP-01-14A. (To view complete table, please refer to the ASCII files.)—Continued

Core, section	Sample	Top (cm)	Depth (mbsf)	Electrical resistivity (Ω×m)	Apparent formation factor
NGHP-01-14A—Continued					
12X-3	ER	55	85.65	0.688	3.44
12X-4	ER	15	86.40	0.517	2.59
12X-4	ER	40	86.65	0.544	2.72
12X-4	ER	60	86.85	0.505	2.53
12X-4	ER	80	87.05	0.535	2.68
12X-4	ER	100	87.25	0.531	2.66
12X-4	ER	120	87.45	0.55	2.75
12X-5	ER	15	87.90	0.523	2.62
12X-5	ER	35	88.10	0.488	2.44
12X-5	ER	55	88.30	0.462	2.31
12X-5	ER	75	88.50	0.535	2.68
12X-6	ER	15	89.40	0.428	2.14
12X-6	ER	35	89.60	0.531	2.66
12X-6	ER	55	89.80	0.494	2.47
12X-6	ER	75	90.00	0.509	2.55
13X-1	ER	15	92.35	0.569	2.85
13X-1	ER	35	92.55	0.55	2.75
13X-1	ER	55	92.75	0.517	2.59
13X-1	ER	75	92.95	0.545	2.73
13X-1	ER	95	93.15	0.594	2.97
13X-1	ER	115	93.35	0.616	3.08
13X-1	ER	135	93.55	0.729	3.65
13X-2	ER	15	93.85	0.638	3.19
13X-2	ER	35	94.05	0.536	2.68
13X-2	ER	55	94.25	0.684	3.42
13X-2	ER	75	94.45	0.609	3.05
13X-2	ER	95	94.65	0.531	2.66
13X-2	ER	115	94.85	0.626	3.13
13X-2	ER	135	95.05	0.61	3.05
13X-3	ER	20	95.40	0.539	2.70
13X-3	ER	40	95.60	0.605	3.03
13X-3	ER	60	95.80	0.52	2.60
13X-3	ER	80	96.00	0.631	3.16
13X-4	ER	15	96.85	0.584	2.92
13X-4	ER	35	97.05	0.592	2.96
13X-4	ER	55	97.25	0.533	2.67
13X-4	ER	75	97.45	0.599	3.00
13X-4	ER	95	97.65	0.569	2.85
13X-4	ER	115	97.85	0.577	2.89
13X-4	ER	135	98.05	0.557	2.79
13X-5	ER	15	98.35	0.578	2.89
13X-5	ER	35	98.55	0.516	2.58
13X-5	ER	55	98.75	0.519	2.60
13X-5	ER	75	98.95	0.611	3.06
13X-6	ER	15	99.85	0.606	3.03
13X-6	ER	35	100.05	0.606	3.03
13X-6	ER	55	100.25	0.658	3.29
13X-6	ER	75	100.45	0.627	3.14
13X-6	ER	95	100.65	0.644	3.22
16X-1	ER	15	102.15	0.642	3.21
16X-1	ER	35	102.35	0.594	2.97
16X-1	ER	55	102.55	0.588	2.94
16X-1	ER	75	102.75	0.561	2.81
16X-2	ER	15	103.65	0.535	2.68
16X-3	ER	15	105.15	0.644	3.22
16X-3	ER	35	105.35	0.545	2.73
16X-3	ER	55	105.55	0.637	3.19

Table 16. Wenner array electrical resistivity and apparent formation factor results for Hole NGHP-01-14A. (To view complete table, please refer to the ASCII files.)—Continued

Core, section	Sample	Top (cm)	Depth (mbsf)	Electrical resistivity (Ω×m)	Apparent formation factor
			NGHP-01-14A—Continued		
16X-3	ER	75	105.75	0.72	3.60
16X-4	ER	15	106.65	0.764	3.82
16X-4	ER	35	106.85	0.826	4.13
16X-4	ER	55	107.05	0.728	3.64
16X-5	ER	22	108.22	0.629	3.15
16X-5	ER	42	108.42	0.533	2.67
16X-5	ER	62	108.62	0.793	3.97
16X-5	ER	82	108.82	0.631	3.16
16X-5	ER	110	109.10	0.779	3.90
16X-5	ER	130	109.30	0.856	4.28
16X-6	ER	81	110.23	0.762	3.81
16X-6	ER	105	110.47	0.888	4.44
17X-1	ER	20	111.80	0.737	3.69
17X-1	ER	40	112.00	0.727	3.64
17X-1	ER	75	112.35	0.783	3.92
17X-2	ER	15	113.14	0.756	3.78
17X-2	ER	35	113.34	0.778	3.89
17X-2	ER	55	113.54	0.709	3.55
18X-1	ER	22	121.42	0.556	2.78
18X-1	ER	50	121.70	0.712	3.56
18X-2	ER	25	122.45	0.783	3.92
18X-3	ER	15	123.51	0.65	3.25
18X-3	ER	30	123.66	0.571	2.86
18X-3	ER	65	124.01	0.73	3.65
19X-1	ER	30	131.10	0.614	3.07
19X-1	ER	69	131.49	0.51	2.55
19X-1	ER	89	131.69	0.62	3.10
19X-1	ER	110	131.90	0.573	2.87
19X-1	ER	130	132.10	0.632	3.16
19X-2	ER	15	132.45	0.667	3.34
19X-2	ER	35	132.65	0.528	2.64
19X-2	ER	55	132.85	0.614	3.07
19X-2	ER	75	133.05	0.634	3.17
19X-2	ER	100	133.30	0.625	3.13
19X-2	ER	120	133.50	0.629	3.15
19X-3	ER	15	133.95	0.596	2.98
19X-3	ER	35	134.15	0.586	2.93
19X-3	ER	55	134.35	0.551	2.76
19X-3	ER	75	134.55	0.569	2.85
19X-3	ER	95	134.75	0.593	2.97
19X-4	ER	25	135.55	0.567	2.84
19X-5	ER	15	136.62	0.617	3.09
19X-5	ER	35	136.82	0.558	2.79
19X-5	ER	55	137.02	0.601	3.01
19X-5	ER	75	137.22	0.635	3.18
19X-5	ER	95	137.42	0.585	2.93
19X-5	ER	120	137.67	0.598	2.99
19X-6	ER	15	137.99	0.624	3.12
19X-6	ER	35	138.19	0.491	2.46
19X-6	ER	55	138.39	0.621	3.11
19X-6	ER	75	138.59	0.681	3.41
19X-6	ER	95	138.79	0.515	2.58
19X-6	ER	115	138.99	0.627	3.14
19X-6	ER	135	139.19	0.559	2.80
19X-7	ER	15	139.49	0.569	2.85
19X-7	ER	35	139.69	0.644	3.22
19X-7	ER	55	139.89	0.568	2.84

Table 16. Wenner array electrical resistivity and apparent formation factor results for Hole NGHP-01-14A. (To view complete table, please refer to the ASCII files.)—Continued

Core, section	Sample	Top (cm)	Depth (mbsf)	Electrical resistivity (Ω×m)	Apparent formation factor
		NGHP-01-14A—Continued			
20X-2	ER	15	141.04	0.706	3.53
20X-2	ER	34	141.23	0.66	3.30
20X-2	ER	61	141.50	0.627	3.14
20X-2	ER	70	141.59	0.671	3.36
20X-2	ER	91	141.80	0.62	3.10
20X-2	ER	111	142.00	0.749	3.75
20X-2	ER	131	142.20	0.654	3.27
20X-2	ER	144	142.33	0.608	3.04
20X-3	ER	15	142.54	0.605	3.03
20X-3	ER	37	142.76	0.621	3.11
20X-3	ER	57	142.96	0.636	3.18
20X-3	ER	77	143.16	0.597	2.99
20X-3	ER	98	143.37	0.578	2.89
20X-3	ER	114	143.53	0.605	3.03
20X-3	ER	129	143.68	0.564	2.82
20X-4	ER	16	144.05	0.633	3.17
20X-4	ER	36	144.25	0.68	3.40
20X-5	ER	13	145.14	0.644	3.22
20X-5	ER	46	145.47	0.656	3.28
20X-5	ER	67	145.68	0.759	3.80
20X-5	ER	84	145.85	0.703	3.52
20X-5	ER	104	146.05	0.686	3.43
20X-5	ER	124	146.25	0.707	3.54
20X-6	ER	15	146.66	0.788	3.94
20X-6	ER	35	146.86	0.68	3.40
20X-6	ER	67	147.18	0.636	3.18
20X-6	ER	90	147.41	0.628	3.14
20X-6	ER	110	147.61	0.693	3.47
20X-6	ER	130	147.81	0.717	3.59
20X-6	ER	143	147.94	0.695	3.48
20X-7	ER	27	148.28	0.694	3.47
21X-1	ER	25	150.25	0.662	3.31
21X-1	ER	45	150.45	0.749	3.75
21X-1	ER	75	150.75	0.755	3.78
21X-1	ER	95	150.95	0.72	3.60
21X-1	ER	115	151.15	0.725	3.63
21X-1	ER	135	151.35	0.796	3.98
21X-2	ER	15	151.65	0.649	3.25
21X-2	ER	35	151.85	0.572	2.86
21X-2	ER	56	152.06	0.594	2.97
21X-2	ER	75	152.25	0.755	3.78
21X-2	ER	95	152.45	0.805	4.03
21X-2	ER	116	152.66	0.616	3.08
21X-3	ER	15	153.15	0.667	3.34
21X-3	ER	36	153.36	0.753	3.77
21X-3	ER	56	153.56	0.65	3.25
21X-3	ER	69	153.69	0.684	3.42
21X-4	ER	8	154.58	0.755	3.78
21X-4	ER	36	154.86	0.868	4.34
21X-4	ER	56	155.06	0.689	3.45
21X-4	ER	75	155.25	0.767	3.84
21X-4	ER	98	155.48	0.682	3.41
21X-4	ER	117	155.67	0.776	3.88
21X-4	ER	136	155.86	0.672	3.36
21X-5	ER	15	156.15	0.682	3.41
21X-5	ER	35	156.35	0.927	4.64
21X-5	ER	56	156.56	0.661	3.31
21X-5	ER	75	156.75	0.899	4.50

Table 16. Wenner array electrical resistivity and apparent formation factor results for Hole NGHP-01-14A. (To view complete table, please refer to the ASCII files.)—Continued

Core, section	Sample	Top (cm)	Depth (mbsf)	Electrical resistivity (Ω×m)	Apparent formation factor
NGHP-01-14A—Continued					
21X-5	ER	96	156.96	0.788	3.94
21X-5	ER	117	157.17	0.855	4.28
21X-5	ER	135	157.35	0.707	3.54
21X-6	ER	8	157.58	0.702	3.51
21X-6	ER	27	157.77	0.806	4.03
21X-6	ER	45	157.95	0.923	4.62
21X-6	ER	65	158.15	0.726	3.63
21X-6	ER	86	158.36	0.957	4.79
21X-6	ER	106	158.56	0.882	4.41
22X-1	ER	37	159.97	0.722	3.61
22X-1	ER	55	160.15	0.757	3.79
22X-1	ER	75	160.35	0.885	4.43
22X-1	ER	95	160.55	0.847	4.24
22X-1	ER	115	160.75	0.755	3.78
22X-1	ER	135	160.95	0.866	4.33
22X-2	ER	15	161.25	0.746	3.73
22X-2	ER	38	161.48	0.761	3.81
22X-2	ER	54	161.64	0.819	4.10
22X-2	ER	72	161.82	0.738	3.69
22X-3	ER	15	162.75	0.599	3.00
22X-3	ER	35	162.95	0.697	3.49
22X-3	ER	55	163.15	0.671	3.36
22X-3	ER	75	163.35	0.713	3.57
22X-3	ER	92	163.52	0.714	3.57
23X-1	ER	33	169.53	0.622	3.11
23X-1	ER	45	169.65	0.685	3.43
23X-1	ER	73	169.93	0.845	4.23
23X-1	ER	95	170.15	0.747	3.74
23X-1	ER	122	170.42	0.685	3.43
23X-2	ER	15	170.85	0.775	3.88
23X-2	ER	35	171.05	0.692	3.46
23X-2	ER	55	171.25	0.897	4.49
23X-2	ER	72	171.42	0.749	3.75
23X-2	ER	95	171.65	0.728	3.64
23X-2	ER	116	171.86	0.67	3.35
23X-2	ER	135	172.05	0.724	3.62
23X-3	ER	15	172.35	0.623	3.12
23X-3	ER	35	172.55	0.64	3.20
23X-3	ER	56	172.76	0.773	3.87
23X-3	ER	74	172.94	0.742	3.71
23X-4	ER	15	173.85	0.598	2.99
23X-4	ER	42	174.12	0.556	2.78
23X-4	ER	65	174.35	0.665	3.33
23X-4	ER	85	174.55	0.736	3.68
23X-4	ER	107	174.77	0.699	3.50
23X-4	ER	125	174.95	0.62	3.10
23X-4	ER	143	175.13	0.634	3.17
23X-5	ER	17	175.37	0.605	3.03
23X-5	ER	35	175.55	0.822	4.11
23X-5	ER	55	175.75	0.73	3.65
23X-5	ER	75	175.95	0.709	3.55
23X-5	ER	95	176.15	0.753	3.77
23X-5	ER	115	176.35	0.628	3.14
23X-5	ER	135	176.55	0.637	3.19
23X-6	ER	15	176.85	0.669	3.35
23X-6	ER	37	177.07	0.676	3.38
23X-6	ER	52	177.22	0.824	4.12

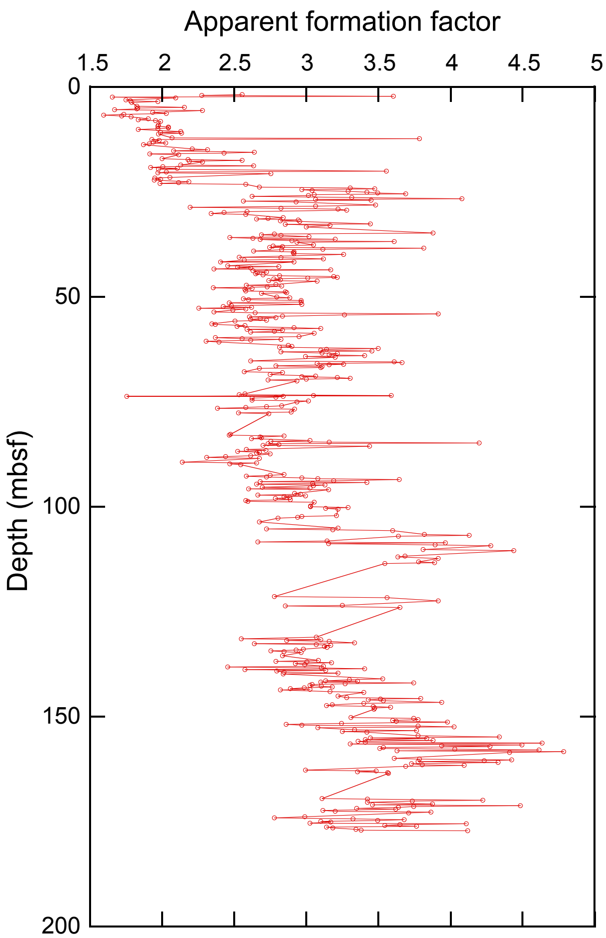

Figure 24. Apparent formation factor versus sub-bottom depth for Hole NGHP-01-14A.

Table 17. Contact *P*-wave velocity results determined on split cores sections from Hole NGHP-01-14A.

Core, section	Sample	Top (cm)	Depth (mbsf)	Vp (km/s)
		NGHP-01-14A		
1H-2	VP	50	2.00	1.472
1H-3	VP	35	3.35	1.475
2H-1	VP	50	5.00	1.478
2H-2	VP	45	6.45	1.477
2H-3	VP	25	7.75	1.478
2H-4	VP	25	9.25	1.477
2H-5	VP	25	10.75	1.489
2H-6	VP	25	12.25	1.486
2H-7	VP	25	13.25	1.496
3H-1	VP	125	15.25	1.491
3H-2	VP	45	15.95	1.491
3H-3	VP	25	17.25	1.496
3H-4	VP	25	18.75	1.501
3H-5	VP	25	20.25	1.502
3H-6	VP	25	21.75	1.509
3H-7	VP	40	22.90	1.512

Downhole Logging

Operations

The last core in Hole NGHP-01-14A was recovered from 180 mbsf (1086.6 mbrf) at 1830 hr on July 11, 2006. After a final temperature measurement with the DVTP at the bottom, the hole was conditioned for logging: a wiper trip was made by bringing the pipe to 60 mbsf and back to total depth; the hole was swept with 40 bbl of sepiolite mud; a "go devil" was pumped to open the lockable flapper valve at the bottom of the drill string; the hole was displaced with 60 bbl of 10.5 ppg barite; and the pipe was set to the logging depth at 58.4 mbsf (965 mbrf). Spooling of the wire line and preparation of the rig floor for logging started at 2230 hr and assembly of the first logging tool string started at 0005 hr on July 12.

The triple combo was complete at 0045 hr and run into hole (RIH) at 0110 hr. After exiting the pipe with some difficulty at 0212 hr, the bottom of tool string could not pass below 967 mbrf, only a few meters below the bit, with most of the string still inside the pipe. Circulating drilling mud at high flow and raising the pipe to give some more room to maneuver the tools could not help, and at 0250 hr it was decided to bring the tool back to the surface and to lower the pipe below this tight interval.

Table 18. Thermal conductivity results for Hole NGHP-01-14A.

Core, section	Sample	Top	Depth (mbsf)	Thermal conductivity (W/[m×K])
		NGHP-01-14A		
1H-3	TC	40	3.40	0.851
2H-3	TC	50	8.00	0.870
3H-3	TC	50	17.50	0.902
3H-7	TC	50	23.00	0.937
4H-1	TC	50	24.00	1.033
4H-3	TC	50	27.00	0.937
5H-1	TC	80	33.80	0.874
5H-3	TC	56	36.56	0.961
5H-6	TC	70	41.20	0.872
6H-1	TC	75	43.25	0.792
6H-7	TC	35	51.55	0.836
7H-1	TC	75	52.75	0.794
7H-7	TC	46	60.78	0.694
8H-1	TC	42	61.92	0.870
11X-3	TC	63	76.49	0.874
12X-3	TC	33	85.43	0.930
13X-3	TC	55	95.75	0.855
16X-3	TC	45	105.45	0.843
17X-2	TC	42	113.41	0.814
18X-3	TC	50	123.86	0.959
19X-3	TC	50	134.30	0.845
20X-3	TC	70	143.09	0.937
21X-1	TC	70	150.70	0.941
21X-3	TC	50	153.50	0.903
22X-3	TC	50	163.10	0.932
23X-3	TC	40	172.60	0.951
23X-6	TC	35	177.05	0.961

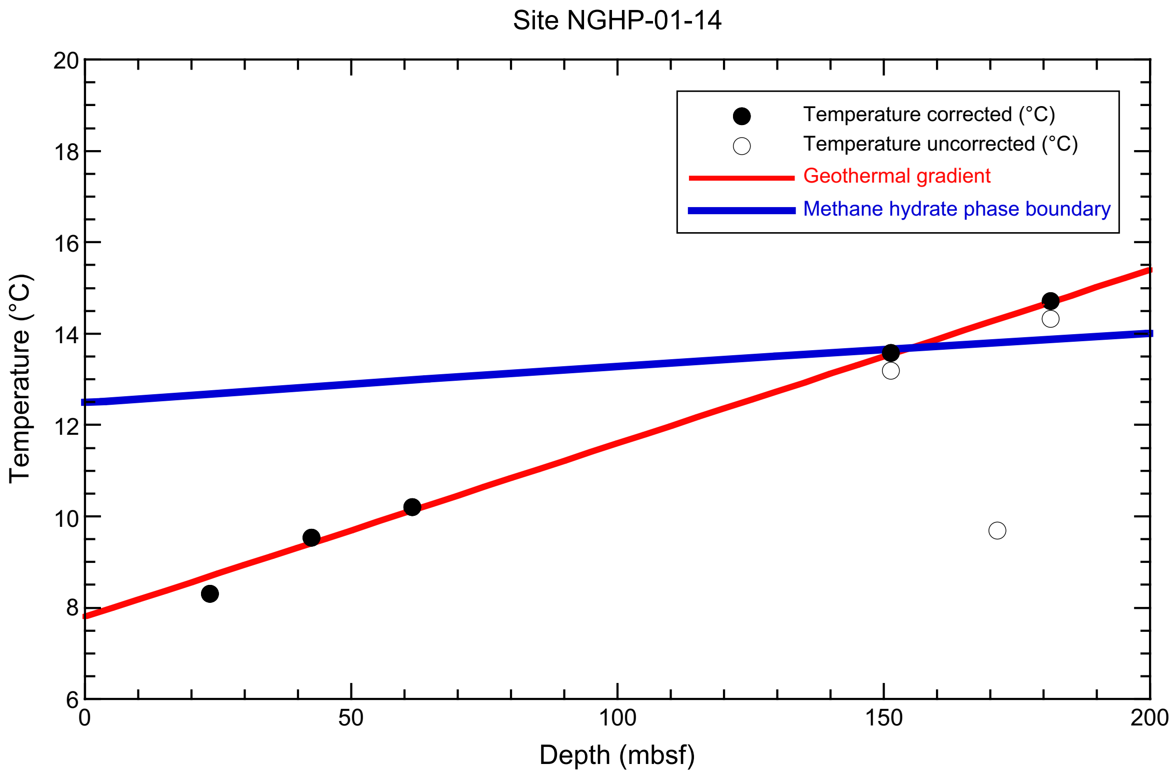

Figure 25. Geothermal gradient and estimated depth to the BSR from *in situ* temperature measurements for Hole NGHP-01-14A. [BSR, bottom-simulating reflector]

Table 19. *In situ* temperature estimates from Hole NGHP-01-14A.

Depth (mbsf)	Core	Assumed thermal conductivity (W/m•K)	Tool	Temperature (°C)	Ad-hoc calibration correction	Corrected temperature (°C)	Estimated uncertainty	Data quality
23.5	A03H	0.95	APCT-3	8.3	0	8.3	0.15	Fair
42.5	A05H	0.95	APCT-3	9.53	0	9.53	0.06	Good
61.5	A07H	0.95	APCT-3	10.2	0	10.2	0.06	Good
151.4	A20X	0.95	DVTP	13.19	0.50	13.69	0.05	Very good
171.4	A22X	0.95	DVTP	9.69	0.50	NA	NA	Poor
181.4	A23X	0.95	DVTP	14.32	0.50	14.82	0.1	Fair-good

Table 20. Summary of pressure coring operations at Site NGHP-01-14.

Core ID	Top of core (mbsf)	Length recovered (cm)*	Length curated (cm)*	Pressure at core depth (bar)	Pressure recovered (bar)		Comments
					logged**	gauge***	
				NGHP-01-14A			
09P	71.0	--	79	98	4	--	Ball valve did not seal
10Y	72.0	--	88	98	0	--	Did not retract
14P	101.0	--	91	101	0	--	No pressure
15E	102.0	32	34	101	82	85	Normal operation

Notes:

Water depth at Site NGHP-01-14 is 907 m. P=PCS, Y=FPC, E=HRC.

*Length measured from X-ray and gamma density analysis, which may not match curated core length.

**Last pressure recorded before data logger disconnected from corer autoclave. Temperature 2–4° C unless otherwise noted.

***Pressure measured when autoclave pressure transducer connected to external gauge. Pressure measured at 7° C unless otherwise noted.

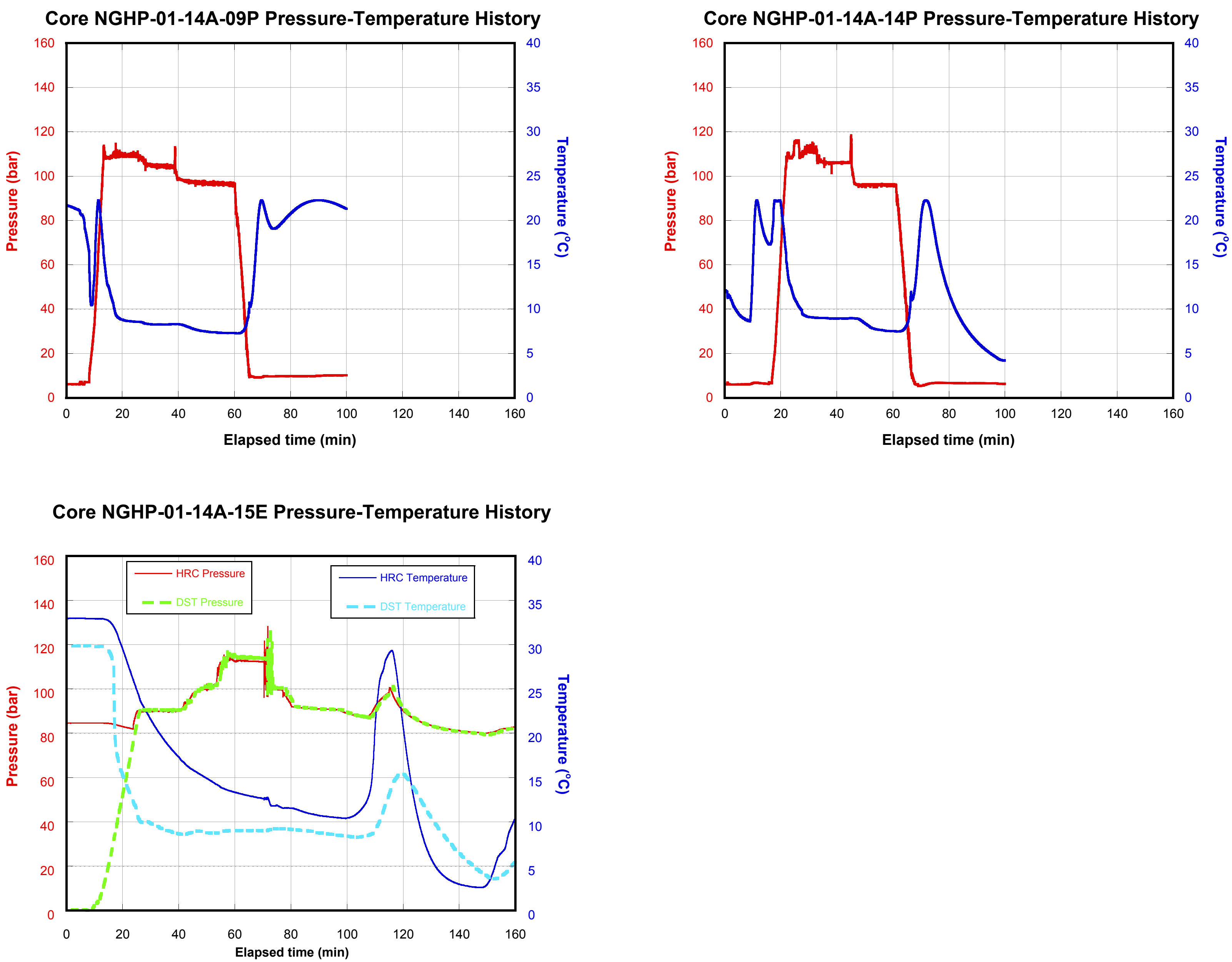

Figure 26. Temperature and pressure versus elapsed time for each pressure corer deployment as recorded by the corer's internal data logger and Micro data loggers, if used.

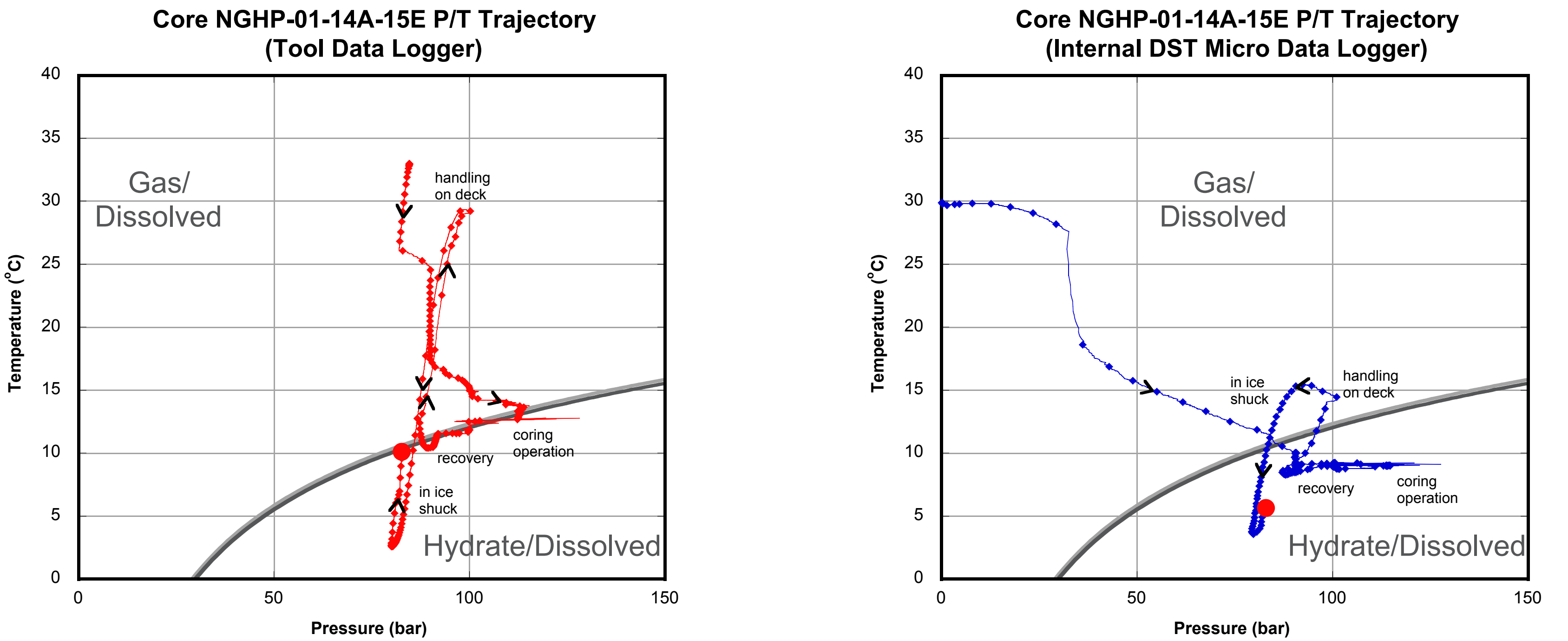

Figure 27. Temperature versus pressure for the deployment of Core NGHP-01-14A-15E, showing trajectories relative to gas hydrate stability at 30 ppt and 35 ppt salinity, calculated from Xu (2002, 2004). Small dots are approximately every minute. Large dot is final temperature and pressure of autoclave prior to data logger removal.

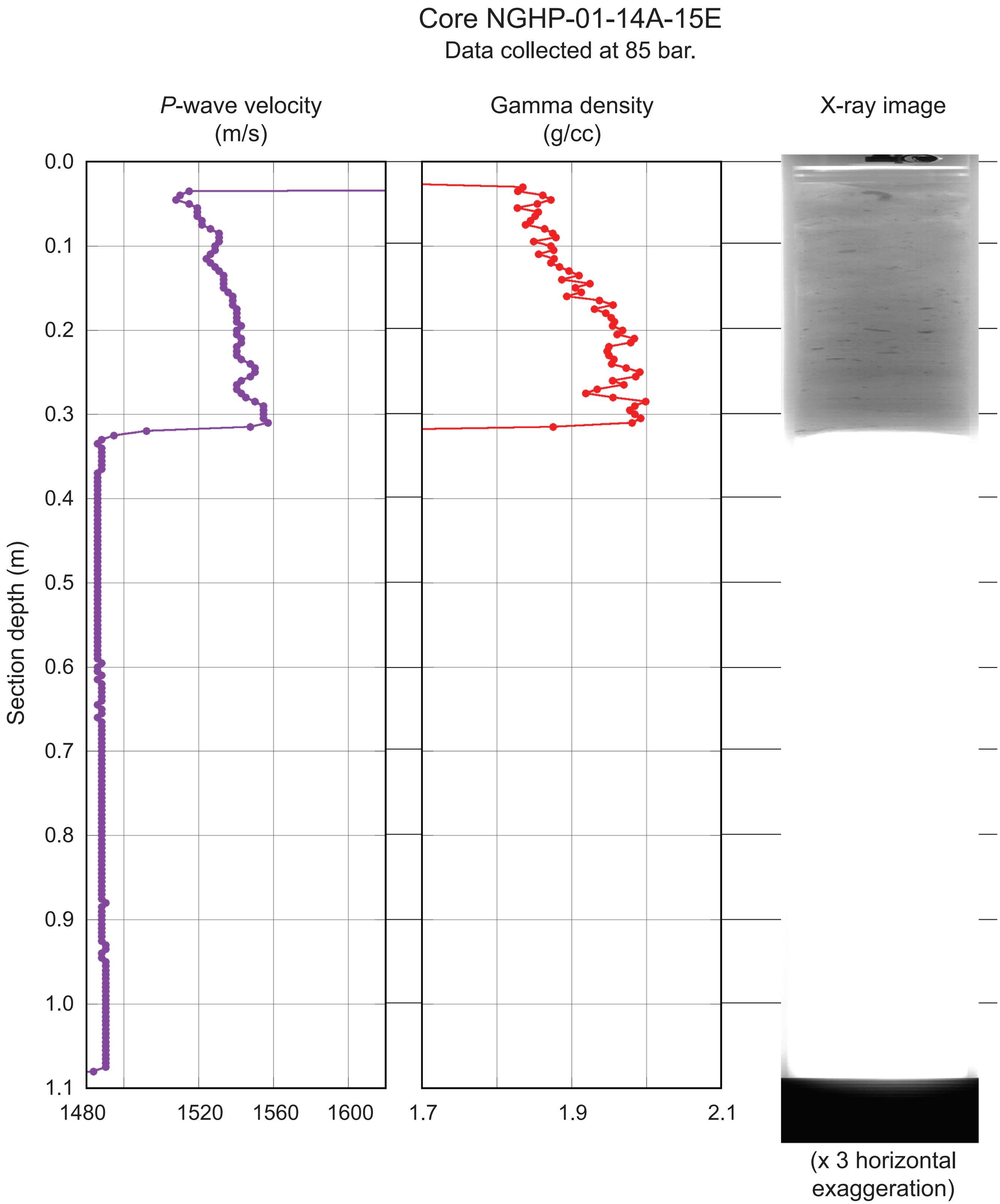

Figure 28. X-ray images and gamma density measurements collected at near *in situ* pressure and 7 °C for Core NGHP-01-14A-15E. X-ray images have been stretched 300 percent in the cross-core direction to show detail.

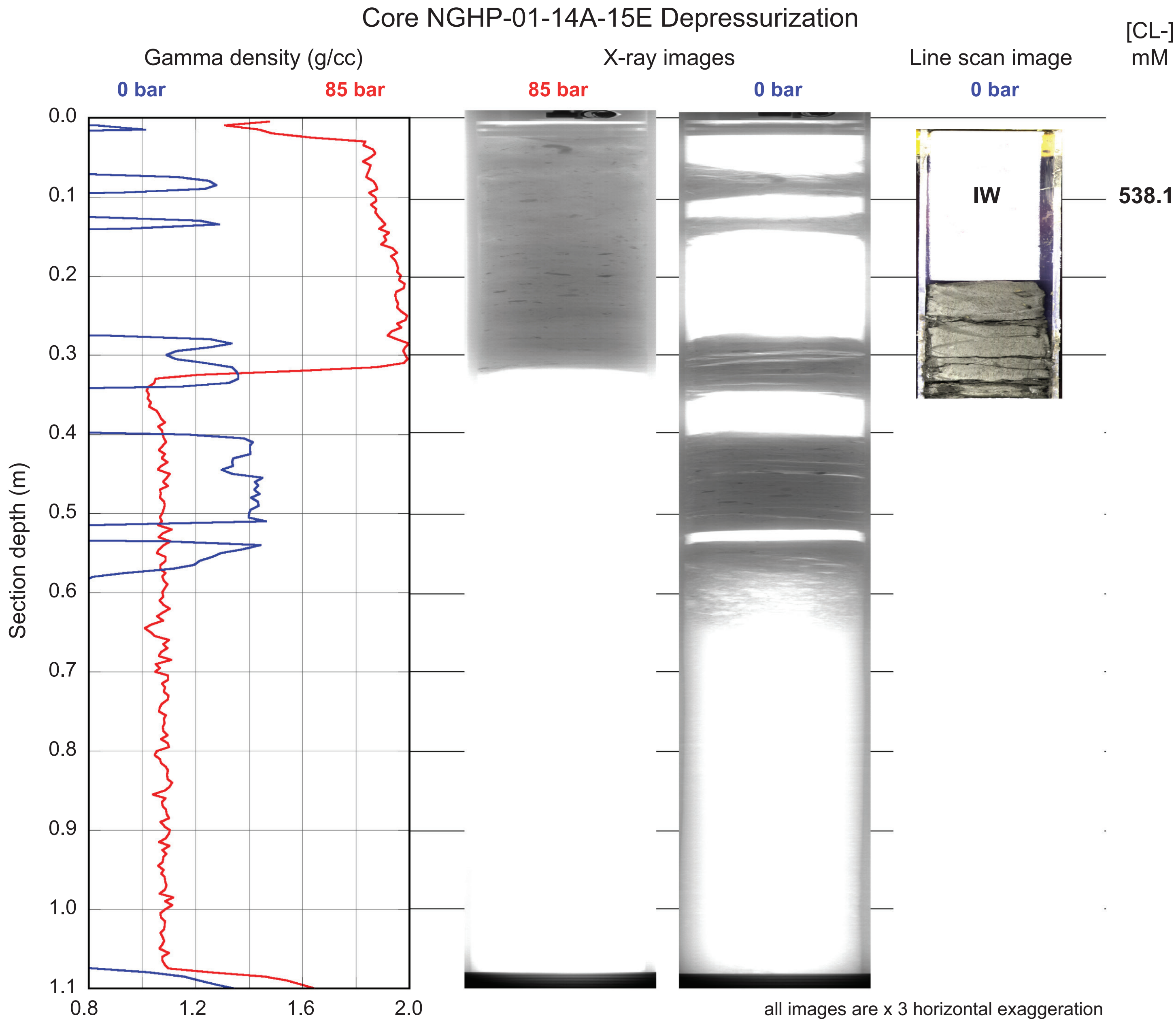

Figure 29. Summary of data taken from Core NGHP-01-14A-15E before and after depressurization, including gamma density profiles collected before and after depressurization, X-ray images collected before and after depressurization, and line-scan images collected after depressurization.

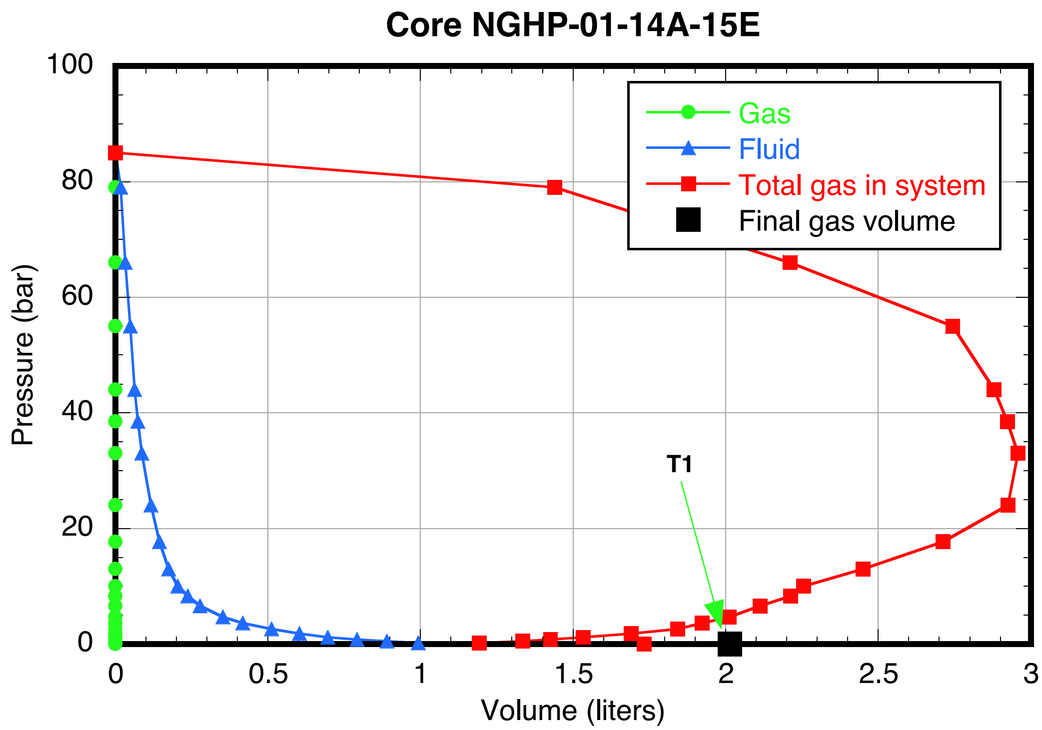

Figure 30. Pressure versus volume for Core NGHP-01-14A-15E, also showing placement of gas samples (see "Organic Geochemistry"). [Green circles, gas volume; blue triangles, fluid volume; red squares, total gas volume in system (calculated as described in the "Methods" chapter); large black square, final calculated gas volume from cores; and T (number), gas samples]

The triple combo was back to the surface at 0330 hr, partially laid down, and was RIH again at 0455 hr after one joint (9.5 m) had been added to the drill string and the bit positioned at 974 mbrf. Only minimal efforts were necessary to get the tools completely in open hole at 0550 hr. The log up stared at 0607 hr, at a logging speed of 900 ft/h, immediately after the tool had reached the total depth of 1,090 mbrf. One tight spot was encountered on the way down, at 1060 mbrf. At 0625 hr the HLDS caliper was closed and the wire-line heave compensator (WHC) turned off before entering the pipe. The tool was fully inside the pipe at 0635 hr and the logging pass was concluded at 0655 hr when the gamma ray log identified the seafloor at 909 mbrf. The tool was back to the surface at 0735 hr, and rigged down by 0810 hr.

Rig up of the FMS/Sonic tool string followed immediately. The string was complete at 0845 hr and RIH at 0855 hr. The bit was cleared without any problem at 1000 hr and the first pass started at 1020 hr from a total depth of 1,089 mbrf. The dipole sonic imager (DSI) acquisition modes were low frequency Monopole, low frequency upper dipole, standard frequency lower dipole and Stoneley. At 1036 hr the FMS calipers were closed and the WHC turned off before the cable head entered the pipe, and we kept logging up until the DSI was inside the pipe before going down for the second pass at 1048 hr. Logging up for the second pass started at 1100 hr from 1090 mbrf with the DSI configured to record low frequency monopole and cross-dipole modes. At 1118 hr the calipers were closed at 1015 mbrf, the WHC deactivated and we kept logging up until the tool was entirely inside the pipe at 1130 hr. The tool string was back at the surface at 1208 hr and disassembled by 1250 hr.

The VSI tool string for the final VSP run was complete at 1310 hr and RIH at 1320 hr. After reaching the bottom of the hole (1,087 mbrf) without any difficulty at 1358 hr, the VSI was anchored for the first station at 1086 mbrf and we started firing the seismic source at 1400 hr. The plan was to space the stations by 10 m in the deeper and shallower portions of the open hole, and to reduce the spacing to 5 m around the BSR at the estimated depth of 120 mbsf (~1,029 mbrf). Out of the 17 stations attempted with a total of 185 shots fired, only six provided waveforms of sufficient quality to be stacked to provide first arrival travel times. The last shot was fired at 1642 hr from 1000 mbrf. After disanchoring the VSI and turning down the WHC, the tool was inside the pipe without problem at 1650 hr and back to the surface at 1740 hr. It was disassembled at 1800 hr and the rig floor was ready to pull out of the hole at 1835 hr.

Logging Data Quality

The main logs recorded by the triple combo in Hole NGHP-01-14A are shown in figure 2. The hole size derived from the HLDS caliper shows that except for a ~10 cm restriction between 150 and 152 mbsf, and a 2-m washed out interval above it, the hole was in very good condition and in gage with the size of the drill bit, indicating that the data are of very good quality. This is confirmed by the almost perfect agreement between the density log and the density measured on core samples. This agreement extends even above ~92 mbsf, where the HLDS was closed before the top of the tool reached the drill pipe. It shows that the tool was still making good contact with the formation above this depth, which indicates that the hole was likely narrow in the upper part of the hole, and could explain our failure to lower the tool string in the first attempt. Two intervals display anomalously low density values that could be attributed to hole conditions: the washout immediately above the tight spot between ~148 and 150 mbsf, and an interval where the hole was apparently rugose between 90 and 95 mbsf.

The density porosity was calculated from the density log and from the grain density measured on core samples, by using at each depth the grain density from the closest sample.

Table 21. Methane-hydrate volume and concentration in pore space for the successful pressure core at Site NGHP-01-14. Values required for calculation of methane-hydrate concentration are also included.

Parameter	Units	NGHP-01-14A-15E
Core diameter	mm	51
Sediment length	cm	32
Sediment porosity	%	48
Pore volume	liters	0.31
Volume methane collected	liters	1.04
Methane concentration in pore fluids	mM	0*
Total methane in core	mmol	45.3
In situ salinity	ppt	33.5
Methane saturation**	mM	94.8
Methane in pore fluids, assuming saturation	mmol	29.6
Excess methane	mmol	15.8
Volume of methane hydrate	ml	2.1
Methane hydrate, % of pore volume***	%	0.7

Notes:

Rows in italics are calculated parameters.

*Methane concentration (via headspace) was not measured on these cores. Zero concentration generates a conservative (minimum) estimate of gas hydrate volume.

**Methane saturation calculated from Xu (2002, 2004) using a water depth of 907 mbsl, a thermal gradient of 37 °C/km, a seafloor temperature of 7.92 °C, and the above salinities.

***Assuming all gas hydrate evenly distributed throughout the pore space.

Hence the good agreement between the density-porosity log and the porosity measurements from core samples is a direct consequence of the good agreement in the density data. The neutron porosity is consistently higher than the other porosity estimates because of the influence of mineral-bound water in these clay-dominated sediments.

The hole size calculated from the FMS caliper logs in figure 33 shows that the hole remained in good condition during the FMS/Sonic run, which is confirmed in the same figure by the strong amplitude and coherence of the sonic waveforms over most of the interval logged, despite very low V_P values. However, the dipole waveforms show that above ~105 the shear velocity was too low for the flexural waves to be properly captured by the recording time window and further processing was required to derive reliable V_S logs above this depth. In addition, the monopole waveform amplitude and coherence are reduced in two intervals, between 110 and 125 mbsf and between ~140 and 150 mbsf. The resulting V_P values are anomalously variable in these intervals and required to be reprocessed.

Because of the low strength of these unconsolidated sediments, only 6 stations out of 17 attempts allowed to identify the first arrival travel times with enough accuracy to draw a preliminary time to depth relationship. Figure 34 shows that at least two of these arrivals will need to be reprocessed, but the least square linear fit between the four most reliable arrivals gives an average velocity of 1,565 m/s, which is in good agreement with the V_P log values. It also suggests that the depth of the BSR, which in this site was at 1,340 ms twtt, is approximately 116 mbsf, in good agreement with the predicted depth.

Logging Units

The trends in the main logs displayed in figures 32 and 33 (particularly the density, resistivity, and velocity logs) allow the definition of three logging units with distinct characteristics:

Over most of Logging unit 1 (65–105 mbsf), the velocity, density and resistivity logs follow mostly uniform baseline trends with a few excursions that could be associated with the occurrence of small amount of gas hydrate. Two intervals in particular (67–72 mbsf and 82–87 mbsf) show higher resistivity value without any associated change in density or porosity and might contain some gas hydrate in their pore space. The HLDS caliper was closed above 92 mbsf, and even if the density log seems to be in good agreement with the core data over this depth, its almost constant value needs to be considered with caution. As the gamma ray log is corrected for the hole size measured by the HLDS caliper, and for the bit size once the caliper is closed, the higher gamma ray readings above 92 mbsf are possibly an artifact that needs also to be interpreted carefully.

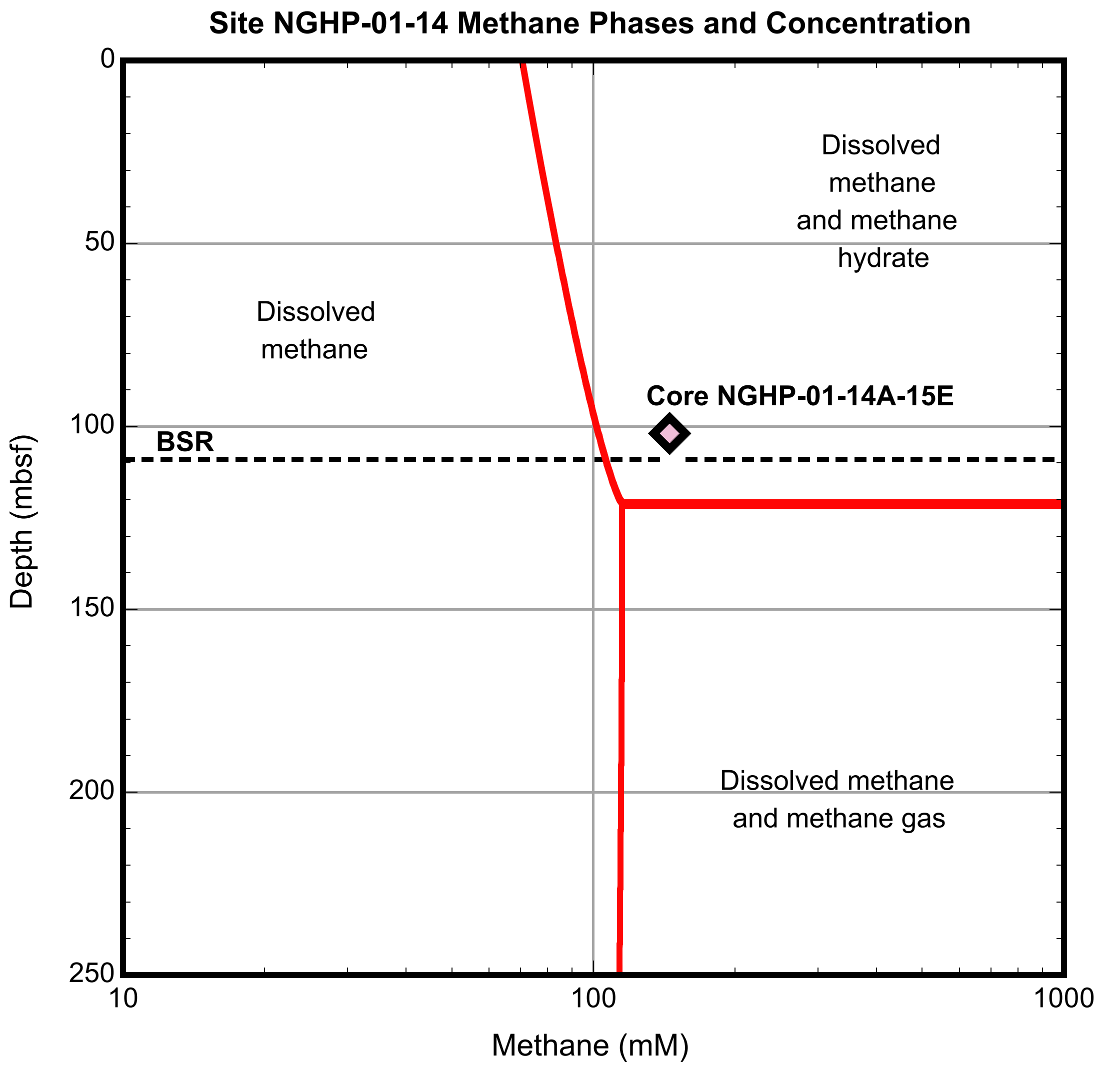

Figure 31. Methane-phase diagram for Site NGHP-01-14, with total methane concentration measured from the one successful pressure core at Site NGHP-1-14. The shipboard-calculated seafloor temperature (7.92 °C) and thermal gradient (37 °C/km) were taken from "Downhole Temperature Measurements" in "Physical Properties"; the salinity was the background salinity around the depths of the pressure cores (35 ppt; from table 4); methane saturation was calculated according to Xu (2002, 2004).

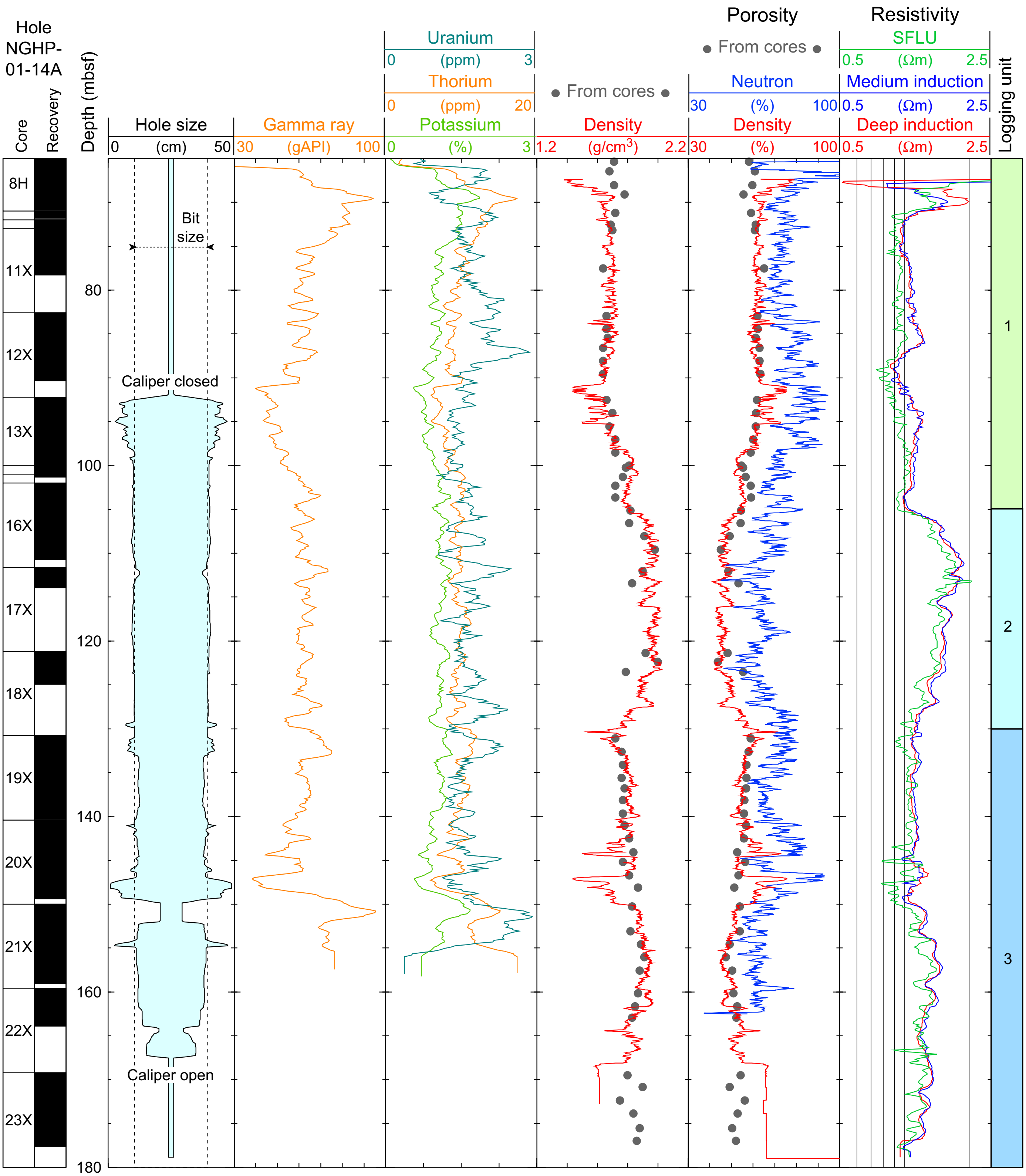

Figure 32. Summary of the wireline logs recorded in Hole NGHP-01-14A. The hole size is calculated from the Hostile Litho Density Sonde (HLDS) caliper. The density and porosity measurements made on core samples are shown for comparison. [SFLU, Spherically focused unaveraged resistivity]

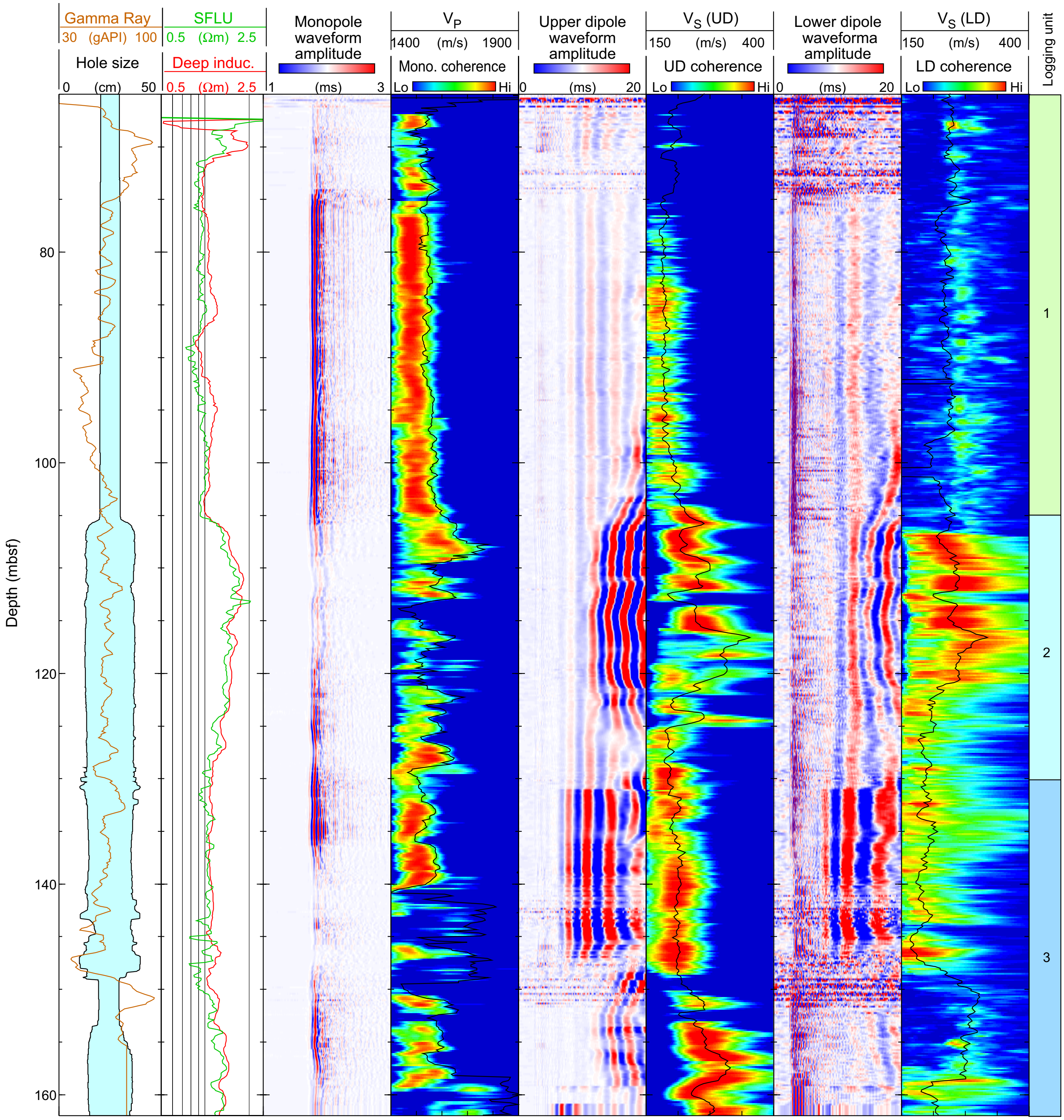

Figure 33. Sonic waveform amplitude and coherence data and velocity logs measured by the DSI in Hole NGHP-01-14A. The hole size, calculated from the FMS calipers, and the gamma ray and resistivity logs are shown for quality control and correlation. [DSI, Dipole Shear Sonic Imager; V_P, *P*-wave velocity; V_S, S-wave velocity, LD, Lower dipole; UD, Upper dipole]

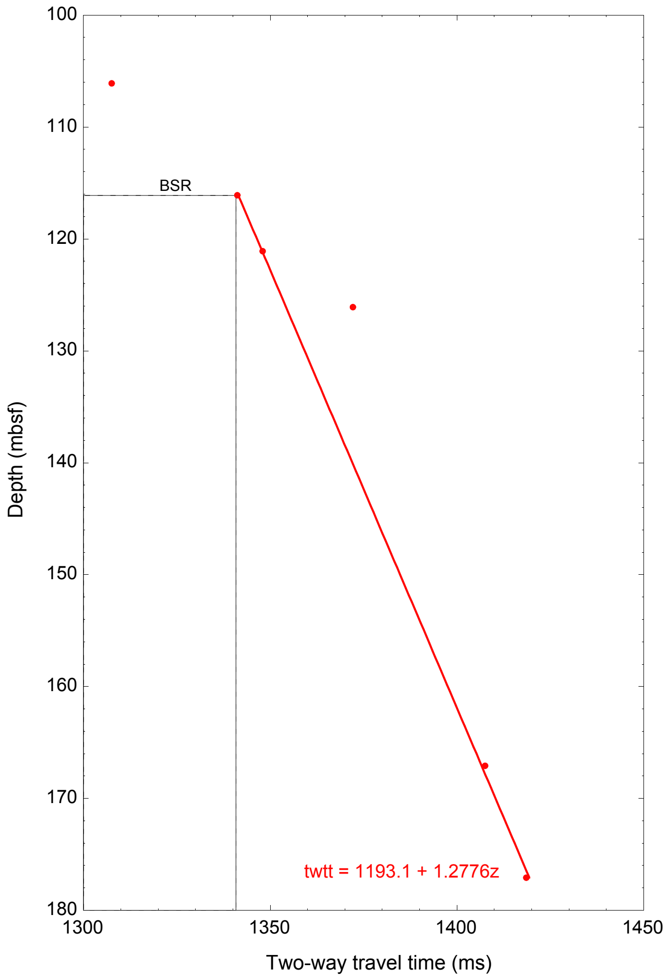

Figure 34. Time-depth plot of the preliminary first break times in the Hole NGHP-01-14A vertical seismic profile. The least square linear fit is calculated only for the four most reliable travel times.

Logging unit 2 (105–130 mbsf) corresponds to a bulge in resistivity, shear velocity and density that is likely created by a lithological change and has little or nothing to do with the occurrence of gas hydrate. The V_P log shows a sharp increase at the top of this subunit, but the monopole waveform display only very variable coherence and low amplitude over the rest of the unit. The coincidence with higher V_S values in the unit suggests that the V_S data respond to the harder formation identified by the higher density and resistivity values, while the monopole amplitudes could be affected the presence of small amounts of free gas.

Logging unit 3 (130–180 mbsf) is characterized by a slight but steady increase with depth in density and resistivity, while the low coherence in most sonic waveforms indicate the likely presence of some amounts of free gas in this unit, between ~135 and 150 mbsf.

Gas-Hydrate and Free Gas Occurrence

As previously discussed (see “Downhole Logging” in the “Methods” chapter), the presence of gas hydrate is generally identified by increases in electrical resistivity and acoustic velocity that are not accompanied by a corresponding density increase. Most of the variations in resistivity observed in Hole NGHP-01-14A show predominantly a positive correlation with the density log, suggesting that gas hydrate could be present in only a few intervals.

To make a quantitative estimate of the amount of gas hydrate present, we followed the procedure described in “Downhole Logging” in the “Methods” chapter, to apply the Archie relationship to the resistivity and porosity logs recorded in Hole NGHP-01-14A. Because no LWD logs were recorded in this site, we used the wire-line resistivity logs to make this estimate. The procedure and the results are illustrated in figure 34. The pore fluid resistivity (R_w) was estimated from Fofonoff (1985) using a temperature profile derived from a linear fit of the *in situ* temperature measurements at Site NGHP-01-14 (7.92 °C at the seafloor; gradient of 37 °C/km, (see “Physical Properties”) and a constant water salinity of 33 ppt, which is an average of the values measured in Site NGHP-01-14. The estimated *m* curve was derived from R_w, the porosity (ϕ) and resistivity (R_t) logs ($m_{est} = -\log F/\log\phi$, where $F = R_t / R_w$). As this relationship is defined for water-saturated sediments, the chosen value of $m = 2.0$ is given by the baseline of this curve in the low-resistivity intervals where there is likely no gas hydrate. Using the porosity log and Archie’s equation ($R_0 = (a\ R_w) / f^m$), we derive the predicted resistivity of the water-saturated formation R_O. A qualitative influence of gas hydrate on the resistivity log is indicated by the difference between R_0 and the measured resistivity R_t. The estimated water saturation, assumed to be the numerical complement of the hydrate saturation, is $S_w = (R_0/R_t)^{1/n}$, where n=2 (Pearson and others, 1983). We used the density porosity and two resistivity measurements to derive the results shown in figure 35. The Spherically Focused unaveraged resistivity (SFLU) has the highest resolution, but the shallowest penetration, of the resistivity measurements made by the DIT tool and is more sensitive to drilling disturbances; the Deep Induction log (ILD) has the deepest penetration, but a lower vertical resolution. The combination of these two estimates provides a possible range of gas-hydrate distribution around Hole NGHP-01-14A.

The results indicate gas-hydrate saturation could be as high as ~20 percent in some intervals. As noted earlier, the higher resistivity between ~105 and 130 mbsf are not associated with any significant amount of gas hydrate as they coincide with an increase in density. Any estimated accumulation below the bottom of the gas-hydrate stability zone, which if it coincides with the BSR is at ~116 mbsf, should be free gas. Several intervals, shaded in grey in figure 35, had anomalously low density log values resulting in excessively high porosity and estimated gas-hydrate or free gas concentrations. The high resistivity values immediately below the pipe between ~65 and 72 mbsf could correspond to actual significant gas-hydrate accumulation, but the unreliability of the density log in this interval makes the saturation estimate questionable.

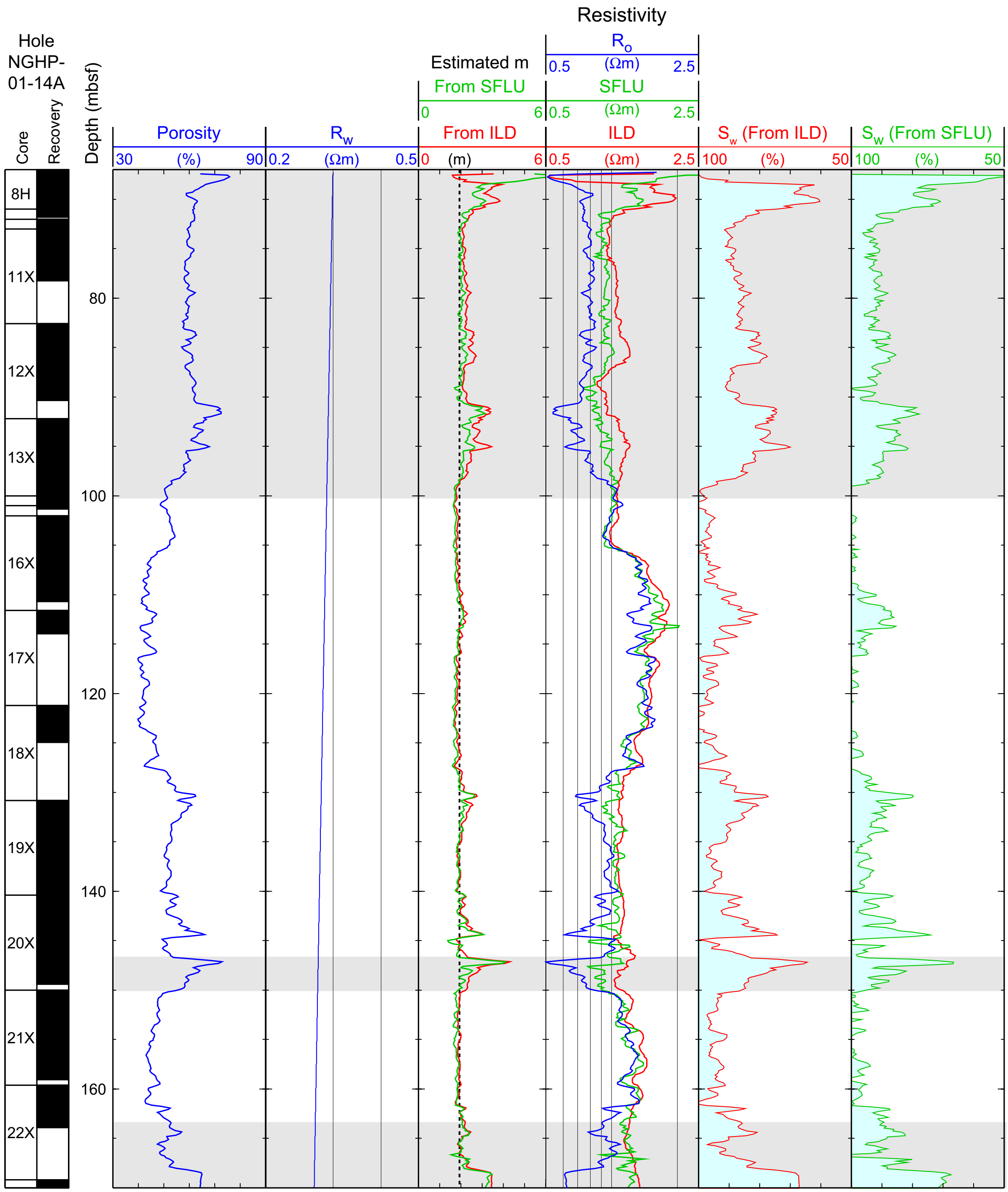

Figure 35. Water saturations from Archie's equation and wireline porosity and resistivity logs in Hole NGHP-01-14A. The gray area indicates degraded data quality. [R_w, formation water resistivity; R_0, computed formation resistivity for 100 percent water saturation; R_t, measured resistivity; S_w, water saturation; SFLU, spherically focused unaveraged resistivity; ILD, deep induction resistivity log] The areas in grey indicate intervals with unreliable density and porosity measurements where saturation values are likely overestimated]

References Cited

Bjerrum, L., 1972, Embankments on soft ground: Proceedings of the ASCE Specialty Conference on Performance of Earth and Earth-Supported Structures, Purdue University, v. II, p. 1–54.

Davis, E.E., Hyndman, R.D., and Villinger, H., 1990, Rates of fluid expulsion across the northern Cascadia accretionary prism—Constraints from new heat flow and multichannel seismic reflection data: Journal of Geophysical Research, v. 95, p. 8869–8889.

Duan, Z., Møller, N., Greenberg, J., and Weare, J.H., 1992, The prediction of methane solubility in natural waters to high ionic strengths from 0° to 250 °C and from 0 to 1600 bar: Geochimica et Cosmochimica Acta, v. 56, p. 1451–1460.

Fofonoff, N.P., 1985, Physical properties of seawater: Journal of Geophysical Research, v. 90, no. C2, p. 3332–3342.

Holtz, R.D., and Kovacs, W.D., 1981, An introduction to geotechnical engineering: Englewood Cliffs, N.J., Prentice-Hall, Inc., 733 p.

Hunt, R.E., 1984, Geotechnical engineering investigation manual: New York, McGraw-Hill Book Company, 983 p.

Kvenvolden, K.A., and Lorenson, T.D., 2000, Methane and other hydrocarbon gases in sediment from the southeastern North American continental margin, *in* Paull, C.K., Matsumoto, R., Wallace, P.J., Black, N.R., Borowski,W.S.,Collett, T.S., Damuth, J.E., Dickens, G.R., Egeberg, P.K., Goodman,K., Hesse, R.F., Hiroki, Y., Holbrook, W.S., Hoskins, H., Ladd, J. ,Lodolo, E., Lorenson, T.D.,Musgrave, R.J., Naehr, T.H., Okada, H., Pierre, C., Ruppel, C.D., Satoh, M., Thiery, R., Watanabe, Y., Wehner, H., Winters, W.J.,and Wood, W.T., Gas hydrate sampling on the Blake ridge and Carolina rise; covering leg 164 of the cruises of the drilling vessel *JOIDES Resolution*, Halifax, Nova Scotia, to Miami, Florida, sites 991–997, 31 October–19 December 1995: Proceedings of the Ocean Drilling Program, Scientific Results, v. 164, p. 29–36.

Ladd, C.C., Foote, R., Ishihara, K., Schlosser, F., and Poulos, H.G., 1977, Stress-deformation and strength characteristics—State-of-the-art report: Proceedings of the Ninth International Conference on Soil Mechanics and Foundation Engineering, Tokyo, v. 2, p. 421–494.

Lambe, T. W. and Whitman, R.V., 1969, Soil mechanics: New York, John Wiley and Sons, 553 p.

Musgrave, R.J., Bangs, N.L., Larrasoana, J.C., Gracia, E., Hollamby, J., and Vega, M.E., 2006, Rise of the base of the gas hydrate zone since the last glacial recorded by rock magnetism: Geology, v. 34, no. 2, p. 117–120.

Novosel, I., Winters, W.J., Boldina, O.M., Labails, C., and Geli, L., 2007, Thermal conductivity of sediment recovered from the IMAGES VIII/PAGE 127 Gas Hydrate and Paleoclimate Cruise on the *R/V Marion Dufresne* in the Gulf of Mexico, 2–18 July 2002, *in* Winters, W.J., Lorenson, T.D., and Paull, C.K., eds., Initial report of the IMAGES VIII/PAGE 127 gas hydrate and paleoclimate cruise on the RV Marion Dufresne in the Gulf of Mexico, 2–18 July 2002: U.S. Geological Survey Open-File Report 2004–1358.

Pearson, C.F., Halleck, P.M., McGuire, P.L., Hermes, R., and Mathews, M., 1983, Natural gas hydrate deposits—A review of *in situ* properties: Journal of Physical Chemistry, v. 87 p. 4180–4185.

Sloan, E.D., 1998, Clathrate Hydrates of Natural Gases (2d ed.): New York (Marcel Dekker), 705 p.

Tréhu, A.M., Bohrmann, G., Rack, F.R., Torres, M.E., Delwiche, M.E., Dickens, G.R., Goldberg, D.S., Gracia, E., Guerin, G., Holland, M., Johnson, J.E., Lee, Y.J., Liu, C.S., Long, P.S., Milkov, A.V., Riedel, M., Schultheiss, P., Su, X., Teichert, B., Tomaru, H., Vanneste, M., Watanabe, M., and Weinberger, J.L.,, 2003, Proceedings of the Ocean Drilling Program, Initial Reports 204 [CD-ROM], 81 p.

Xu, W., 2002, Phase balance and dynamic equilibrium during formation and dissociation of methane gas hydrate: Proceedings of the 4th International Conference on Gas Hydrates, Yokohama, Japan, p. 195–200.

Xu, W., 2004, Modeling dynamic marine gas hydrate systems: American Mineralogist, v. 89 p. 1271–1279.